



University of Bremen

Faculty of Geosciences

# The transition from stable to slow to fast earthquake slip on faults: the influence of surface morphology, fault normal stiffness and lithology

Dissertation in Geosciences

By

Agathe M. Eijsink

Submitted in Partial Fulfillment of the Requirements for the Degree of

–Doctor rer. nat. –

Thesis submission date: September 2021

Date of Colloquium: 5 November 2021



## Reviewers / Gutachter

**Dr. Matt J. Ikari**

(Supervisor)

MARUM – Centre for Marine Environmental Sciences

University of Bremen

Leobener Straße 8

28359 Bremen, Germany

**Dr. Marco M. Scuderi**

Department of Earth Sciences

La Sapienza University of Rome

Building CU005

Piazzale Aldo Moro 5

00185 Roma, Italy

## Abstract

Over the last decades, new types of earthquakes have been discovered. The most well-known group of ordinary earthquakes might be the most dangerous as they emit the largest amount of seismic radiation and cause ground-shaking, but repeating slow earthquakes can also damage buildings and infrastructure. Ordinary earthquakes occur when movement on a fault is unstable and a run-away process accelerates the movement to seismogenic velocities. During slow earthquakes, there are also clearly defined phases of faster slip along the fault, but the maximum slip velocity reached during these phases is lower. Then, there are aseismic faults, where slip accumulates constantly by stable creep at a rate close to the far-field stressing rate. The mechanisms that control the nature of sliding behavior of faults are multiple and studied in more or less detail. In this thesis, I explore how three factors influence fault stability: fault surface roughness and roughness anisotropy, fault-normal stiffness and stiffness contrasts across a fault, and the lithological controls on the extraordinary shallow slow slip events in the Hikurangi subduction zone margin (New-Zealand).

Here, I present results using direct shear experiments, while varying one of the studied variables. To study the influence of fault surface morphology, I use two materials; a velocity-weakening and therefore potentially unstable pure quartz powder, and Rochester shale powder, which is velocity-strengthening and therefore likely to show stable sliding. Fault surface morphology evolves with displacement and its influence on frictional behavior is therefore studied by varying the amount of displacement on the samples. To test the influence of host-rock stiffness, the testing device is fitted with springs of variable stiffness in both the shear-parallel and fault-normal directions. Testing occurs on the intrinsically unstable quartz powder and I analyze both the frictional properties as well as the slip instabilities that occur. For the study about the Hikurangi margin, I use samples of the sediments on the incoming plate and use realistically low deformation rates, to study the frictional behavior and the occurrence of spontaneous slow slip events during the experiments.

The results show rough, isotropic faults can host slip instabilities, because these show the required velocity-weakening frictional behavior. Striated, smooth surfaces are velocity-strengthening and promote stable sliding. The formed fault surfaces obey the typical self-affine fractal scaling, that make these results directly applicable to natural faults. Reducing the fault-normal stiffness causes the fault to become less velocity-weakening and would therefore promote stable sliding. However, slip instabilities occur when the fault-normal stiffness is reduced, which I explain by a different mechanism that requires a stiffness asymmetry. The asymmetry is the result of reducing the fault-normal stiffness on one side of the fault. The plate-rate shear

experiments on Hikurangi sediments show spontaneous slow slip events occur in the calcite-rich lithologies, whereas the weakest lithologies are velocity-strengthening.

Altogether, the results presented in this thesis suggest unstable sliding will occur on rough, isotropic fault patches. The slow slip events in the Hikurangi margin can only occur when the slow slip event-hosting lithologies are introduced into the deformation zone. This could be explained by a geometrically complex deformation zone due to subducting seamounts. Stiffness contrasts, due to lithological contrast across a fault or due to asymmetric damage, may cause slip instabilities that are not explained by the traditional critical stiffness theory. I show the three studied variables are closely linked and fault surface roughness, fault stiffness and stiffness contrast, as well as fault zone lithology may affect each other.

## Zusammenfassung / German summary

In den letzten Jahrzehnten wurden neue Arten von Erdbeben entdeckt. Die bekanntesten regulären Erdbeben sind vielleicht die gefährlichsten, da sie eine große Menge der seismischen Wellen emittieren und Bodenerschütterungen verursachen. Langsame Erdbeben können aber auch, wenn sie sich wiederholen, Gebäude und Infrastrukturen zerstören. Reguläre Erdbeben werden ausgelöst, wenn die Bewegung auf einer Verwerfung instabil ist und ein sich verstärkender Prozess die Bewegung bis zu seismogenen Geschwindigkeiten beschleunigt. Bei langsame Erdbeben gibt es auch klar definierte Rutschungsphasen, aber die erreichte Maximalgeschwindigkeit ist geringer als bei den regulären Erdbeben. Dann gibt es aseismische Verschiebungen, bei denen die Bewegung stabil ist und eine konstante Geschwindigkeit hat, die der Fernfeld-Belastungsrate gleicht. Die Mechanismen, die die Art des Gleitverhaltens auf Verwerfungen bestimmen, sind vielfältig und mehr oder weniger detailliert untersucht. In dieser Dissertation untersuche ich wie drei Faktoren die Stabilität von Verschiebungen beeinflussen: die Rauheit der Gleitfläche und Rauheitsanisotropie, die Steifigkeit normal zur Bruchfläche und Steifigkeitskontraste über die Verwerfung hinweg, sowie die Einflüsse der Lithologie auf langsame Erdbeben in der Hikurangi Subduktionszone (Neu-Seeland).

Ich benutze Rahmenscherversuche, bei denen die untersuchten Variablen einzeln variiert werden. Um den Einfluss von Oberflächenrauheit zu untersuchen, benutzte ich zwei Materialien mit unterschiedlich geschwindigkeitsabhängigen Reibungskoeffizienten. Quarzpulver, welches geschwindigkeitsschwächend und damit potenziell instabil ist, und Pulver aus Rochester Shale (schiefer), was geschwindigkeitsstärkend ist und wofür stabiles Verhalten zu erwarten ist. Die Morphologie der Verwerfungsfläche entwickelt sich mit dem Scherweg, weswegen ihr Einfluss auf das Reibungsverhalten durch das Variieren vom kumulativen Scherweg untersucht wird. Um den Einfluss der Muttergesteinssteifigkeit zu testen, wurde das Rahmenschergerät mit Federn variabler Steifigkeit sowohl in scherparalleler als auch in normaler Richtung ausgestattet. Getestet wurde am intrinsisch instabilen Quarzpulver und gemessen wurden sowohl die Reibungseigenschaften, als auch die auftretenden Instabilitäten. Für die Studie über die Hikurangi-Subduktionszone verwende ich Sedimentproben aus dem undeformierten Teil der subduzierenden Erdplatte und benutzte realistisch niedrige Deformationsraten, um das Reibungsverhalten und das Auftreten von spontanen langsamen Erdbeben zu untersuchen.

Die Ergebnisse zeigen, dass raue, isotrope Gleitflächen Instabilitäten beherbergen können, da diese das erforderliche geschwindigkeitsschwächende Reibungsverhalten aufweisen. Geriffelte, glattere Gleitflächen zeigen geschwindigkeitsverstärkendes Reibungsverhalten, das auf stabiles Verhalten hinweist. Die gebildeten Gleitflächen verhalten sich nach der typischen selbstaffinen

fraktalen Skalierung, die diese Ergebnisse direkt auf natürliche Verwerfungen anwendbar macht. Eine verminderte flächennormale Steifigkeit bewirkt eine Abnahme der Geschwindigkeitsabhängigkeit der Reibung. Instabilitäten treten jedoch auf, was ich durch einen anderen Mechanismus erkläre, der eine Steifigkeitsasymmetrie erfordert. Diese tritt auf, wenn die flächennormale Steifigkeit auf einer Seite der Fläche reduziert wird. Scherversuche mit Plattengeschwindigkeit ähnlichen Scherraten an Hikurangi-Sedimenten zeigen, dass in den kalzitreichen Lithologien spontane langsame Erdbeben auftreten, während die Lithologien mit den geringsten Reibungskoeffizienten geschwindigkeitsverstärkend sind.

Insgesamt deuten die in dieser Dissertation präsentierten Ergebnisse darauf hin, dass auf rauen, isotropen Bruchflächen instabiles Gleiten auftritt. Die langsamen Erdbeben in der Hikurangi-Subduktionszone können nur auftreten, wenn die langsamen Erdbeben beherbergenden Lithologien in die Deformationszone eingebracht werden. Dies könnte durch den geometrischen Einfluss von subduzierten Seebergen auf die Deformationszone erklärt werden. Kontraste in der Steifigkeit aufgrund von lithologischen Kontrasten über eine Verwerfung oder asymmetrischer Beschädigung können Instabilitäten verursachen. Diese können nicht durch die traditionelle Theorie der kritischen Steifigkeit erklärt werden. Ich zeige, dass die drei untersuchten Variablen eng miteinander verbunden sind und sich die Oberflächenrauheit, die flächennormale Steifigkeit und der Steifigkeitskontrast, sowie die Lithologie der Deformationszone gegenseitig beeinflussen können.

## Contents

Reviewers / Gutachter.....	- 3 -
Abstract.....	- 4 -
Zusammenfassung / German summary.....	- 6 -
Contents.....	- 8 -
1. Introduction.....	- 12 -
1.1. Aims and objectives .....	- 12 -
1.2 Earthquakes and friction.....	- 14 -
1.2.1 What is an earthquake .....	- 14 -
1.2.2 Fault surfaces.....	- 15 -
1.2.3 Rate-and-state dependent friction.....	- 17 -
1.2.4 Spring-slider models .....	- 20 -
1.2.5 Slipping fault patches .....	- 22 -
1.2.6 Friction on natural faults .....	- 23 -
1.3 The studied variables.....	- 25 -
1.3.1 Fault surface roughness.....	- 25 -
1.3.2 Fault normal stiffness .....	- 25 -
1.3.3 Lithology.....	- 26 -
1.4 Research questions .....	- 27 -
1.5 Outline and author contributions.....	- 27 -
2 Fault surface morphology as an indicator for slip stability .....	- 31 -
2.1 Abstract .....	- 31 -
2.2 Introduction .....	- 31 -
2.3 Short method .....	- 33 -
2.4 Results: striations and frictional behavior .....	- 36 -
2.5 Discussion .....	- 38 -
2.5.1 Validity for other materials .....	- 38 -
2.5.2 Mechanism: elongating asperities .....	- 38 -

2.5.3	Upscaling to natural faults.....	- 41 -
2.6	Supplementary figures.....	- 44 -
2.7	Detailed methods.....	- 46 -
2.7.1	Friction experiments.....	- 46 -
2.7.2	Surface topography microscopy.....	- 49 -
3	How fault-normal and shear-parallel stiffness influence frictional sliding behavior-	53
-		
3.1	Abstract.....	- 53 -
3.2	Introduction.....	- 54 -
3.3	Methods.....	- 56 -
3.3.1	Experimental procedure.....	- 56 -
3.3.2	Data analysis.....	- 57 -
3.3.3	Stiffness adjustments.....	- 59 -
3.3.4	Slip events.....	- 60 -
3.4	Results.....	- 61 -
3.4.1	Frictional behavior.....	- 61 -
3.4.2	Slip event occurrence.....	- 64 -
3.4.3	Slip event statistics.....	- 66 -
3.5	Discussion.....	- 68 -
3.5.1	Effects on friction.....	- 68 -
3.5.2	Occurrence of stick-slip.....	- 69 -
3.5.3	Application for natural faults.....	- 74 -
3.6	Conclusion.....	- 77 -
4	Plate-rate frictional behavior of sediment inputs to the Hikurangi subduction margin: How does lithology control slow slip events?.....	- 79 -
4.1	Abstract.....	- 79 -
4.2	Plain language summary.....	- 80 -
4.3	Introduction.....	- 80 -

4.4	Geological Setting .....	- 83 -
4.5	Materials and Methods .....	- 85 -
4.5.1	Materials.....	- 85 -
4.5.2	Friction experiments.....	- 85 -
4.5.1	Friction data analysis.....	- 88 -
4.5.1	Slow Slip Event analysis .....	- 91 -
4.6	Results .....	- 93 -
4.6.1	Frictional behavior .....	- 93 -
4.6.2	Slow slip events.....	- 94 -
4.7	Discussion .....	- 97 -
4.7.1	Calcite content.....	- 97 -
4.7.1	SSE occurrence.....	- 98 -
4.7.2	Earthquake relationships .....	- 101 -
4.7.3	Hikurangi Margin.....	- 103 -
4.8	Conclusion.....	- 106 -
5	Synopsis .....	- 107 -
5.1	Introduction .....	- 107 -
5.2	How does the surface morphology of a fault influence the frictional stability?-	107 -
5.3	How does the stiffness normal to the fault zone influence the occurrence and nature of slip instabilities? .....	- 108 -
5.4	At the Hikurangi subduction zone margin, how does lithology control the occurrence of the observed shallow slow slip events .....	- 110 -
5.5	How can our findings be applied to natural faults?.....	- 111 -
5.6	How are fault zone roughness, fault normal stiffness and lithology related, and how do they influence each other?.....	- 113 -
5.7	Conclusions .....	- 116 -
5.8	Open questions and future research.....	- 117 -
6	References .....	- 119 -

7	Acknowledgements .....	- 130 -
8	Versicherung an Eides Statt / Affirmation in lieu of an oath .....	- 131 -

# 1. Introduction

## 1.1. Aims and objectives

Earthquakes and the additional natural disasters that they can trigger, such as landslides and tsunamis, are among the most destructive events that occur. Although yearly numbers vary greatly, the WHO estimated an average of ~37 500 deaths per year were caused by earthquakes in the period 1998-2017<sup>1</sup>. According to the USGS<sup>2</sup> about 500 000 measurable earthquakes occur each year, of which ~100 000 can be felt and ~100 cause damage. Forecasting when an earthquake is going to happen is still near-impossible. The locations where earthquakes happen, are however often not surprising, as they generally occur on faults of which the existence is known. On the other hand, there are fault systems that are creeping, meaning they are moving without large earthquakes, although it remains questionable if creeping is omnipresent on these faults or that it is either a transient state, or only happens close to the surface with earthquakes at depth (Harris, 2017). Other faults systems, such as the subduction zone at the Hikurangi margin, host earthquakes so slow, that they do not produce seismic waves and therefore pose no immediate treat. Repeated slow earthquakes can however also damage infrastructure on the long term (Bürgmann, 2018). Understanding why some faults show stable creep, whereas others host slow or devastating large ordinary earthquakes, is vital for making earthquake risk assessment and improves our general knowledge about earthquake mechanisms, which can then in turn also be applied in theoretical and numerical models.

Studying earthquakes is a multidisciplinary field, partly caused by the fact that earthquakes cannot be directly 'seen'. Different disciplines each approach earthquakes from a different point of view and with different methods, ranging from seismology where the seismic waves emitted by earthquakes are recorded and used to measure and locate the event, to structural geology and geomorphology looking into fault structures and traces of past earthquakes. Laboratory studies such as presented in this thesis complement those other disciplines, by studying earthquakes in a controlled environment, where the influence of specific factors can be singled out. Observations made in the laboratory can then serve as input for numerical models, that are constructed based on theoretical and empirical equations and are useful to explain the observations, test theories and to expand results to other length or time scales. Only an integrated approach spanning multiple

---

<sup>1</sup> [https://www.who.int/health-topics/earthquakes#tab=tab\\_3](https://www.who.int/health-topics/earthquakes#tab=tab_3)

<sup>2</sup> [https://www.usgs.gov/natural-hazards/earthquake-hazards/science/cool-earthquake-facts?qt-science\\_center\\_objects=0#qt-science\\_center\\_objects](https://www.usgs.gov/natural-hazards/earthquake-hazards/science/cool-earthquake-facts?qt-science_center_objects=0#qt-science_center_objects)

disciplines and methods can bring us forward in understanding the mechanisms behind earthquakes. Although laboratory studies are a simplification of natural fault systems and care should be taken to apply findings to nature, they are a crucial part in the larger cycle of earthquake studies.

In this thesis, I report on laboratory studies that explore how three variables influence the frictional behavior and stability of faults, to see which conditions promote stable sliding, slow earthquakes or fast ‘ordinary’ earthquakes. The first is fault surface roughness or fault morphology, which additional to having an effect on frictional behavior, as I show, also has the potential to scale frictional behavior from the laboratory to natural faults, since faults exhibit a certain scalable degree of roughness. The second variable studied is the fault normal stiffness, because since faults are rough, a certain fault-normal motion must accompany fault slip. The fault-normal stiffness can therefore influence fault slip behavior, in addition to a known effect of shear-parallel stiffness. The third study is a case study about the Hikurangi subduction margin in New Zealand, and focusses on the known effect lithology has on slip behavior. The Hikurangi margin hosts very shallow slow slip events, which makes it an excellent case to study, as the slow slip events that occur in laboratory experiments can be compared to the natural slow slip events.

## 1.2 Earthquakes and friction

### 1.2.1 What is an earthquake

To study the occurrence of earthquakes, we need to define and look into what exactly an earthquake is and also explore the variety of earthquakes that exist. The traditional view that earthquakes cause shaking of the ground by seismic waves, has been refined since with new instrumentation other types of earthquakes can be detected as well. Three major groups of earthquakes that are now commonly recognized are:

*Slow slip events (SSEs)* are instances of accelerated aseismic slip on a fault patch, that have a duration of minutes to decades in nature (Bürgmann, 2018). They have first been discovered using creepmeters, placed on both sides of a fault that continuously measure displacement and can therefore detect periods of accelerated aseismic slip (Bilham et al., 2004). Although initially detected mostly for continental strike-slip events, with improved methods and coverage of continuously measuring GPS stations, that can measure temporary reversals in the direction of movement (Dragert et al., 2001), slow slip events have now been detected in a wide variety of settings, including subduction zones.

*Low and very low frequency earthquakes (LFEs/VLFs)* are recognized by the low frequency, low amplitude seismic signals they emit, with no clear *P* waves (Beroza and Ide, 2011). VLFs have even lower frequencies and longer durations than LFEs, but have otherwise similar characteristics. Except for the detectable seismic waves and slightly shorter duration, LFEs/VLFs are not very different from SSEs. LFEs, VLFs and SSEs combined have been called *slow earthquakes* (Ide et al., 2007), because they are significantly slower than ordinary earthquakes.

*Ordinary earthquakes* is the name adopted for the traditional, fast earthquakes that have durations of up to a few seconds (Ide et al., 2007) and have the typical, detectable seismic signal known for earthquakes.

How slow and ordinary earthquakes are related in nature, which events may interact and which events may trigger which other type, is still an open research topic (e.g. Beroza and Ide, 2011; Obara and Kato, 2016), but not discussed in detail in this thesis. Another open question is if slow earthquakes and ordinary earthquakes are a continuous spectrum (Leeman et al., 2016), or that they follow two distinct scaling laws (Ide et al., 2007).

To study earthquakes, not only the duration and characteristics of the sliding phase are important, but the whole earthquake cycle should be considered. Ordinary earthquakes have been described as ‘stick-slip’ behavior, where a period during which the fault is locked and does not

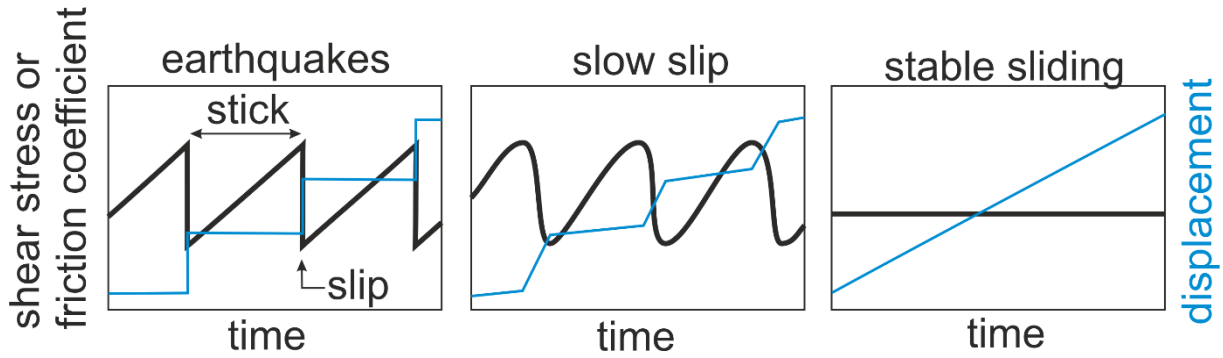


Figure 1.1: Schematic visualization of the qualitative difference in evolution of shear stress (or friction coefficient) in black and displacement in blue over time, for an ordinary earthquake (left), slow slip event (middle) and stable sliding (right)

move (the interseismic period), is followed by the sudden release of build-up shear stress as an earthquake (Fig. 1.1). For stable sliding, where there are no fluctuations in shear stress on the fault, movement on the fault is continuous and therefore fault displacement shows a steady increase. Slow slip events are in between, movement on the fault slows down in between events, but the fault does not become fully ‘locked’, where there is no measurable movement. Slip release during slow slip events is less sudden than during ordinary earthquakes, but occurs over a longer period of time. In nature, SSEs generally take weeks to months (Ide et al., 2007), but in the laboratory studies we present here, with smaller samples and higher driving velocities, SSEs may take seconds to hours (Chapter 3&4). The size of stress drops during slow slip events can be as large as for stick-slip events (Bürgmann, 2018).

## 1.2.2 Fault surfaces

When a rock breaks in a brittle manner, the new surface that forms is defined as a fault. The mechanics that determine whether or not a rock will break are described using failure criteria such as the Coulomb failure criterion for rocks under compression,

$$\tau = \mu\sigma'_n + C \quad (1.1)$$

that describes the shear strength of the rock  $\tau$  [MPa], that consists of a cohesion  $C$  [MPa] and the internal friction  $\mu$  [-] times the effective normal stress  $\sigma'_n$  [MPa] (e.g. Scholz, 2019), which is calculated from the normal stress  $\sigma_n$  [MPa] and pore fluid pressure  $P_f$  [MPa] as:

$$\sigma'_n = \sigma_n - P_f \quad (1.2)$$

The sudden breakage of rocks may be a catastrophic failure event, yet most earthquakes are not caused by the breaking of rock, but rather occur on already formed faults (Scholz, 1998). Small cracks will form in rocks under stress, which grow and coalesce to form larger faults.

surfaces. Subsequent earthquakes on faults will than make faults grow in length (Cowie and Scholz, 1992). The study of fracture mechanics and fault formation is an entire study area on its own, but earthquake mechanics can better be described by the frictional sliding of rocks over an already existing fault surface. On an already developed fault surface, it can be assumed that the cohesion  $C$  is negligible, which simplifies equation 1.1 so that the friction coefficient represents the ratio between shear stress and effective normal stress:

$$\mu = \frac{\tau}{\sigma_n'} \quad (1.3)$$

Fault surfaces are not perfectly planar, which means that on two opposing sides of the fault surfaces, only a few points are truly in contact. These contact points are called contact asperities or just asperities, and together they form the real area of contact (Fig. 1.2). The real area of contact is generally only a few percent of the total area (Dieterich and Kilgore, 1994). This is the central concept in Bowden and Tabor's (1950) adhesion theory of friction, in which they propose both normal stress and shear stress can be related to the contact area, by the penetration hardness  $P$ , and shear strength of the asperity  $S$ . The friction on the fault surface,  $\mu$ , is defined as the ratio between those two:  $\mu=S/P$ . The friction coefficient does not depend on contact area, which

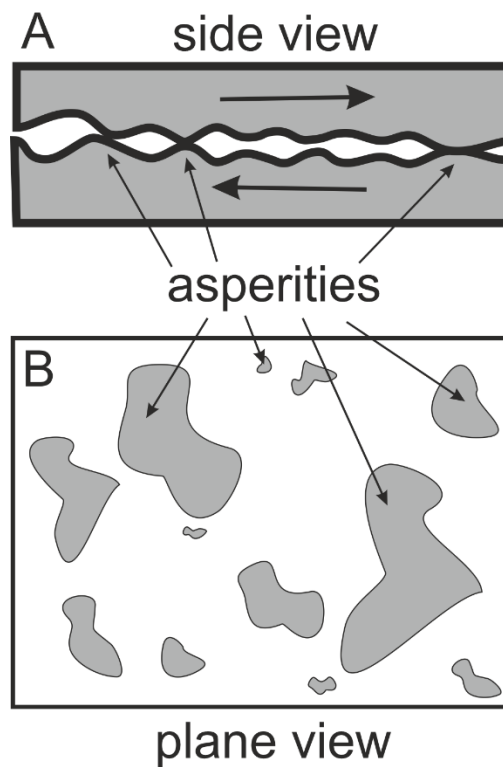


Figure 1.2: surface asperities, A: side view of a fault, B: top view of a fault where only the grey areas are truly in contact. After: Scholz, (2019) figure 2.1

satisfies Amontón's first law of friction, which states that friction is independent of the contact area of the two contacting bodies (e.g. Scholz, 2019). This means that both the shear stress and the normal stress will be higher at the contact asperities than what is measured macroscopically, but the friction coefficient measured is valid for both.

The asperities on both sides of the fault may interact, which leads to resistance against sliding, or friction. When the two sides of a fault are in stationary contact, the asperities grow over time. This has been visualized by Dieterich and Kilgore (1994, 1996), but can also be inferred from laboratory experiments. Using slide-hold-slide experiments, where periods of sliding are alternated with periods of stationary contact, it can be shown that a peak in friction that occurs after sliding is resumed, grows logarithmically with the time of stationary contact (Dieterich, 1972). On the other hand, during sliding, contact asperities are continuously destroyed. Engelder and Scholz (1976) show sliding friction is combination of fracturing of the contact asperities itself and ploughing of asperities into the surface of the opposite side of the fault. Friction on a fault surface is therefore a continuous balance between asperities being destroyed during sliding and growing during stationary contact, which is the basis of the rate-and-state friction framework.

### 1.2.3 Rate-and-state dependent friction

Earthquakes are essentially an increase of sliding velocity on a fault surface, therefore the velocity dependency of friction is an important parameter that governs fault slip behavior. The velocity dependence of friction is generally measured using laboratory velocity-step measurements, where sliding velocity is step-wise increased or decreased. Friction coefficient  $\mu$  may either increase with increasing sliding velocity  $V$  (velocity-strengthening behavior) or the friction coefficient may decrease with increasing sliding velocity (velocity-weakening behavior). Velocity-weakening behavior means that sliding at higher velocities becomes increasingly energy efficient, as friction decreases, and faults may spontaneously accelerate. The development of friction after a sudden velocity increase is characterized by a direct effect in the same direction as the velocity change and a subsequent evolutionary effect in the opposite direction. The overall evolution can be described using the rate-and-state friction law (in its modern form; e.g. Scholz, 1998):

$$\mu = \mu_0 + a \ln\left(\frac{V}{V_0}\right) + b_{1,2} \ln\left(\frac{V_0 \theta_{1,2}}{D_{c1,2}}\right) \quad (1.4)$$

in which  $\mu_0$  is the friction coefficient at a reference velocity  $V_0$  [m/s], and  $a$  and  $b$  are two dimensionless empirical parameters that scale the direct and evolutionary effect.  $\theta_{1,2}$  [s] are the

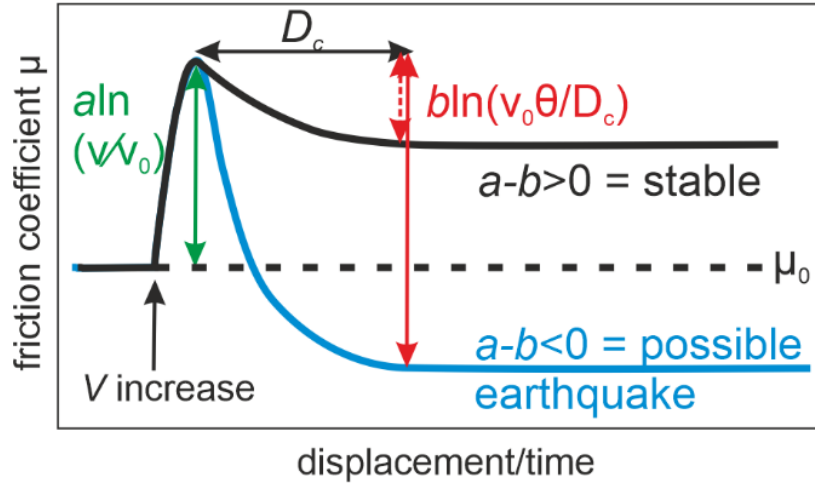


Figure 1.3: Response of friction coefficient  $\mu$  after an increase in velocity described in terms of rate-and-state friction parameters. A material with positive  $a-b$  will follow a curve like the black, whereas a material with negative  $a-b$  will follow a curve like the blue one.

state variables with units of time, that describe the state of the sliding surface, which changes over critical slip distance  $D_{c1,2}$  [m] (Fig. 1.3). In the original, mathematical formulation, the number of state variables  $\theta_i$  is not specified (Ruina, 1983) and may represent state changes due to any physical process. In practice, 1 or 2 state variables are usually sufficient to describe the frictional behavior. The most common physical interpretation on what  $\theta$  represents is the average time of contact between asperities (Dieterich, 1978). In that case,  $D_c$  represents the slip distance needed to completely refresh the population of asperities.

The rate-and-state parameters  $a$  and  $b$  are purely empirical, yet finding what they physically represent would increase the acceptance of the rate-and-state friction theory, as well as aid in the extrapolation of found data to larger scales and different temperature and pressure conditions. For parameter  $a$  the current interpretations focusses around the idea that it is related to creep at the asperity contacts, which is a rate-dependent process that can be described by an Arrhenius type of equation and depends on the temperature and the activation volume of the process (Rice et al., 2001). Parameter  $b$  is thought to represent a change in contact area due to creep in the asperities (Dieterich and Kilgore, 1994), and may be related to the healing coefficient measured during slide-hold-slide experiments (Ikari et al., 2016).

Independent of its physical meaning, the evolution of the state parameter must be described to be used in combination with the constitutive equation 1.4 in the rate-and-state friction (RSF) models. For this, several state evolution laws have been proposed, the most common ones that are used are the ‘ageing’, ‘slowness’ or ‘Dieterich’ law (Dieterich, 1979):

$$\frac{d\theta_i}{dt} = 1 - \frac{v\theta_i}{D_{ci}}, i = 1, 2 \quad (1.5)$$

and the ‘slip’ or ‘Ruina’ law (Ruina, 1983):

$$\frac{d\theta_i}{dt} = \frac{v\theta_i}{D_{ci}} \ln\left(\frac{v\theta_i}{D_{ci}}\right), i = 1, 2 \quad (1.6)$$

where the main difference between the two occurs at the condition when the sliding velocity is truly zero. For the ageing law, when the fault is in true stationary contact, the state variable develops logarithmically with time, as was observed for slide-hold-slide healing experiments (section What is an earthquake). The slip law on the other hand requires slip for contacts to evolve, which raises the question if slip on a stressed contact ever is truly zero or that it only diminishes to very small values, where a non-zero shear stress always drives displacement to relieve the stress. Another major difference between the ageing and slip evolution laws is that the slip law is symmetric for up-steps (velocity increases) and down-steps (velocity decreases), whereas the time-dependent nature of the ageing law induces asymmetry between up-steps and down-steps (Marone, 1998).

Several other state evolution laws have been proposed, such as the ‘PRZ’ evolution law that combines features of the slip and ageing evolution laws (Perrin et al., 1995), or evolution laws that include an additional effect to give a better match to specific observations, such as the Nagata law that is a modification of the ageing law, but includes stressing rate (Nagata et al., 2012). Other works focus on the physical processes occurring during sliding, and try to model velocity steps based on constitutive equations for the processes happening in a microphysical model of a shear zone, yielding good results for that particular set-up (Chen and Niemeijer, 2017). Generally, these alternative evolution laws can give better results for specific conditions, but the relative simplicity of the ageing and slowness law and their application to various settings, make them still the most widely used.

Independently of which evolution law is used, during steady-state sliding, when the state is constant and  $\frac{d\theta_i}{dt}$  is zero, equation 1.4 reduces to:

$$a - b = \frac{(\mu - \mu_0)}{\ln(\Delta V)} \quad (1.7)$$

so that the difference in steady state friction coefficient over a change in velocity  $\Delta V$  can be described by the difference between the two parameters  $a$  and  $b$ . Velocity-weakening behavior is characterized by a negative  $a-b$  value, whereas positive  $a-b$  values indicate velocity-strengthening behavior.

### 1.2.4 Spring-slider models

Whether or not a velocity-weakening fault will display unstable slip events, depends not only on the velocity-dependent behavior, but also on the rate with which a fault can unload stress with displacement, or the stiffness, compared to its surroundings. For this, fault motion can be considered as a single degree of freedom elastic system of a frictional fault in elastic or viscoelastic medium (Cook, 1981; Ruina, 1983; Gu et al., 1984). A common simplification to depict this idea is the spring-slider model, where a slider of a given mass that exerts a normal stress on the sliding surface, is pulled by a spring, with stiffness  $k$  [MPa/m] (Fig. 1.4). If a very stiff spring pulls the slider, it will move continuously and sliding is called conditionally stable. If a more compliant spring is used, pulling on the spring will first extend the spring, and only when sufficient shear force is stored in the spring, will the slider jump forward, unloading the spring. Repeated cycles of loading and unloading the spring gives stick-slip behavior, which is thought to represent earthquakes. Of interest in this framework is the exact value of stiffness where the transition from stable sliding to stick-slip cycles occurs. To find that specific stiffness, the shear force in the spring  $\tau$  can be described as a function of the stiffness in the spring  $k$  and the motion of the load point ( $V_{lp}$ ) relative to the slider ( $V_{slider}$ ) over time:

$$\frac{d\tau}{dt} = k(V_{lp} - V_{slider}) \quad (1.8)$$

Given a constant load point velocity and assuming a change in shear stress decays over a distance  $D_c$ , based on the formulation of  $D_c$  as a distance over which friction or shear stress decays to a new level, the critical value of the spring at which instabilities may occur  $k_c$  is given by:

$$k_c = \frac{v}{D_c} \frac{d\tau}{dt} \quad (1.9)$$

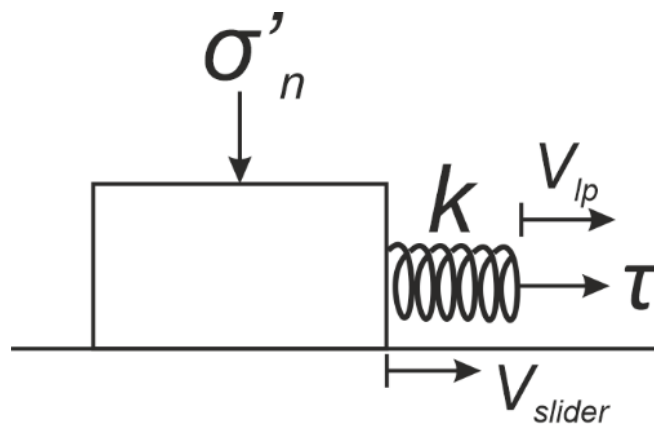


Figure 1.4: Spring-slider model where the mass of the slider exerts a normal stress on the sliding surface. Slider is pulled by a spring with stiffness  $k$ , with a constant load point velocity  $V_{lp}$ , whereas slider velocity  $V_{slider}$  may vary.

This is a generic equation, independent of the specific formulation of friction laws. As explained by e.g. Rice and Ruina (1983), there is a second term to this equation related to the inertia of the slider, which is generally neglected. Applying this instability criterion to the description of how shear stress or friction changes over time according to the rate-and-state friction equations, as first formulated by Ruina (1983), gives:

$$k < k_c = \frac{(b-a)\sigma'_n}{D_c} \quad (1.10)$$

where in laboratory experiments, the stiffness of the spring  $k$  is the stiffness of the testing device. For natural faults,  $k$  depends on the size of the slipping fault patch and the elastic modulus of the surrounding rock.

Numerical models based on this formulation have aided in predicting what kind of behavior is expected under what conditions. Ruina (1983) give numerical simulations for different values of  $k$  to show that indeed a transition occurs from stable sliding when  $k > k_c$  to stable oscillations when  $k = k_c$ , to large stick-slip events when  $k < k_c$ , upon a small velocity perturbation. Others who follow a similar approach to investigate the effect of different factors on this criteria include the effect of inertia, which adds a second term to equation 1.10 and therefore including inertia will make the system more unstable (Rice and Ruina, 1983). Including a second state variable in the formulation causes stable oscillations not only for a single value of  $k$  where  $k = k_c$ , but for a range of values where  $k$  is only slightly smaller than  $k_c$ . Large enough velocity perturbations may however trigger unstable slip events under all conditions, but these will eventually decay to stable sliding (Figure 1.5 & Gu and Wong, 1991).

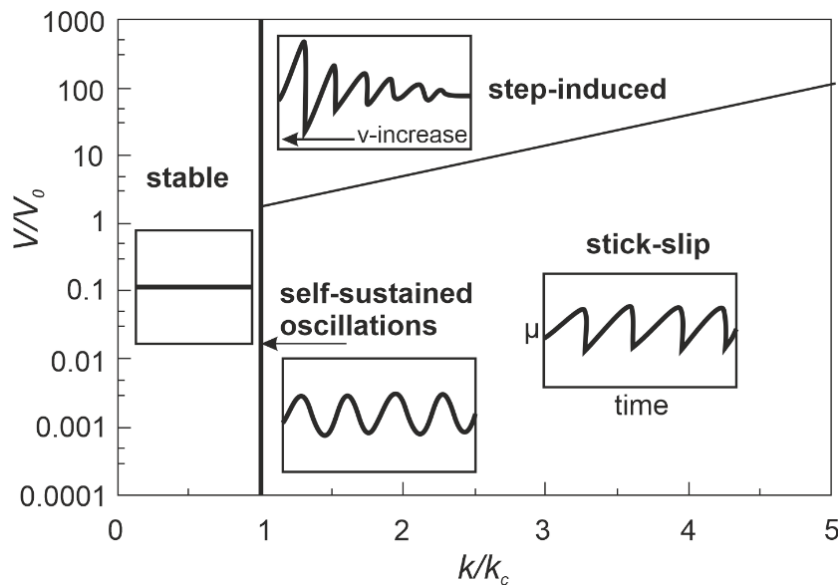


Figure 1.5: the frictional behavior in laboratory experiments depends on the ratio between  $k$  and  $k_c$  and the size of the velocity step. After: Gu and Wong (1991)

These theoretical considerations have been tested in laboratory experiments, such as spring-slider measurements by Baumberger et al. (1994), where increasing the driving velocity or weight of the slider (normal stress) triggers oscillations or stick-slip behavior. More complex testing devices use a layer of gouge material that is squeezed between two forcing blocks, which represents a layer of fault gouge. The experiments show the same transition in sliding behavior using a range of normal stresses, in combination with different forcing blocks of more or less compliant materials (Leeman et al., 2016) or by including a spring in the shear force chain (Scuderi et al., 2016b). This allows for systematic studies of slow slip events such as the sliding velocities and frictional properties of the shear zone (Leeman et al., 2018), emitted seismic waves during the full spectrum of slip events (Scuderi et al., 2016b) and the influence of shear zone fabric (Scuderi et al., 2017). These last studies (Leeman et al., 2016, 2018; Scuderi et al., 2016b, 2017) also link the transition in slip events observed in the laboratory to the spectrum of fault slip observed in the field, where rapid stick-slip represents ordinary earthquakes and the stable oscillations represent slow slip events, which had not yet been discovered when those stable oscillations were first described in the laboratory.

### 1.2.5 Slipping fault patches

The spring-slider model, although useful, is an oversimplification of natural faults. One of the main differences is that in the spring-slider system, just like on laboratory samples, slip is distributed homogeneously, whereas in natural faults, the ends of a fault will slip less than the central part. Another difference is that for a slider or small laboratory sample, the whole surface will slip rather simultaneously, whereas in natural faults, slip propagates. On natural faults slip propagation was hypothesized from the observation that the time during which a single location slips, the rise time, is shorter than the overall duration of the slip event (Kanamori and Anderson, 1975; Heaton, 1990). This has led to a model of slip propagating as a pulse during an earthquake, where only a part of the fault slips at a time (Heaton, 1990). The propagation of slip is mainly driven by the dynamic stress drop that occurs (Andrews and Harris, 2005). Slip propagation has also been shown using larger laboratory samples, where slip is measured on various places on the fault surface (Johnson and Scholz, 1976).

Earthquakes are best described by separate, consecutive phases: an initial perturbation in the velocity, a nucleation phase during which the event grows and a runaway to dynamic propagation, where sliding is inertia-controlled (Ohnaka et al., 1986; Ellsworth and Beroza, 1995; Roy and Marone, 1996; Perfettini and Ampuero, 2008). Whether the instability develops into an

earthquake depends on whether during the nucleation phase the event grows to a critical patch size (Ohnaka et al., 1986; Perfettini and Ampuero, 2008). To find the critical patch size  $L_c$ , the critical stiffness equation (Equation 1.10) can be rewritten using the host rock stiffness as  $k = \eta G/L$ , in which  $G$  is the shear modulus of the rock [MPa],  $L$  is the radius or half-length of the patch [m] and  $\eta$  is a geometrical constant (Dieterich, 1992; Scholz, 1998):

$$L_c = \frac{G\eta D_c}{(b-a)\sigma'_n} \quad (1.11)$$

That slip instabilities occur once the nucleation zone has reached this critical patch size has been shown in experimental studies (Ohnaka et al., 1986) and by early numerical models (Dieterich, 1992). More recent numerical modelling studies have however revealed that there may be more than one length scale that controls slip instabilities (Rubin and Ampuero, 2005; Ampuero and Rubin, 2008; Perfettini and Ampuero, 2008).

### 1.2.6 Friction on natural faults

Applying these concepts to nature involves considering various different aspects that influence friction simultaneously, many of which change with depth, such as temperature, pressure and mineralogical changes due to metamorphic reactions. For earthquake occurrence, especially the evolution of the velocity dependence of friction  $a$ - $b$  with depth is of importance. Shallow, unconsolidated sediments are velocity-strengthening (Marone and Scholz, 1988). The depth at which a transition to velocity-weakening occurs depends on the setting and is deeper for subduction zones than for continental faults (Fig. 1.6, Scholz, 1998).

The depth at which  $a$ - $b$  changes from positive to negative, is also the depth at which the critical stiffness  $k$  changes from negative to positive, where positive values for  $k_c$  are needed to satisfy the criterion  $k < k_c$  (equation 1.10), which describes the conditions at which earthquakes can occur.  $k$  also changes with depth, because the material surrounding the fault also gets stiffer with consolidation (Fig. 1.6, Marone and Saffer, 2015). The exact number for  $k$  depends on the size of the fault patch as well, but figure 1.6 shows qualitatively how both  $k$  and  $k_c$  develop with depth, where the details vary depending on the material, geotherm and local conditions.

As temperature increases with depth,  $a$ - $b$  starts to increase again to positive values when the temperature is reached where crystal plasticity starts and ductile deformation becomes the prevailing deformation mechanism over brittle deformation (Scholz, 1998), and  $k_c$  decreases accordingly (Fig. 1.6). The temperature of the onset of crystal plasticity is the important factor

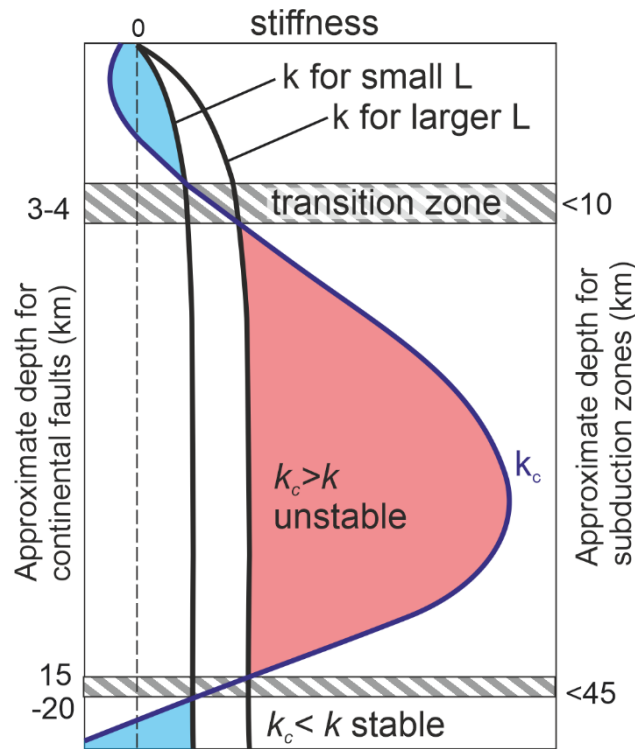


Figure 1.6: Qualitative representation how both  $k$  and  $k_c$  evolve with depth, where the depth range where  $k_c > k$  can host earthquakes. Combination of Scholz (1998) and Marone and Saffer (2015)

here, which depends on the type of crystals present and therefore the lithology of the fault, and the local geotherm.

Together, these two transitions define a depth range at which earthquakes are possible, called the seismogenic zone. In this theoretical and simplified model of the earth's crust, combined with the theoretical framework described before, transitional behavior like slow slip events would be expected in the transition zones between stable and unstable sliding, which they generally do (Saffer and Wallace, 2015). However, fault zones rarely follow the ideal case presented above. Fault zone heterogeneity, differences in lithology and fault zone structure between different faults or along-strike the same fault, are among the factors that influence stability (Skarbek et al., 2012; Zielke et al., 2017; Barnes et al., 2020). This thesis is dedicated to study the influence of three variables on the stability regimes on fault surfaces.

## 1.3 The studied variables

### 1.3.1 Fault surface roughness

Fault surfaces might macroscopically appear planar, on the microscopic level they contain a certain roughness, which gives rise to the contact asperities as described in section Fault surfaces. The most commonly known structures on fault surfaces may be slickensides, a set of grooves that are parallel to the sliding direction and can therefore be used as a kinematic indicator (Doblas, 1998). The roughness of a fault surface decreases when ‘zooming out’, but it generally does so following a self-affine fractal scaling law, meaning that a single equation can be used to describe the roughness of a fault over a large range of (wave)lengths (e.g. Brown and Scholz, 1985; Power et al., 1987; Power and Tullis, 1991). With the development of 3D scanning techniques such as LIDAR (Light Detection and Ranging) and photogrammetry (e.g. Bistacchi et al., 2011) or 3D seismic imaging (Kirkpatrick et al., 2020), measurements of the roughness of natural faults have increased during the last decades (e.g. Renard et al., 2006; Bistacchi et al., 2011; Candela et al., 2012).

That roughness influences certain frictional parameters such as frictional strength, slip stability and critical slip distance  $D_c$  has already been proven (section 2.2). However, in contrast to the majority of earlier work, the starting roughness is controlled in the experimental set-up used in this thesis. Instead, faults with a certain roughness form spontaneously upon shear, that is afterwards measured. The spontaneous localization and fault formation ensures that the roughness that forms follows the specific self-affine roughness relationship needed for scaling. Therefore explaining the frictional behavior of small laboratory faults in terms of surface roughness can be directly scaled and applied to large natural fault surfaces. This motivated the study of how fault surface roughness influences frictional sliding behavior (Chapter 2). However, that faults are rough has various side-effects, as we will see in chapters 3 and 4.

### 1.3.2 Fault normal stiffness

One of the side-effects of rough faults, is that slip parallel to the macroscopic fault surface must be accompanied by some movement perpendicular to the fault surface (dilation), to overcome the roughness. It has been previously shown that faults dilate and compact during loading/unloading (Marone et al., 1990) and during the seismic cycle (Scuderi et al., 2016a). Whereas the influence of stiffness parallel to the fault surface (the shear direction) is known to have a large influence on sliding behavior, as is explained in section Spring-slider models, the

effect of stiffness in the direction normal to the fault surface has not been explored yet. Because some degree of slip normal to the fault must occur during slip instabilities, I investigate the effect fault normal stiffness has on the instabilities that occur. Since I control the fault-normal stiffness on one side of the fault, this introduces an asymmetry in fault stiffness. When a contrast in elastic properties across a fault surface exists, the fault should be described as a bimaterial interface rather than slip in a homogeneous solid. Slip on a bimaterial interface is fundamentally different from slip in a homogeneous solid.

### 1.3.3 Lithology

The effects lithology has on frictional behavior are multiple and complex, where the interaction of the different effects is also not entirely understood yet. The friction coefficient  $\mu$  (equations 1.4 & 1.7) of natural fault gouges with different compositions, has been shown to vary between 0.2 and 0.7 (Carpenter et al., 2016). One clear influence on the friction coefficient is the component of phyllosilicate minerals, which are significantly weaker than other minerals, especially when wet (Logan and Rauenzahn, 1987; Morrow et al., 2000). The main influence of frictional strength is that large faults often form in the lithologies with low frictional strength, as faulting in those requires the least energy. There is a correlation between frictional strength and the velocity-dependency of friction  $a-b$  (Ikari et al., 2011, 2016). Also for  $a-b$  there is a marked difference between phyllosilicate minerals, which generally show velocity-strengthening behavior and other minerals, which can show velocity-weakening behavior. The reason for the low friction and positive or small  $a-b$  values in phyllosilicate minerals include their structure as sheet silicates and the low bond strength between the sheets (Morrow et al., 2000) and low healing rates (Carpenter et al., 2016). The effects of other factors have on friction, such as temperature, may also vary with lithology. Frictional behavior measured during experiments is therefore always specific for the tested lithology and extrapolating findings to other lithologies is difficult.

The question how lithology influences sliding behavior is therefore too broad to answer in this thesis. Instead, we focus on a specific problem, a case study about the Hikurangi margin, a subduction zone offshore the east coast of the northern island of New Zealand. This subduction zone is special because slow slip events occur relatively shallow, they have been shown to continue to within 2 km of the seafloor (Wallace et al., 2016). During IODP (International Ocean Discovery Program) Expedition 375 to the Hikurangi margin in 2018, the undisturbed lithologies on the incoming plate were drilled, as one of the research aims. Input sediments are accurate representatives of the lithologies in the subduction zone, because they have a similar mineralogy and grain size, and a similar pre-subduction burial and deformation history. In case of the

Hikurangi margin, the shallow nature of the SSEs means that the in-situ conditions of the input sediments do not differ substantially from the in-situ conditions of the sediments that host the SSEs. Using the input sediments, I can therefore answer the question in which lithology the shallow SSEs that are observed at the Hikurangi margin occur. Knowing in which lithology the SSEs occur is an essential first step in understanding these shallow SSEs.

## 1.4 Research questions

Related to the variables studied, I define five research questions:

1. How does the surface morphology of a fault influence the frictional stability?
2. How does the stiffness normal to the fault zone influence the occurrence and nature of slip instabilities?
3. At the Hikurangi Subduction zone margin, how does lithology control the occurrence of the observed shallow slow slip events?
4. How can these findings be applied to natural faults?
5. How are fault zone roughness, fault normal stiffness and lithology related, and how do they influence each other?

## 1.5 Outline and author contributions

After this general introduction (Chapter 1), the outline of the thesis is structured as follows:

Chapter 2 focusses on research question 1 and explains how surface roughness and especially the shape of the contact asperities on a fault surface, can be related to the frictional behavior of the fault. An additional aspect of this chapter is that surface roughness can be used as a tool to relate laboratory findings to natural faults. One of the main problems with extending laboratory-measured values to natural faults is a scaling issue. Surface roughness obeys specific fractal scaling laws, that are applicable over lengths scales ranging from mm's to hundreds of km's and can therefore be used to relate cm-scale laboratory samples to natural faults that may be km's in length.

A shortened version of this chapter has been submitted to the journal *Geology*. Additional authors that contributed to this manuscript besides me, are James Kirkpatrick, François Renard and Matt Ikari, and author contributions are divided as follows: Matt Ikari initiated the project

and acquired the Confocal Laser Scanning Microscope as part of the larger PREDATORS project under ERC grant #714430, which was required to execute this research, because it enabled the measurements of surface roughness. Matt Ikari helped me with the development of the experimental plan, data interpretation and manuscript writing. James Kirkpatrick's contribution to the project was introducing me to the method of surface roughness analysis, discussing the data analyses and he made suggestions to improve the manuscript. François Renard's contribution was that he hosted me at the University of Oslo, where he explained how to use and interpret data measured with the White Light Interferometer, a different method to measure surface roughness, to measure certain surface roughness attributes more accurately (specifically  $L_c$ ) and to validate the results measured with the newly acquired Confocal Laser Scanning Microscope in Bremen. François also made useful suggestions to improve the manuscript. My own contribution is that I developed the experimental plan, carried out the friction experiments and analyzed the frictional data. Also, I developed the method to measure surface roughness with the Confocal Laser Scanning Microscope, analyzed the measured roughness data, related the two measured parameters and I wrote the first version of the manuscript, after which it was improved by suggestions from all co-authors.

Chapter 3 aims to answer research question 2 and looks at the influence the stiffness normal to the fault has on frictional sliding behavior and the occurrence of slip instabilities. In the introduction (section 1.2.4) it is explained how stiffness in the direction parallel to shear has a direct influence on the sliding behavior of a velocity-weakening fault. Since all faults have a certain roughness, fault slip parallel to the macroscopic fault surface to relieve the shear stress, must be accompanied by a certain degree of movement normal to the fault. I therefore propose that decreasing the stiffness normal to the fault surface promotes unstable sliding.

The other author that contributed to this chapter besides me, is Matt Ikari, who advised on the research idea and experimental plan, commented on the manuscript, and supervised and financed the project. My contribution to this manuscript consists of coming up with the initial research idea, designing and executing the experiments, analyzing and interpreting the data and writing the manuscript.

Chapter 4 focusses on research question 3 and is about the SSEs in the Hikurangi subduction zone and describes the frictional behavior of the lithologies entering the subduction zone at plate-rate deformation rates. Because the SSEs in the Hikurangi margin are relatively shallow, the input sediments have a similar microstructural and mineralogical structure as the lithology at the depth where the shallow SSEs take place. I test the main lithologies at realistic plate-rate deformation rates, because the velocity-dependence of friction, described by parameter  $a-b$  varies with velocity

and values measured at deformation rates commonly used in laboratory experiments of  $\mu\text{m}'\text{s}$  per second are not necessarily representative for the frictional behavior at realistic plate-rate deformation rates of  $\text{cm}/\text{year}$  or  $\text{nm}'\text{s}$  per second.

Except for me, also Matt Ikari contributed to this manuscript, by coming up with the initial research question, so that personal samples in the name of MI, collected during IODP Expedition 375, in which he took part, could be used for this research. Matt Ikari helped with developing the experimental plan, data interpretation, helped write the manuscript and supervised and financed the project. My contribution to this manuscript was refining the research question, selecting the samples, designing the experimental plan, carrying out the experiments and analyzing and interpreting the data. I wrote the initial manuscript which was improved with comments from Matt Ikari.

Chapter 5 summarizes the main findings chapters 2-4, answers the last two research questions of this thesis and concludes the thesis.



## 2 Fault surface morphology as an indicator for slip stability

*Agathe M. Eijsink<sup>1</sup>, James D. Kirkpatrick<sup>2</sup>, François Renard<sup>3,4</sup> and Matt J. Ikari<sup>1</sup>*

- 1) *MARUM, Center for Marine Environmental Sciences, University of Bremen, D-28359 Bremen, Germany*
- 2) *Department of Earth & Planetary Sciences, McGill University, 3450 University Street, Montréal, Québec H3A 0E8, Canada*
- 3) *Njord Centre, University of Oslo, 0316 Oslo, Norway*
- 4) *University Grenoble Alpes, CNRS, ISTerre, 38000 Grenoble, France*

### 2.1 Abstract

Laboratory measurements can determine the potential for geologic materials to generate unstable (seismic) slip, but a direct relation between the sliding behavior in the laboratory and physical characteristics observable in the field is lacking, especially for phyllosilicate-rich gouges that are widely observed in natural faults. Here, we integrate laboratory friction experiments with surface topography microscopy and demonstrate a correlation between frictional slip behavior and fault surface morphology. Our results show that stable sliding is favored on striated, smooth fault surfaces, whereas potentially unstable sliding is associated with rougher, isotropic fault surfaces. We interpret that frictional stability and fault surface morphology are linked via the evolution of asperity contacts across slip surfaces. Because fault surface roughness obeys a fractal relationship over a large range of length scales, we infer that the morphological characteristics observed in the laboratory can be used to indicate the tendency for unstable slip on natural fault surfaces.

### 2.2 Introduction

Earthquakes and landslides, which both occur due to unstable fault slip, occur on fault surfaces that are many orders of magnitude larger than typical laboratory samples used to measure the behavior of frictional sliding. To apply laboratory findings to real-world faults, the laboratory-measured parameters have to be related to measurable quantities that can be extrapolated over a wide range of length scales. Laboratory friction experiments have provided the basis for a theoretical framework that predicts the stability of a slipping fault via measurements of velocity-dependent frictional strength (Marone, 1998). However, a clear connection between friction parameters and physical quantities observable in the field is lacking and, although evidence of past earthquakes can be found in the rock record (e.g. pseudotachylytes) (e.g. Rowe and Griffith, 2015), physically-observable pre-existing features on fault surfaces that indicate the ability to

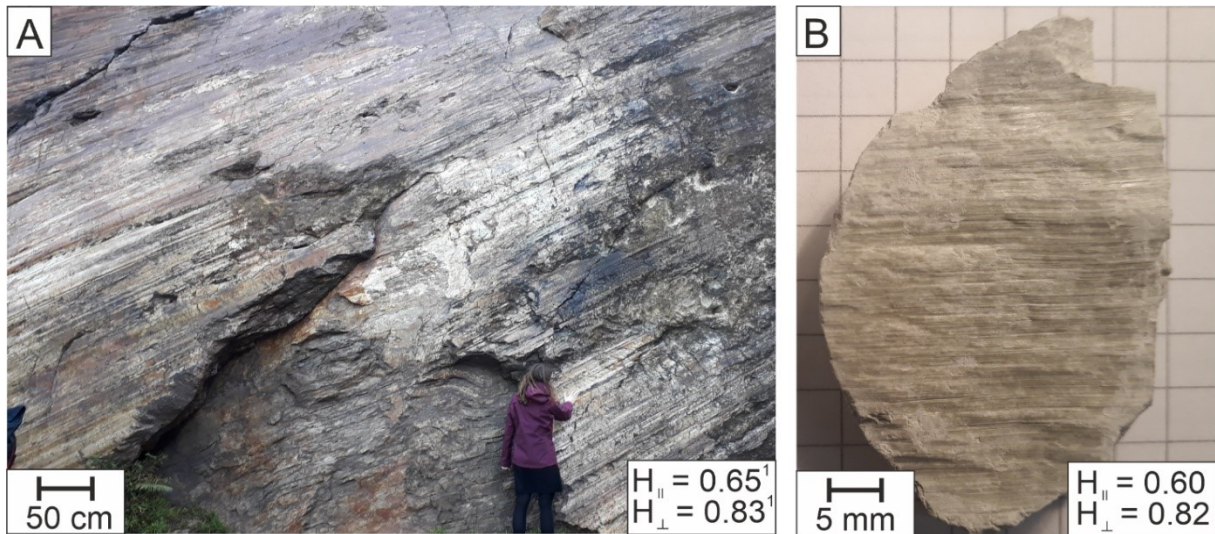


Figure 2.1: Fault striations on multiple scales. A: The Corona Heights fault (San Francisco, CA), showing large-scale striations. Hurst exponents from (Candela et al., 2012). B: Fault recovered in drill core from the Hikurangi margin (New Zealand), sample U1520C-5R2 (Wallace et al., 2019).

repeatedly generate seismic slip have not yet been identified. Fault surface morphology may be a promising tool to relate experimental observations with natural faults, because fault roughness can be measured relatively easily both in the field and in the laboratory (e.g. Candela et al., 2012). Here, we report on a relationship between fault surface roughness and frictional stability parameters, which would be applicable at length scales ranging from the laboratory to the field.

Fault surfaces, as well as other frictional slip surfaces formed by landslides (Shuzui, 2001) or glaciers (Kamb, 1970), commonly contain structures such as slickensides or grooves (Doblas, 1998), which are oriented parallel to the slip direction, and which combine to define specific topographical patterns (Fig. 2.1). It has long been recognized that the topography of fault surfaces can be described as having a self-affine fractal character across length scales of several orders of magnitude (Brown and Scholz, 1985; Power et al., 1987; Schmittbuhl et al., 1993). Since the development of 3D measuring technology (Renard et al., 2006; Sagy et al., 2007), this type of topography has been shown to characterize many natural fault outcrops (Sagy et al., 2007; Bistacchi et al., 2011; Candela et al., 2012; Shervais and Kirkpatrick, 2016; Dascher-Cousineau et al., 2018) and recently in-situ faults at depth (Kirkpatrick et al., 2020). Fault surface roughness is self-affine over a large range of length scales (Power et al., 1987; Candela et al., 2012; Renard et al., 2013), suggesting the surface geometry measured on small-scale laboratory samples can be extrapolated to the much larger scales of natural faults.

Previous laboratory friction experiments have shown that artificially varying the surface roughness as a starting condition affects frictional behavior, including frictional strength (Biegel et al., 1992; Vincent-Dospital et al., 2021), slip stability (Marone et al., 1990; Harbord et al.,

2017) and critical slip distance (Okubo and Dieterich, 1984; Dieterich and Kilgore, 1996), and that these effects also depend on normal stress (Badt et al., 2016; Harbord et al., 2017). Laboratory and numerical studies that measure the surface roughness after sliding indicate that the final roughness is affected by the starting roughness (Badt et al., 2016) and that gouge presence and formation during slip decreases the frictional strength and can smoothen or produce grooves on the fault surface (Davidesko et al., 2014; Brodsky et al., 2020; McBeck et al., 2021). Recent work has shown a qualitative relationship between frictional properties and surface microstructure (Fagereng and Ikari, 2020b) and that differences in deformation mechanisms cause variations in fault surface morphology (Sagy et al., 2017).

Here, we quantify the surface roughness evolution on experimental faults composed of quartz or shale and relate roughness to the measured frictional behavior. In contrast to earlier work, we allow the fault surface morphology to develop by shearing initially undeformed (remolded) samples. In particular, the shale represents phyllosilicate-rich faults, which are common in nature but have not been previously studied in surface roughness experiments. The testing conditions (10 MPa effective normal stress and wet, but fully drained) were chosen to be representative for faults in the shallow crusts, which are the focus of this paper. However, the results can also be applied to other frictional sliding processes that occur under relatively low normal stresses, such as landslides (both subaerial and submarine) and glaciers.

### 2.3 Short method

Using a single-direct shear device (see detailed methods, 2.7), we performed two different types of friction experiments: (1) velocity-stepping experiments, where sliding velocity was alternated between 1 and 10  $\mu\text{m/s}$  every millimeter of displacement in the range 2-10 mm, and (2) shearing at a constant velocity of 10  $\mu\text{m/s}$  to a total displacement of 2-10 mm. The constant velocity experiments were performed to produce a slip surface on which we measured roughness, the velocity-stepping experiments provide the frictional data at matching displacements.

Upon a velocity ( $V$ ) change, the friction coefficient  $\mu$  evolves to a new steady-state value as (Dieterich, 1981; Scholz, 1998):

$$\mu = \mu_0 + a \ln\left(\frac{V}{V_0}\right) + b \ln\left(\frac{V_0 \theta}{D_c}\right), \quad (2.1)$$

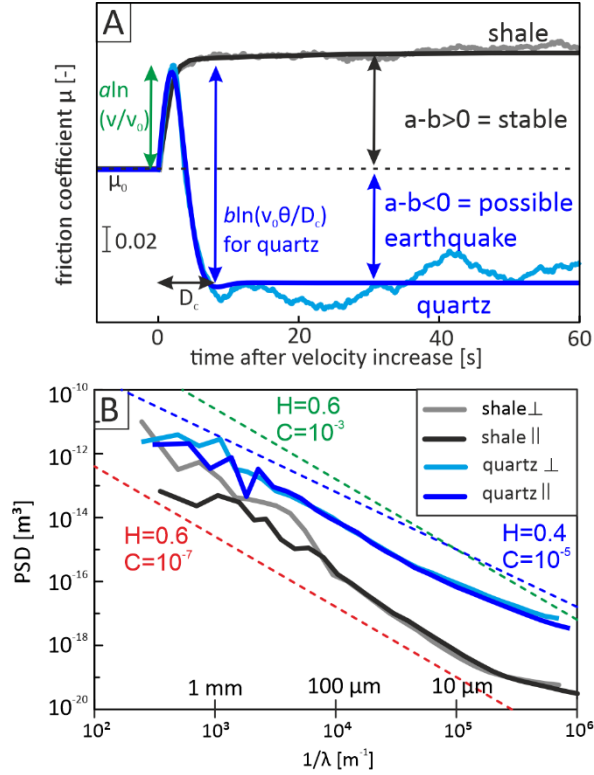


Figure 2.2: Examples of friction and fault roughness measurements. A: Frictional behavior after a stepwise velocity increase at a fixed displacement of 8 mm. Note that the quartz is velocity weakening ( $b > a$ ), whereas the shale has no clear decrease in friction after the initial increase, meaning  $b \approx 0$ , and  $a - b > 0$ . B: Power spectral density (PSD) of measured surface roughness of samples after a fixed displacement ( $d=8$  mm). PSD roughness is fit by a power law with Hurst exponent  $H$  and pre-exponential exponent  $C$  both parallel ( $\parallel$ ) and perpendicular ( $\perp$ ) to sliding. A higher PSD indicates a rougher surface, and a shallower trend, indicates a lower Hurst exponent. Note the overlapping PSD curves for the isotropic quartz and diverging curves for the anisotropic shale at wavelengths greater than  $\sim 100$   $\mu\text{m}$ .

where  $\mu_0$  is the friction coefficient at a reference velocity  $V_0$ , friction parameter  $a$  scales the direct effect on friction, and friction parameter  $b$  scales the subsequent evolution of friction, which depends on the state variable  $\theta$  (units of time) over a critical slip distance  $D_c$  (Fig. 2.2A). Once the state variable and friction coefficient have reached steady-state at the new velocity  $V$ , Equation 1 can be reduced to  $a-b = \Delta\mu_{ss}/\Delta \ln V$ , where  $\Delta\mu_{ss}$  is the change in steady-state friction coefficient (Detailed methods, 2.7). Positive values of  $a-b$  indicate that friction increases with increasing sliding velocity (velocity-strengthening), which normally leads to stable sliding, whereas negative values of  $a-b$  (velocity-weakening) are needed for unstable sliding behavior such as earthquakes. To compare the surface morphology of stably sliding and potentially unstable materials, we tested quartz powder as a representative velocity-weakening material (Logan and Rauenzahn, 1987) and powdered Rochester shale as a representative velocity-strengthening material (Saffer and Marone, 2003; Ikari et al., 2009) (Fig. 2.2A).

Surface roughness was measured with a confocal laser scanning microscope (CLSM), with some supplemental measurements made with a white light interferometer (WLI). We quantify surface roughness using the power spectral density (PSD) as:

$$PSD = C \left( \frac{1}{\lambda} \right)^{(2H+1)} \quad (2.2)$$

where  $C$  is an empirical constant,  $\lambda$  is the wavelength, that may vary over several decades of length scales, and  $H$  is the Hurst exponent (Brown and Scholz, 1985; Candela et al., 2012) (Detailed methods, 2.7.2). The PSD value at any specific wavelength measures the absolute roughness of a fault surface at that wavelength (Fig. 2.2B). The Hurst exponent is important for scaling and typically has values in the range  $\sim 0.4-1$  (Power et al., 1987; Schmittbuhl et al., 1993; Candela et al., 2012; Sagy et al., 2017) and shows an azimuthal dependence on striated fault surfaces (Lee and Bruhn, 1996; Renard et al., 2006). For  $H=1$  (self-similar) the surface appears equally rough at all scales, and lower values of  $H$  mean the surface becomes relatively smoother at larger scales (self-affine). From the Hurst exponents, we calculate a degree of anisotropy  $A$  as:

$$A = \frac{H_{\perp} - H_{\parallel}}{H_{\perp}} \quad (2.3)$$

in which  $H_{\perp}$  and  $H_{\parallel}$  represent the maximum and minimum Hurst exponents, measured perpendicular and parallel to the shear direction (Lee and Bruhn, 1996).  $H_{\perp}$  and  $H_{\parallel}$  converge below a critical wavelength  $L_c$ , which represents the minimum scale of anisotropy (Candela and Brodsky, 2016), therefore we consider  $H$  measured above this wavelength for the calculation of  $A$ .

## 2.4 Results: striations and frictional behavior

Upon sliding for displacements  $\geq 4$  mm, the shale develops smooth, clearly striated fault surfaces (Fig. 2.3A) whereas the quartz fault surfaces appear rougher and isotropic (Fig. 2.3B). The roughness measurements confirm these observations, showing that roughness at a reference length of 1 mm decreases for the shale samples during the first few millimeters of sliding, whereas the quartz is consistently rougher and the PSD height does not change (Fig. 2.3C). The Hurst exponents (Supplementary Figure 2.2) are constant at  $\sim 0.4$  for the quartz surfaces, both perpendicular and parallel to the sliding direction, resulting in a low roughness anisotropy  $A$  of  $0 \pm 0.13$  for all displacements, confirming that the quartz fault is relatively isotropic (Fig. 2.3D). The shale fault shows higher values of  $H_{\parallel}$  and  $H_{\perp}$  of  $\sim 0.6$  and  $\sim 0.8$ , which are more typical of natural fault zones (Candela et al., 2012), that diverge with increasing displacement, causing the anisotropy  $A$  to increase up to 0.25 with increasing displacement (Fig. 2.3D). The initial rapid decrease in surface roughness and increase of anisotropy in the shale coincides with a drop in friction from a peak value to an approximately steady-state value around  $\sim 4$  mm of displacement, followed by a slight slip-weakening trend (Supplementary Figure 2.1).

The frictional stability parameter  $a-b$  is negative ( $\sim -0.003$ ) for the nearly isotropic quartz and the initially isotropic shale after 2 mm displacement ( $-0.006$ ), indicating slip instabilities are possible. As anisotropy on the shale surfaces develops,  $a-b$  becomes positive ( $\sim -0.004$ ), indicating stable slip (Fig 2.3E). The difference in  $a-b$  is mainly caused by differences in  $b$ , which is close to zero for the anisotropic shale and around 0.008 for the quartz and initially isotropic shale (Fig. 2.3F and Supplementary Figure 2.3). This in contrast to  $a$ , which shows relatively constant values of around 0.004 for both the shale and the quartz. The critical slip distance  $D_c$  is relatively constant for the quartz with values of  $\sim 20$   $\mu\text{m}$ , and varies between 80 and 120  $\mu\text{m}$  for the shale (Supplementary Figure 2.3). WLI measurements of the minimum scale of anisotropy  $L_c$ , which were only successful for the more reflective shale samples, are consistently  $\sim 20$   $\mu\text{m}$  and do not vary with displacement (Fig S4). Values of  $L_c$  measured with the CLSM are more scattered, between 2 and 70  $\mu\text{m}$  for the shale and between 180 and 700  $\mu\text{m}$  for the quartz.

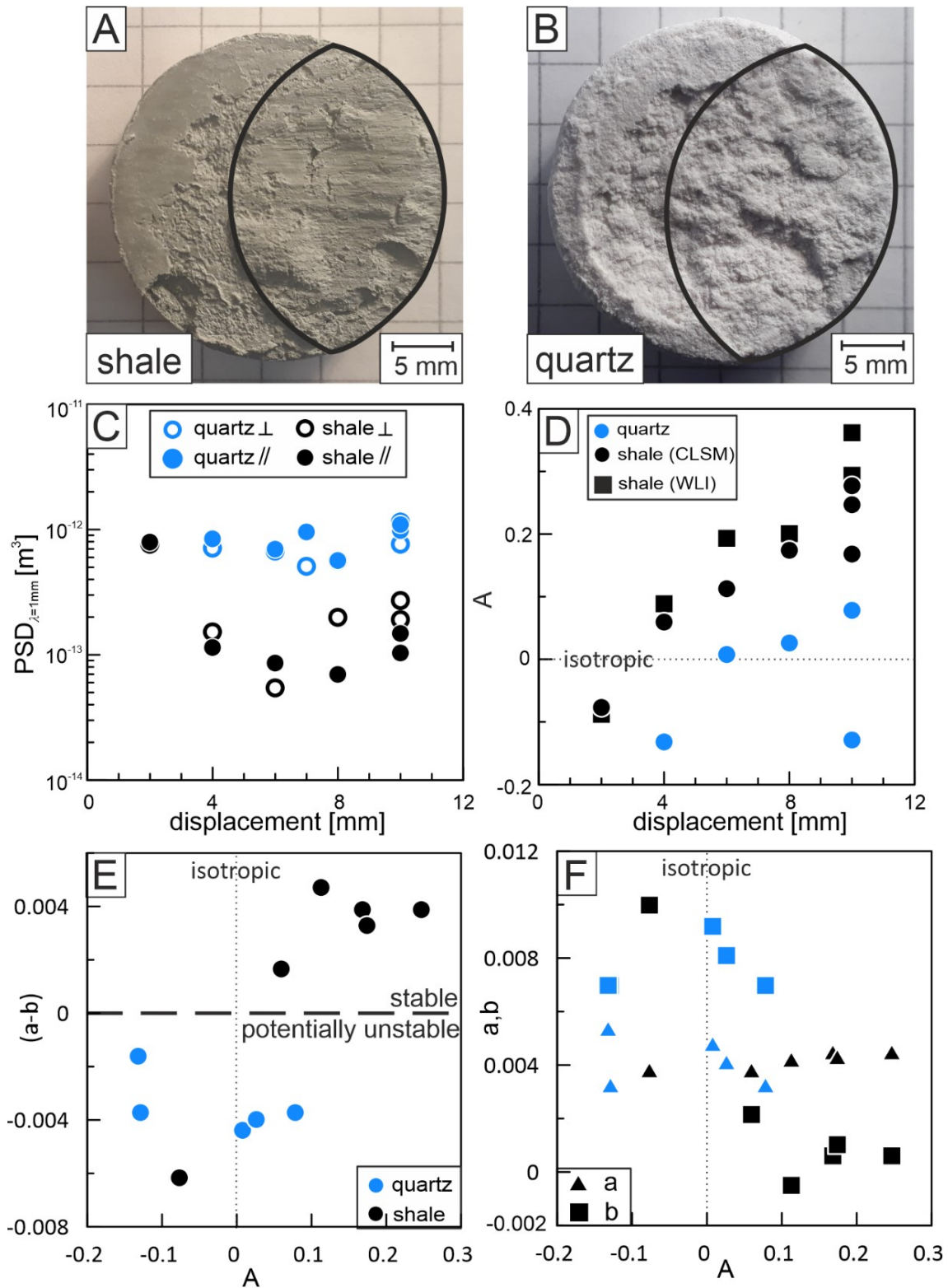


Figure 2.3: Fault roughness development with displacement. A and B: visible striations parallel to the sliding direction develop in the shale (A), but not in the quartz (B). For both samples, the displacement is 10 mm, the sliding direction is horizontal, and the sample-sample contact is outlined with black curves. C: Roughness, expressed as the power spectral density (PSD) at a wavelength of 1 mm. D: anisotropy,  $A$ . E: friction velocity dependence parameter  $(a-b)$ . F: individual friction parameters  $a$  and  $b$  as a function of anisotropy  $A$ . Except for the squares in D, the roughness values are measured with the confocal laser microscope.

## 2.5 Discussion

### 2.5.1 Validity for other materials

Our results show a clear relationship between surface roughness and frictional stability parameters; striated, anisotropic fault surfaces correspond to stable sliding, whereas velocity-weakening frictional behavior occurs on rough, near-isotropic fault surfaces. These simple systematics are consistent with previous experimental studies on a wide range of materials. For example, striated surfaces have been produced in quartz, under hydrothermal conditions where the material is velocity-strengthening and sliding is stable (Toy et al., 2017). Striated patches have been produced on limestone bare surfaces (Sagy et al., 2017) under conditions where there is no frictional healing (Tesei et al., 2017). Because frictional healing is considered necessary for slip instability (Marone and Saffer, 2015), the study by Sagy et al. (2017) also suggests that striations are related to stable slip. Direct observations of the sliding surface morphology of a single salt crystal show that frictional slip behavior stabilizes when the contact asperities evolve from initially isotropic to anisotropic and elongated (Voisin et al., 2007). Experiments on mixtures of halite and muscovite, in which a transition occurs from velocity-strengthening at low velocities to velocity-weakening at higher velocities, show simultaneous developments in microstructure from foliated to more chaotic (Niemeijer and Spiers, 2005), where foliations might represent the fault-perpendicular representation of striated and anisotropic surfaces. Therefore, the relationship we observe for shale and quartz in this study is likely applicable to a broad range of geologic materials.

### 2.5.2 Mechanism: elongating asperities

We propose that the geometric evolution of contacting asperities, which are the topographical highs on the surface, is the mechanism linking the surface roughness with frictional behavior. In the shale samples, we observe that the surface becomes preferentially smoother in the sliding direction with displacement, which produces the visible striations. This is apparent from the surface topography (Fig. 2.4A,B), which shows that the topographical highs on the shale shear surfaces become elongated with slip. In contrast, the quartz stays nearly isotropic and the surface topography shows that after 10 mm of displacement, the topographical highs on the fault surface do not become elongated (Fig. 2.4C). Based on our limited data, we estimate that positive  $a$ - $b$  values occur when the roughness anisotropy  $A > \sim 0.1$ . The velocity-weakening quartz does not reach these values, whereas the velocity-strengthening shale requires a few millimeters of displacement to reach these values.

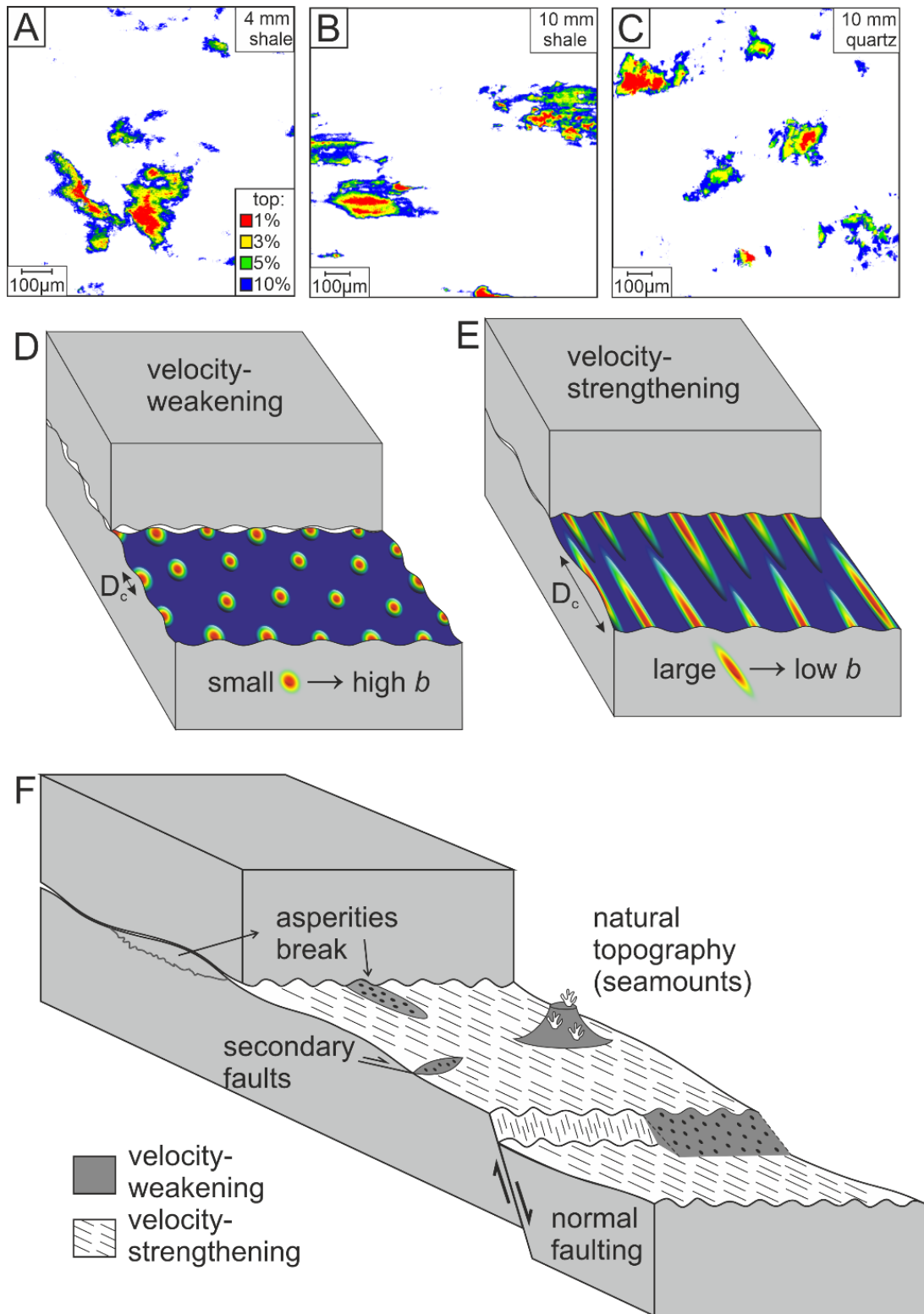


Figure 2.4: Surface deformation with increasing slip. A-C: Contact asperities size/shape for real contact areas of 1, 3, 5 or 10%, showing (A) isotropic roughness for shale surfaces after 4 mm of displacement, (B) anisotropic and elongated asperities in the shale after larger shear displacement (10 mm), (C) isotropic roughness in quartz after 10 mm displacement. Sliding direction is to the right. D-F: Schematic illustrations showing (D) isotropic fault surfaces as having small roundish asperities with normal stress highly localized at a few contacting areas, whereas striated fault surfaces (E) have elongated asperities, resulting in lower values of  $b$  and possibly larger  $D_c$  values. On natural fault surfaces (F), various processes can cause rough patches to act as asperities, which would be velocity-weakening and could host unstable slip.

Our results provide additional constraints on the relation between geometrical asperity evolution and friction, as the data clearly show that the friction parameter  $b$ , not  $a$ , controls  $a$ - $b$  for our tested materials, an effect also observed with increasing slip on salt crystals (Voisin et al., 2007). Micromechanical studies of friction suggest that the rate-dependent friction parameter  $b$  is related to the rate that real areas of contact grow with time (Dieterich and Kilgore, 1994; Ikari et al., 2016). Larger contact areas lead to lower local normal stresses at the contacts, which will then grow more slowly as a result, leading to lower values of  $b$ . We see that  $b$  is significantly smaller for the more anisotropic, striated fault surfaces in shale (supplementary figure 2.3), compared to the quartz fault surfaces. Furthermore, we measure a very large value of  $b$  for the shale at the lowest displacement, when the shale surface is still relatively rough (Fig. 2.3C) and isotropic (Fig. 2.3D). The decrease in  $b$  with slip therefore coincides with smoothing and the development of anisotropy. We therefore suggest that the elongation and flattening of asperities during slip, which mechanically increases the asperity size and therefore the contact area (Fig. 2.4D,E), is a mechanism for velocity-strengthening friction and stable slip.

The exact value for contact area on specific fault surfaces cannot be determined from surface roughness only, but depends also on factors such as material hardness and applied load (Hyun et al., 2004; Pei et al., 2005). However, the development of larger contact areas in the shale can be explained by a combination of factors: the relatively low hardness of the clay grains in the shale compared to quartz (Deirich et al., 2012) which results in larger contact areas under the same normal load (Pei et al., 2005), the platy grain shape of the illite minerals in the shale, and the intrinsically low interparticle friction of illite (Saffer and Marone, 2003; Ikari et al., 2009). In particular, the low friction of illite may facilitate easier rearrangement of grains into grooves, as proposed by Fagereng and Ikari, (2020) in a study on chlorite-epidote-hornblende mixtures, where striation development is linked to the proportion of weak chlorite. The easy rearrangement of clay minerals into striated surfaces would then explain the commonly observed velocity-strengthening behavior in this material. The relationship between friction coefficient and anisotropy development may however be limited to clay minerals. For example, although the development of anisotropy is associated with stable sliding in salt (Voisin et al., 2007) and hydrothermal quartz (Toy et al., 2017), it does not coincide with a decrease in friction and therefore must be explained by a different mechanism.

### 2.5.3 Upscaling to natural faults

The fault surfaces that developed during the laboratory experiments exhibit the same self-affine character of fault surface roughness as natural faults, which has been demonstrated to apply over eleven decades of length scales in natural systems (Power et al., 1987; Renard et al., 2013). This similarity allows for extrapolation of our measurements of frictional parameters, especially  $a$ ,  $b$ , and  $a-b$ , to natural fault surfaces. Therefore, we propose that our results provide a basis to distinguish velocity-strengthening and velocity-weakening fault surfaces in nature using surface roughness anisotropy.

Relating the friction parameter  $D_c$  to a physical quantity measurable from surface roughness is not as straightforward, due to the well-known discrepancy between laboratory-measured values of several to 10's  $\mu\text{m}$ , and values of meters inferred for natural earthquakes and on natural faults (Scholz, 1998; Kanamori and Brodsky, 2004). Previous studies have suggested  $D_c$  might represent asperity size (Dieterich, 1978; Dieterich and Kilgore, 1994), or might be equivalent to the minimum scale of anisotropy  $L_c$  (Candela and Brodsky, 2016; Okamoto et al., 2019).  $L_c$  is scale-independent, implying that  $D_c$  would not have to be scaled from the laboratory to natural faults (Candela and Brodsky, 2016). On the other hand, if  $D_c$  represents asperity size, it would have to be scaled, since on self-affine surfaces, asperity size depends on the size of the surface area considered. Our results show that  $D_c$  is in the range 80-120  $\mu\text{m}$  and  $L_c$  is  $\sim 20$   $\mu\text{m}$  for the shale, and for the quartz  $D_c$  is  $\sim 20$   $\mu\text{m}$  and  $L_c$  is  $\sim 200$   $\mu\text{m}$  (Fig S2.4). These values are sufficiently similar so that a link should be considered, but  $L_c$  is outside of the range of measured  $D_c$  values. Therefore, we cannot conclusively determine if  $L_c = D_c$  and if  $D_c$  must be scaled from the laboratory to the field.

Based on the relationship between surface roughness and frictional behavior we document here, it would be expected that striated natural fault surfaces, like the Corona Heights fault (Fig. 2.1A), will show stable sliding. Most measurements on natural fault outcrops (Power et al., 1987; Renard et al., 2006; Candela et al., 2009; Bistacchi et al., 2011) show  $H_f < H_L$ , which would indicate frequent stable sliding behavior, even though some of these faults are known to have slipped seismically (Candela et al., 2009; Bistacchi et al., 2011). This might be partly explained by a sampling bias, since striated fault surfaces are preferentially measured, or possibly represent overprinting by a late phase of velocity-strengthening sliding at very shallow depth or afterslip. Based on our results, seismic slip is not expected to originate from striated faults, but if a velocity-strengthening material is forced into the dynamic weakening regime, this might explain why some seismically-slipping natural fault surfaces are striated. This is consistent with laboratory studies

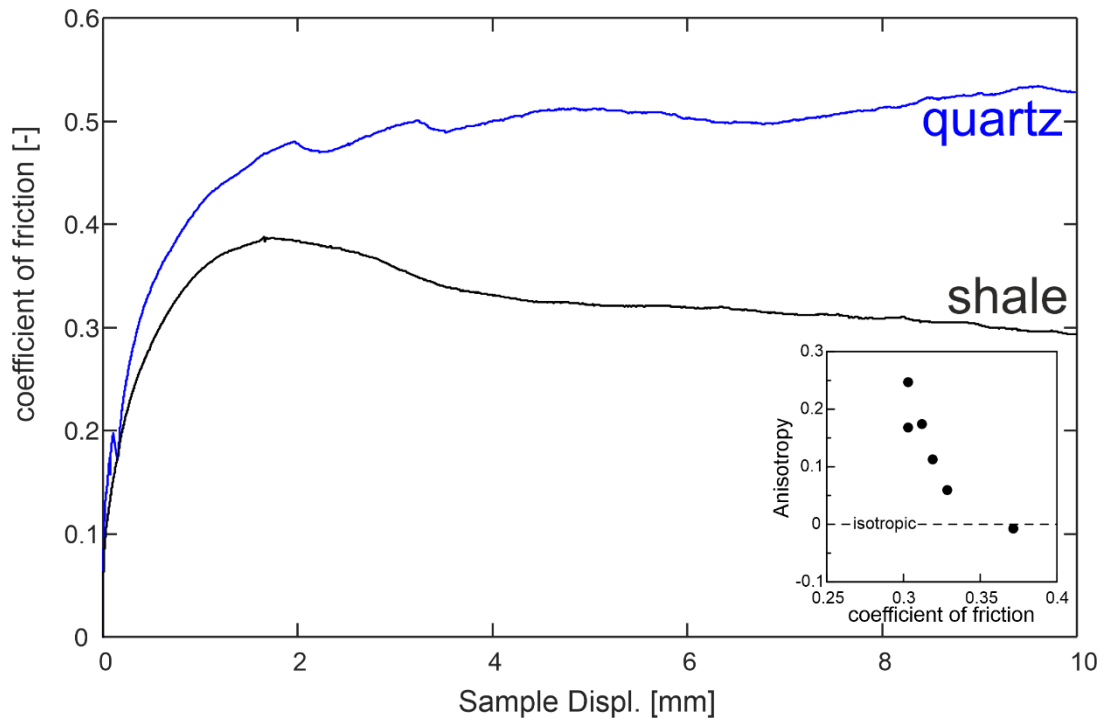
conducted at seismic slip velocities ( $\sim 1$  m/s) which can produce striated mirror surfaces after dynamic weakening (Chen et al., 2013; Fondriest et al., 2013).

Our observations are consistent with results of a recent effort to measure the in-situ roughness of an active subduction megathrust, where corrugated (anisotropic) fault patches were interpreted to slide stably and rough (more isotropic) patches were interpreted to be potential earthquake sources (Kirkpatrick et al., 2020). In Kirkpatrick et al. (2020), rough patches are formed by normal faulting which disrupts the continuity of the megathrust. Other processes across many scales (e.g. grain plucking, decapitated seamounts, intersection with secondary shear faults, asperity break-off) may cause the formation of isotropic rough patches on an overall smooth fault surface (Shervais and Kirkpatrick, 2016) (Fig 4E), where Shervais and Kirkpatrick (2016) found that the formation of new slip surfaces is probably the most important process. The scale difference between plucking of  $\mu\text{m}$ -scale grains as an important re-roughening process (Shervais and Kirkpatrick, 2016) to the km-scale rough patches visible using seismic data (Kirkpatrick et al., 2020), shows the usefulness of our relationship: surface roughness anisotropy can be measured on many scales, using a variety of measuring techniques. As a study in Costa Rica (Kirkpatrick et al., 2020) demonstrates, the relationship between  $a$ - $b$  and surface anisotropy exhibited in our laboratory experiments can be extended to natural faults, potentially with the use of remote measuring techniques over large distances and in areas where sampling may not be practical.

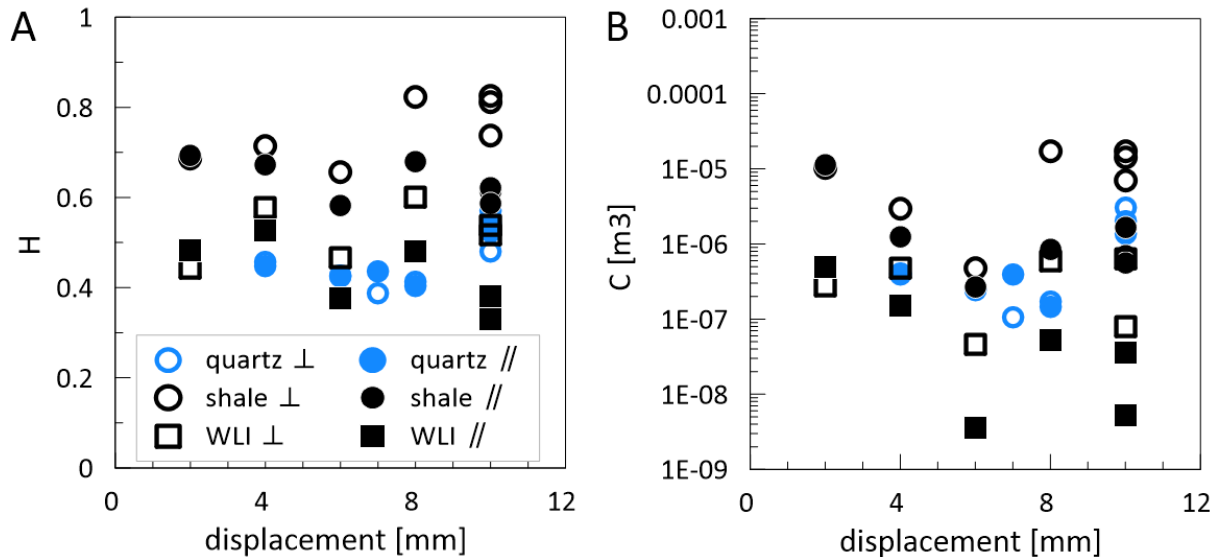
Finally, we also emphasize that relating sliding stability to surface roughness is not limited to faults and earthquake slip, but could be relevant for any process that involves frictional sliding in brittle materials. Recently, the rate and state friction system used in this study has been successfully used to describe the motion of landslides (Handwerger et al., 2016; Lacroix et al., 2020), glaciers (Zoet et al., 2013, 2020; Lipovsky and Dunham, 2017) and volcanic conduits (Dmitrieva et al., 2013). Therefore, based on the relationships presented here, sliding for these situations may also be controlled by the roughness of the shear surfaces. For example, striations have been observed in submarine landslides (Posamentier and Kolla, 2003; Gee et al., 2005) and debris avalanches generated by a volcanic flank collapse (Legros et al., 2000; Hughes et al., 2020), with the latter field study (Hughes et al., 2020) suggesting that the palaeotopography of the basal surface affects shear localization. In glaciers, bedrocks commonly show striations parallel to sliding (Kamb, 1970), which laboratory experiments have shown can form due to basal drag under velocity-strengthening sliding conditions (Zoet and Iverson, 2020). In order to confidently extend our results to these processes, systematic roughness measurements of natural landslide slip surfaces and glacier basal surfaces would be needed to determine whether they display the same

self-affine scalable roughness as fault surfaces, and to interpret the surface morphology in terms of rate- and state-dependent friction laws.

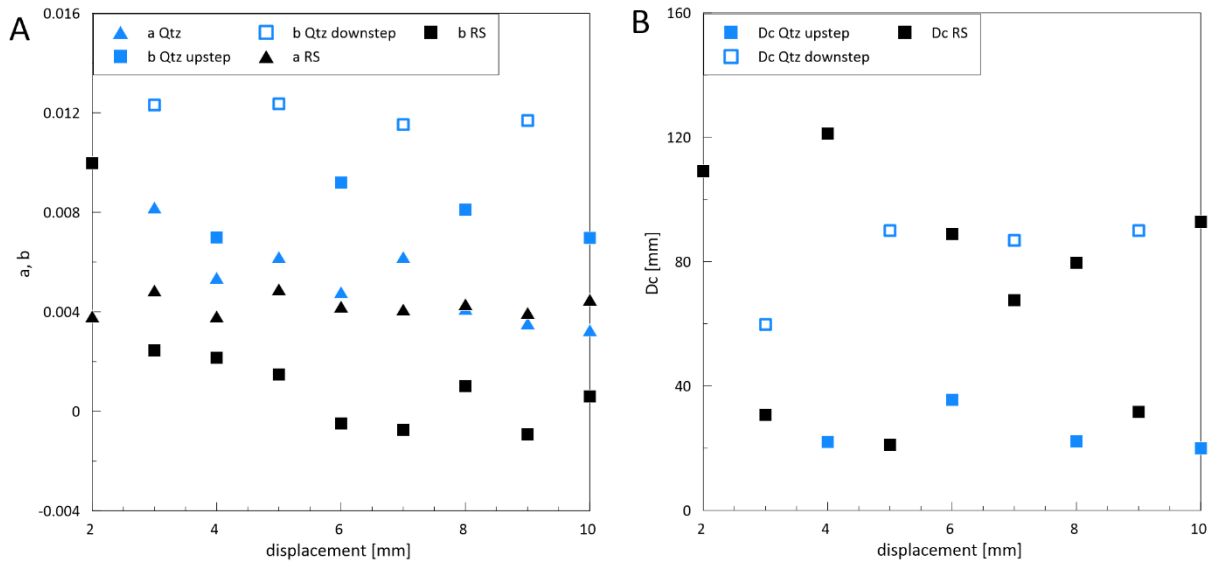
## 2.6 Supplementary figures



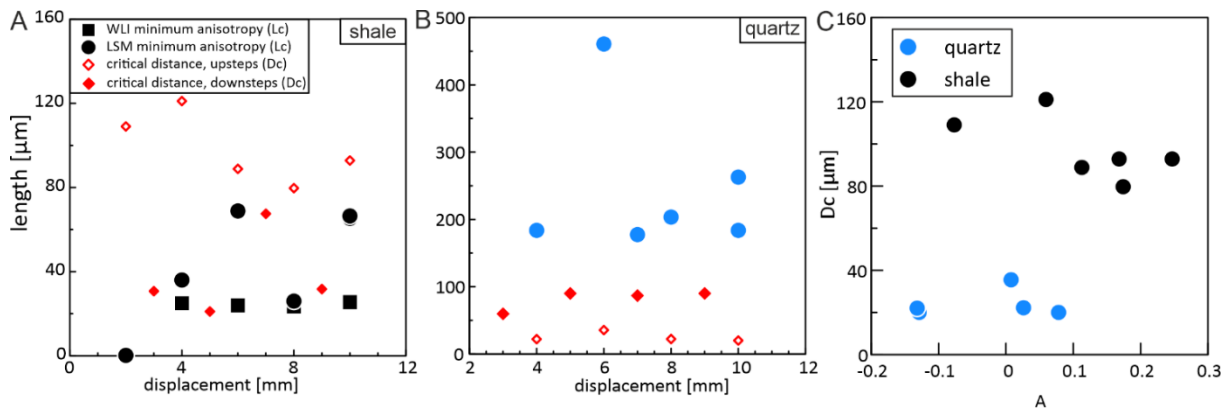
Supplementary Figure 2.1: friction coefficient  $\mu$  (shear stress divided by normal stress) over sample displacement, showing an initial run-in phase followed by steady-state sliding at friction coefficients of  $\sim 0.3$  for the shale and  $\sim 0.5$  for the quartz, with the inset showing how the development of anisotropy of the surface roughness coincides with a decrease in friction in shale.



Supplementary Figure 2.2: comparison of  $H$  and  $C$  (where  $C$  is the value of the power spectral density (PSD) curve estimated at a wavelength of 1 meter) measured with the confocal laser scanning microscope (CLSM) and the white light interferometer (WLI) on slip surfaces in shale and quartz with total slip between 2 and 10 mm.



Supplementary Figure 2.3: Friction parameters as a function of displacement. A: rate-and-state friction (RSF) parameters  $a$  and  $b$ . B: critical slip distance  $D_c$ . There are considerable differences between upsteps (velocity increase) and downsteps (velocity decrease) in the quartz (Qtz), but not the shale (RS). Note values from increases in velocity (upsteps) at even amounts of displacements correspond to the surface roughness measurements and are reported in the text, as described in the Methods.

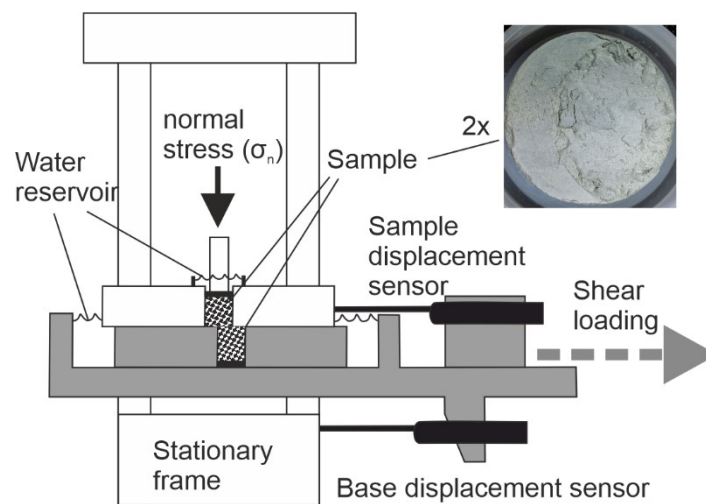


Supplementary Figure 2.4 Comparison of the lengths of critical displacement  $D_c$  and minimum anisotropy  $L_c$  for shale (A) and quartz (B). C:  $D_c$  values are constant with increasing anisotropy. Note values from increases in velocity (upsteps) at even amounts of displacements correspond to the surface roughness measurements and are reported in the text. WLI: white light interferometer, CLSM: confocal laser scanning microscope

## 2.7 Detailed methods

### 2.7.1 Friction experiments

The materials used in the friction experiments are either powdered Rochester shale, which was crushed and sieved to grain size  $<180\ \mu\text{m}$  or a pure quartz powder (Sigrano M4) with 90% of the grains  $<170\ \mu\text{m}$ . The powders were mixed with demineralized water to form a stiff paste, which was pressed into a cylindrical sample cell with diameter 25 mm and height 30 mm. The sample was loaded with an imposed normal stress of 10 MPa and left to consolidate for  $\sim 22$  hours. Experiments were performed at room temperature and saturated with demineralized water.



*Method figure 2.1 Schematic illustration of the direct-shear apparatus (Giesa RS5) used for friction experiments. Shear force is applied by the grey-shaded portion of the apparatus moving to the right, causing the lower shear plate to move relative to the upper shear plate, inducing shear displacement between the upper and lower sample half. The sample assembly is submerged in a demineralized water reservoir open to the atmosphere. Porous metal frits at the top and bottom of the sample to ensure full drainage. Not to scale.*

We conducted the experiments with a Giesa RS5 single direct shear device at the MARUM (Fig M2.1). The used sample cell consists of two steel plates, with through-going cylindrical voids in the middle, where the sample material is sandwiched between porous frits, to allow fluid flow from the water basin to the sample and vice versa. The samples were initially saturated and consolidated until compaction rate diminished, to ensure excess pore water dissipated. During the experimental procedure, the samples are in the dilatational regime, where there are small amounts of dilation upon velocity steps, so no fluid overpressures should form in the sample even if the sample permeability would be low. The top of the water basin is open to the atmosphere, so that we can assume atmospheric pore water pressure in the sample and

effective normal stress is assumed to equal the applied normal stress. A vertical servo-controlled ram is in contact with the top of the sample assembly asserts a constant normal load on the sample.

Upon shear, the lower steel plate is displaced with an electric stepper motor relative to the upper sample half that is kept stationary by the steel loading frame. This causes frictional displacement between the lower and upper steel sample holder plates, dividing the sample in two cylindrical sample halves between which a localized sliding surface develops. Displacement is measured at the base of the loading frame and directly at the sample, making it possible to differentiate between the externally forced displacement and the movement of the sample without effects of machine stiffness. After 10 mm of displacement, the overlap between the upper and lower sample half is reduced to ~50% of the initial contact surface area, after which it decreases rapidly and edge effects of the steel to sample contact become more significant. Therefore, only sample displacements up to 10 mm are used. Although the sample to sample contact diminishes with increasing displacement, the part of the upper half that is not in contact with the lower sample half is supported by the steel, so that the overall area over which the normal load is distributed does not change and normal stress stays constant throughout the experiment. For the experiments where surface roughness was measured, we kept the velocity constant at 10  $\mu\text{m/s}$  until the desired displacement was reached, after which the shear stress was decreased to zero. The excess water was removed before the sample was unloaded and the sample assembly was taken out of the device. The two plates confining the sample are taken apart, to exhume the sliding surface. The top and bottom sample halves were room dried for ~24 hours, to limit the amount of drying during measurement of the sliding surface. We confirmed this drying stage did not have a significant effect on the measured surface parameters, by measuring the same part of the fault surface directly after the experiment and multiple times during the drying process.

We performed a velocity-step test on both materials (the powdered Rochester shale and quartz powder) to determine the frictional parameters. This was done in the same manner as described above, but the velocity was switched between 10 and 1  $\mu\text{m/s}$  every mm of displacement in a way so that at even values of displacements there was an increase from 1 to 10  $\mu\text{m/s}$ . By measuring the shear stress throughout the experiment, we calculate the friction coefficient  $\mu$  as:

$$\mu = \frac{\tau}{\sigma_n} \quad (2.4)$$

assuming negligible cohesion. We modelled the velocity steps according to the empirical rate-and-state friction laws (Dieterich, 1978, 1979, 1981; Ruina, 1983) to obtain the parameters  $a$ ,  $b$  and  $D_c$  at the different displacement values, using:

$$\mu = \mu_0 + a \ln\left(\frac{V}{V_0}\right) + b \ln\left(\frac{V_0\theta}{D_c}\right) \quad (2.5)$$

In which  $V$  is velocity (m/s),  $\mu_0$  and  $V_0$  are reference values,  $a$  and  $b$  are dimensionless constants,  $D_c$  is the critical slip distance in meter and  $\theta$  is the state variable in seconds. We obtain a best-fit to the data using a Matlab-based GUI called RSFit3000 (Skarbek and Savage, 2019). To describe the evolution of  $\theta$  we use the ‘aging’ or ‘Dieterich’ law (Dieterich, 1979):

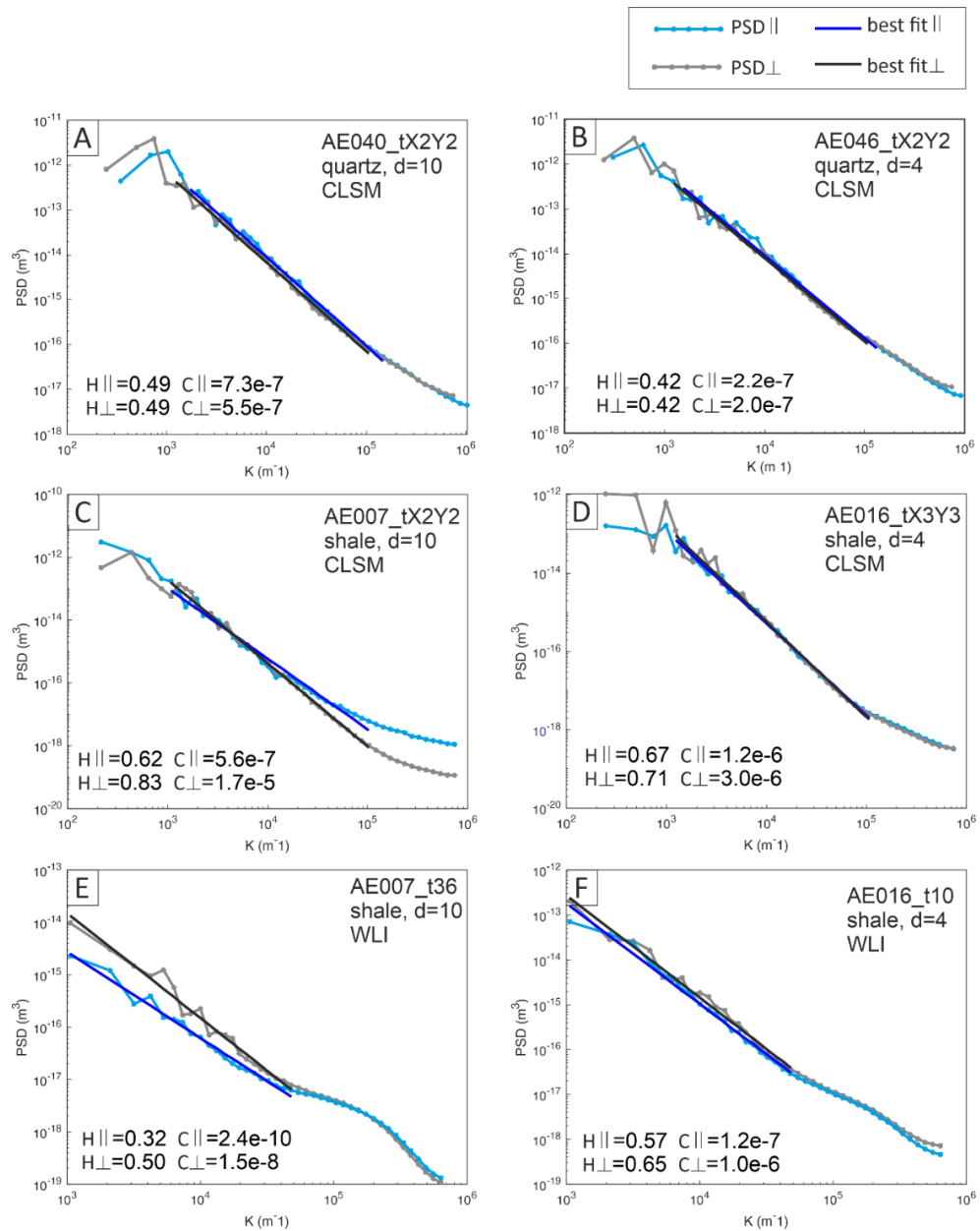
$$\frac{d\theta}{dt} = 1 - \frac{V\theta}{D_c} \quad (2.6)$$

which describes contact evolution as a time-dependent process and allows contact evolution during stationary contacts (Dieterich, 1978). This in contrast to the other often used ‘slip’ or ‘Ruina’ law, which requires slip for contacts to evolve (Ruina, 1983). The ‘aging’ law we use is asymmetric in that there is a difference in friction parameters between upsteps, where the velocity is increased and downsteps, where the velocity is decreased (Supplementary Figure 2.3). For this reason, we only use friction parameters from the upsteps, in which case there is little difference between the ‘aging’ and the ‘slip’ law (Marone, 1998; Bhattacharya et al., 2015). The surface roughness measurements in this study are at even millimeters of displacement, where friction parameters are determined from upsteps. Note that in the shale, there is a large uncertainty in  $D_c$  values, which arises in cases where  $b$  is close to zero in equation (2.5).

A steady-state condition is reached when the friction coefficient and state variable  $\theta$  are constant, or  $\frac{d\theta}{dt}=0$ . When this is the case, equation (2.5) reduces to  $a-b = (\mu_0-\mu)/\Delta\ln V$ . This shows how  $a-b$  expresses the difference in steady-state friction scaled to the change in sliding velocity. Positive  $a-b$  values mean that friction is higher when sliding velocity is increased, indicating velocity-strengthening behavior. Negative  $a-b$  values indicate velocity-weakening behavior, which is a prerequisite for unstable behavior.

## 2.7.2 Surface topography microscopy

We measured all sliding surfaces using a confocal laser scanning microscope (Zeiss LSM 800) with a laser scan head with a wavelength of 405 nm. Using tile stitching, two surface areas of 4.0 by 0.3 mm were measured in a cross-shaped pattern, parallel and perpendicular to the shear direction so that  $>500$  profiles of 4 mm length could be extracted. This cross-shaped pattern maximizes the largest measurable wavelengths, while minimizing measurement time.



Method figure 2.2 Example power spectral density (PSD) curves of measured surface roughness for A: quartz after 10 mm displacement. B: quartz after 4 mm displacement. C: shale after 10 mm of displacement and D: shale after 4 mm of displacement, measured with the confocal laser scanning microscope (CLSM), showing the quartz is isotropic (curves overlap) and the shale becomes anisotropic (curves diverge) at higher displacement. E: shale at 10 mm displacement and F: shale at 4 mm displacement, measured with a white light interferometer (WLI). Indicated are the Hurst exponents  $H$  and constant  $C$  parallel ( $||$ ) and perpendicular ( $\perp$ ) to the sliding direction.

The horizontal spacing between points was 0.624  $\mu\text{m}$  and the vertical spacing between depth-slices was chosen so that the vertical resolution is always  $<0.1 \mu\text{m}$ . Shale powder samples with at least 4 mm displacement were reflective enough to also be measured with a white light interferometer (ContourGT, Bruker), which was done at the Njord Centre of the University of Oslo. We used a green light source and a magnification of 5.0 x 1.0 to measure square areas of 0.95 by 0.95 mm with a horizontal spacing between points of 0.74  $\mu\text{m}$  and nanometer vertical resolution. To analyze the roughness, the measurement was split in up to 1280 profiles parallel and perpendicular to shear. For both measurement techniques, we selected measurement locations along pristine parts of the sliding surface, with clear striations and with minimum gaps or residuals from the other sample half. For the confocal microscope measurements, this selection was done using the camera microscope head before the measurements. For the white light interferometer measurements, this was done by deleting the not intact parts after the measurements. Microscopic analysis of a cross-cut thin section confirms these parts are indeed the sliding surface.

The measured topography profiles were linearly detrended and a 3% cosine taper was applied before the Fourier transform was calculated. The Fourier power spectrum squared normalized to the length of the profile gives the power spectral density PSD, which is a measure for how strong a sinusoidal wavelength is present in the spectral characteristics of a surface (Sagy et al., 2007; Brodsky et al., 2011). We averaged the PSD for all profiles and performed a logarithmic binning to smoothen the curve with minimal data loss. We obtain a best fit on a double logarithmic curve, following:

$$PSD = Ck^{-\beta} \quad (2.7)$$

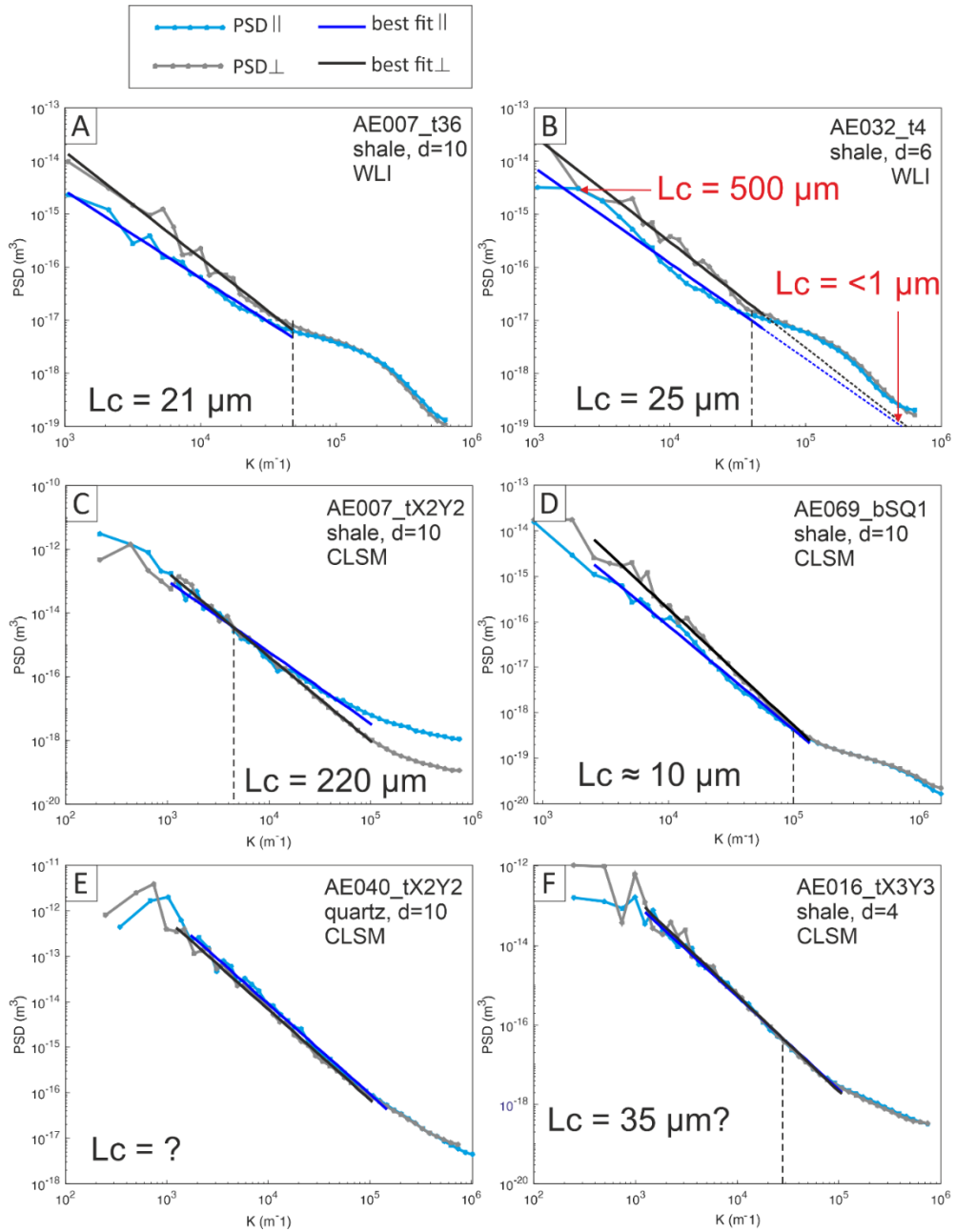
In which  $PSD$  is the power spectral density in  $\text{m}^3$ ,  $k$  is wavenumber ( $\text{m}^{-1}$ ), which is the inverse of wavelength  $\lambda$ ,  $C$  is a constant and  $\beta=2H+1$ , where  $H$  is the Hurst exponent (Brown and Scholz, 1985; Schmittbuhl et al., 1995; Candela et al., 2012). From the Hurst exponents, we calculate the degree of roughness anisotropy ( $A$ ) using:

$$A = \frac{H_{\perp} - H_{\parallel}}{H_{\perp}} \quad (2.8)$$

where  $H_{\perp}$  and  $H_{\parallel}$  are the Hurst exponents perpendicular and parallel to the slip direction (Fig M2). The parameter  $A$  is equal to zero for a truly isotropic surface and increases with increasing anisotropy. Measurements with the WLI, which were only successful for the more reflective shale samples, show trends that are similar as those measured with the CLSM, although  $H$  is up to 0.2 lower and  $C$  is up to two orders of magnitude lower (Supplementary Figure 2.2).

The minimum scale of anisotropy  $L_c$ , is defined as the length scale below which the sample does not show any roughness anisotropy, and is usually of the order of several tens of micrometers (Candela and Brodsky, 2016).  $L_c$  is most reliably determined from the WLI measurements, where the PSD curves parallel and perpendicular to the striations overlap at small length scales (Method figure 2.3A).  $L_c$  was defined by Candela and Brodsky (2016), as the point where the difference between the two PSDs is less than 30%, but in our data due to high noise, curves can overlap at higher wavelengths, making it unreliable to automatically follow this criterion (Method figure 2.3B). Alternatively, the crossover point between the best-fit curves parallel and perpendicular could be used. However, for low displacement fault surfaces, the best-fit PSD curves are close to parallel and extrapolating them would give unrealistically low estimates for  $L_c$  (Method figure 2.3B). In these cases, the data at higher wavelengths was used to obtain values for  $H$  and  $C$  and  $L_c$  was defined as the point where the curves started to overlap. We therefore picked  $L_c$  by hand, but only in those cases where it is relatively clear (~70% of measurements).

In the CLSM, the PSD curves do not necessarily overlap at low wavelengths (Method figure 2.3C), due to the cross-shaped pattern. Measuring square areas would give better results for  $L_c$  (Fig M3D), however, to determine  $H$  and  $C$ , the elongated profiles give better results, because the longer length give a larger wavelength range over which curves can be fitted. To get an estimation for  $L_c$  from the elongated CLSM measurements, we determined the point where the best-fit curves would intersect, which often lies outside of our measurement scales. For the close to isotropic quartz and shale at low displacement, (Method figure 2.3E,F), where the best-fit curves are parallel or almost overlap, the values of  $L_c$  are highly sensitive to small changes in the fitting procedure. All values reported in the text are averages for six measurements with the CLSM and 8-35 measurements with the WLI, combined for the top and bottom half of the sample.



Method figure 2.3 measuring the minimum scale of anisotropy  $L_c$ . A: white light interferometry (WLI) curves have a clear divergence point. B: PSD curves can overlap due to noise at high wavelengths, this would lead to a too high estimate of  $L_c$  and using the intersection of the best-fit curves would lead to a lower  $L_c$  than the actual wavelength where the PSD curves start to overlap. C: PSD curves measured with the confocal laser scanning microscope (CLSM) do not overlap, the intersection of best-fit curves is used as an indicator for  $L_c$ . D: measuring square areas with the CLSM would give diverging PSD curves similar to the WLI measurements. For the isotropic quartz (E) and shale at low displacements (F), estimating  $L_c$  is sensitive to very small changes in PSD curves.

### 3 How fault-normal and shear-parallel stiffness influence frictional sliding behavior

*Agathe M. Eijsink and Matt J. Ikari*

Key points:

- Reducing shear stiffness causes a transition from stable through slow slip to stick-slip
- Reduced normal stiffness increases the friction coefficient and increases  $a$ - $b$
- Reduced normal stiffness alone can cause stick-slip instabilities, but no slow slip
- Systematically reducing both shows irregular events, where the largest events occur at low shear stiffness and high normal stiffness

#### 3.1 Abstract

The potential of faults to show earthquake-like stick-slip instabilities, depends only partly on the intrinsic frictional properties of the fault zone, but also on the elasticity of the surrounding material. A velocity-weakening fault will have a transition in slip mode from stable sliding through slow slip events to large, fast earthquakes with decreasing stiffness parallel to the shearing direction. Due to the roughness all faults planes have, slip in the shear direction must be accompanied by fault-normal movement, working against stiffness in the fault normal direction. In this paper, we systematically vary the stiffness surrounding the fault in both the shear-parallel and fault-normal directions, to investigate under which conditions slip instabilities can occur. We confirm the transition expected due to reduced shear stiffness occurs and that the occurrence of different types of slip events can be explained by the proposed critical stiffness criterion. A reduced normal stiffness also causes slip instabilities, despite a higher friction coefficient and less pronounced velocity-weakening. We propose these slip instabilities are caused by a different mechanism, known as wrinkle-like slip pulses, because of a stiffness asymmetry that is introduced by lower the fault normal stiffness.

## 3.2 Introduction

Faults, although macroscopically planar, exhibit roughness on all scales (Chapter 2, Power et al., 1987; Candela et al., 2012). This means that when faults slip, not only displacement parallel to the fault occurs, but motion perpendicular to the fault plane is required. Quartz gouges dilate (expand) during shear loading and compact during unloading (Marone et al., 1990), and dilate when sliding velocity is increased (Samuelson et al., 2009). During stick-slip motion, thought to be the laboratory equivalent of earthquakes, faults dilate during the ‘sticking’ phase when shear stress builds up and compact during the slip event, when the stress drops (Scuderi et al., 2016a). However, whether a fault slips in a stable manner, or in stick-slip cycles, depends not only on the fault itself, but also on the stiffness or shear modulus of the surrounding material (Dieterich, 1979; Rice and Ruina, 1983; Scholz, 1998). Here, we investigate the influence of the stiffness of the surrounding material on frictional behavior and occurrence of unstable slip.

To exhibit stick-slip behavior, a fault must exhibit velocity-weakening behavior, meaning friction decreases with increasing velocity, but a second condition is that the fault must have a higher stiffness than the surrounding material, i.e. the fault must unload stress faster than the surroundings (Scholz, 1998). This can be described with a spring-slider model, where, if the spring has a low enough stiffness, shear stress applied to the fault is first stored in the spring, until the resistance of the slider (fault) is overcome and the slider jumps forward, releasing the elastic energy stored in the spring (Gu et al., 1984) (Fig. 3.1A). The stiffness governing this, is the stiffness in the direction parallel to the sliding direction, or in the direction of the shear stress. The role of this stiffness in the shear direction, has been shown to be crucial for the transition between stable sliding and stick-slip behavior in materials under conditionally unstable conditions (Scholz, 1998), both in models (Ruina, 1983; Gu et al., 1984) and laboratory experiments (Leeman et al., 2016; Scuderi et al., 2016b). Dilation on the other hand, works against the normal stress, which may or may not have the same stiffness (Fig 3.1B), but this stiffness is not considered in most simple spring-slider models.

In nature, there are various processes that may affect the host rock stiffness. The most important of these include lithology and consolidation state, where the stiffness of individual minerals as well as how well cemented they are control the host rock stiffness. A stiffness contrast occur the fault may occur when a fault juxtaposes different lithologies, or lithologies with different consolidation states, which is common when the fault movement has a component of

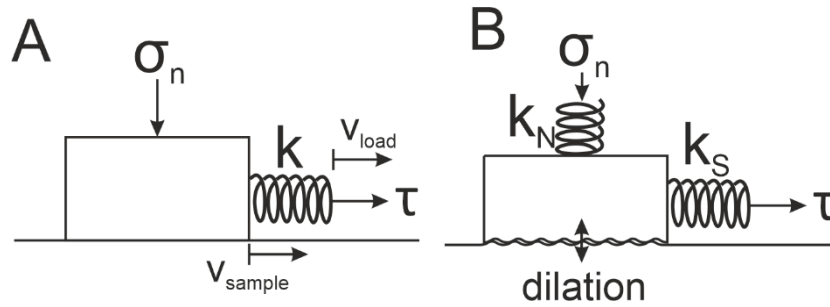


Figure 3.1: A: a simple spring-slider system, commonly used to represent a sliding fault. B: How a spring-slider system may be viewed if vertical stiffness plays a role

dip-slip movement. A contrast in elastic properties has for example been shown for the San Andreas fault and the North-Anatolian fault, and can be quantified by contrasts in seismic velocities or the occurrence of fault zone head waves (Le Pichon et al., 2005; Zhao et al., 2010; Share and Ben-zion, 2016). Another process influence the host rock stiffness is that faulting often involves fracturing, brecciation or pulverization of the host rock, decreasing its stiffness (Kim et al., 2004; Faulkner et al., 2006; Griffith et al., 2009). The damage zone that forms surrounding the main fault is also commonly asymmetric, contributing to the effect of stiffness asymmetry.

In this study, we use laboratory experiments to investigate the effect of varying the stiffness in the direction of the normal stress ( $k_N$ ), in addition to varying the stiffness in the direction of the shear stress ( $k_S$ ). Whereas decreasing  $k_S$  is known to cause a transition in sliding behavior from stable sliding through slow slip to rapid stick-slip, the effect of  $k_N$  has received little attention so far. Our study focusses on the effect normal stiffness ( $k_N$ ) has on frictional behavior and sliding stability. Combining this with the known effect shear stiffness has, gives an integrated approach how host rock conditions can influence slip stability.

### 3.3 Methods

#### 3.3.1 Experimental procedure

For the experiments, we used Sigrano M4 pure quartz powder ( $>99\%SiO_2$ ), which has a median grain size of  $50\ \mu m$ . The quartz powder was mixed with deionized water and pressed into the sample cell, which consists of two steel plates with a cylindrical void in the middle, where the sample material is compressed between two porous sintered-steel frits. The porous plates ensure that the sample material is in contact with the deionized water that is added to the top of the sample and a water basin surrounding the two plates. The water basins are open to atmosphere, so that the pore pressure in the sample is at atmospheric pressure and the effective normal stress is equal to the applied normal stress of 20 MPa. Normal sample height was 9.8 mm below the shear interface and 5.5 mm above the shear interface, which leads to a poisson effect once the normal stress is applied, transferring part of the applied normal stress to the sides of the steel sample container (Fagereng and Ikari, 2020a). We corrected for this by measuring shear stress on a sample with a height of 2.0 mm above the shear interface, where we assume this effect is negligible, but as a downside these samples are too small to be recovered after the experiment for possible additional analyses. By comparing the friction coefficient measured on the smaller sample with that measured during standard experiments, we could calculate that the shear interface experiences 17.1 MPa normal stress, and the measured friction coefficient and a-b values modelled from the original data with higher samples were corrected accordingly.

After application of the normal stress, the sample is left to compact 12-16 hours, after which shearing is initiated. The experimental sequence is initiated with a run-in phase of 5 mm displacement at a driving velocity of  $10\ \mu m/s$ , after which 2 series of velocity-steps are applied, with driving velocities of 0.1, 1 and  $10\ \mu m/s$ , for a displacement of 1 mm, which is then repeated (Fig. 3.2A). A stepper motor drives the lower plate forward at the set driving velocity, while the upper plate is held stationary, inducing shear deformation at the level of the interface of the two steel plates. Our set-up enforces localization in a very thin zone in the sample material, and although the quartz powder we use resembles fault gouge material, this is different to the deformation of a gouge layer of defined thickness commonly used in laboratory (e.g. Marone et al., 1990; Leeman et al., 2016), where volumetric deformation can take place throughout the whole layer.

### 3.3.2 Data analysis

During the experiments, we measure the shear stress ( $\tau$ ) that is needed for displacement to occur at the set driving velocity, which is normalized to the applied effective normal stress ( $\sigma'_n$ ) to give the friction coefficient ( $\mu$ ):

$$\mu = \frac{\tau}{\sigma'_n} \quad (3.1)$$

We report the friction coefficient at the peak ( $\mu_{peak}$ ) that occurs in all experiments after 2.5-3 mm of sliding (Fig. 3.2A), which marks the point in time when the sliding velocity in the sample (sample velocity) matches the set driving velocity. After an initial decrease, friction generally increases with increasing displacement, so that the steady-state friction coefficient ( $\mu_{steady-state}$ ), which is the average friction coefficient over the last 25  $\mu\text{m}$  before the first velocity step starts, can be higher than the peak friction value (Fig. 3.2A).

Unstable sliding is possible when friction decreases with increasing sliding velocity, called velocity-weakening behavior. When the friction increases with increasing sliding velocity (velocity-strengthening), it is energetically unfavorable for a fault to accelerate. The velocity-dependence of faults is commonly tested with velocity-step experiments, and analyzed using the rate-and-state friction (RSF) framework (Dieterich, 1978), which describes that upon a velocity change, friction  $\mu$  will evolve following (Fig. 3.2B):

$$\mu = \mu_0 + a \ln\left(\frac{V}{V_0}\right) + b_{1,2} \ln\left(\frac{V_0 \theta_{1,2}}{D_{c1,2}}\right) \quad (3.9)$$

In which  $\mu_0$  is the friction coefficient at a reference velocity  $V_0$  (m/s),  $a$  and  $b$  are dimensionless parameters that scale the direct effect and the subsequent evolution effect, and  $\theta_{1,2}$  (seconds) are the state parameters that develop towards a new steady-state value over a distance  $D_c$  (m). There are multiple evolution laws how  $\theta_{1,2}$  develops with time  $t$ , we use the commonly used ‘aging’ law:

$$\frac{d\theta_i}{dt} = 1 - \frac{V\theta_i}{D_{ci}}, i = 1, 2 \quad (10.3)$$

At steady state, where  $\theta_{1,2}$  are constant, equation (1) reduces to:

$$\frac{\Delta\mu_{ss}}{\Delta \ln(V)} = a - b \quad (3.11)$$

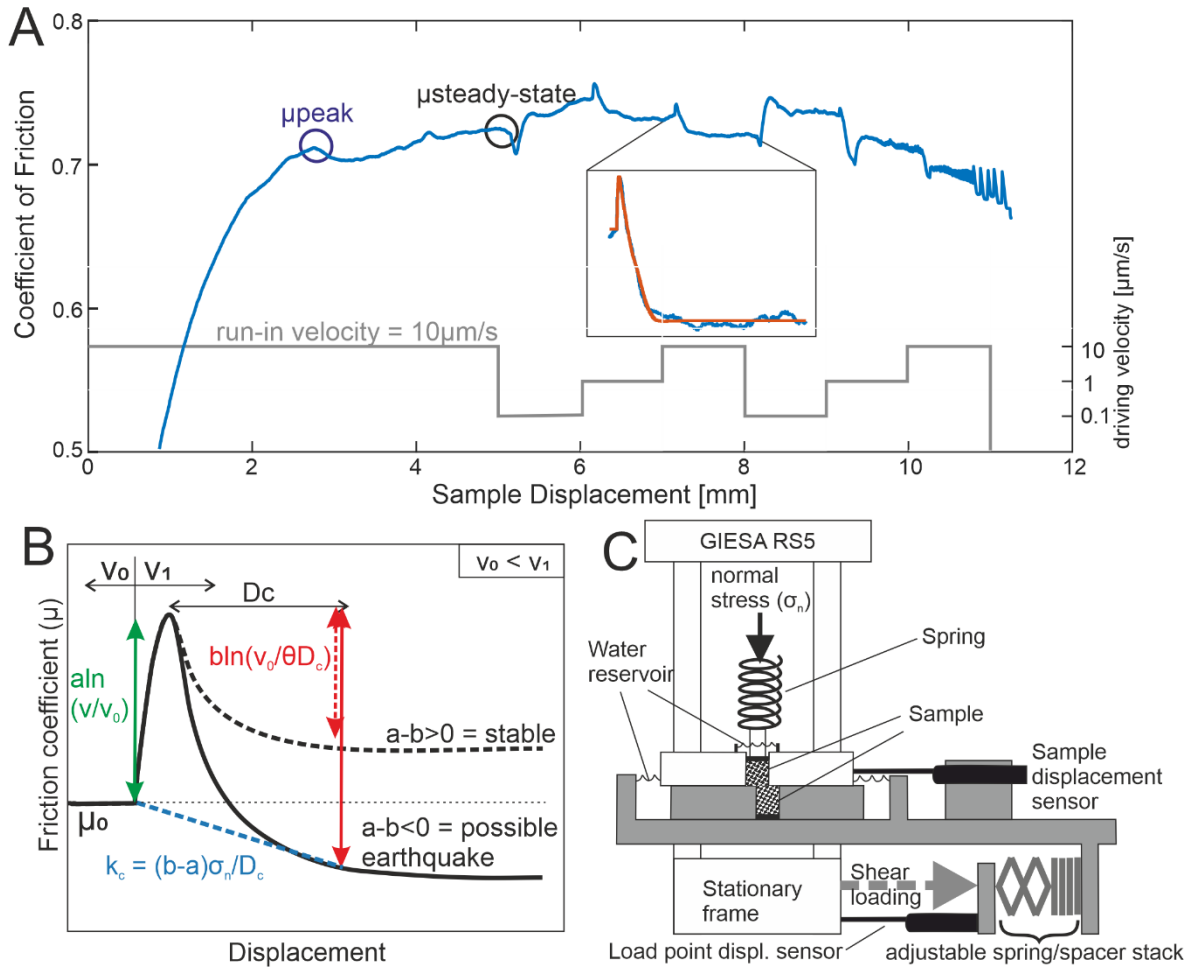


Figure 3.2: A: data example (AE127) using a 1.2 MPa/mm vertical spring and a horizontal stiffness of 3.2 MPa/mm, including the velocity stepping sequence (grey). B: Evolution of friction after a velocity step, including the rate-and-state friction model. C: Experimental set-up, showing the load point displacement sensor measures displacement before the adjustable stack of spacers and springs that is used to vary horizontal stiffness, and a sample displacement sensor measures displacement directly on the sample; vertical stiffness is adjusted by the placement of a spring below the vertical forcing ram.

Where  $\Delta\mu_{ss}$  is the difference in steady-state friction coefficient between the two sliding velocities that give  $\Delta \ln(V)$ . This shows that  $a-b$  is the single parameter needed to distinguish between velocity-strengthening (positive  $a-b$ ) and velocity-weakening (negative  $a-b$ ) behavior.

Negative  $a-b$  values will not automatically lead to unstable sliding behavior, but indicate that possible instabilities, once initiated, can grow. Whether instabilities will occur, depends on whether the fault unloads shear stress faster than the surrounding material. Instabilities will only occur when the stiffness in the shear stress direction  $k_S$  is smaller than a critical value  $k_c$ :

$$k_S < k_c = \frac{(b-a) \sigma'_n}{D_c} \quad (3.12)$$

We use the first sequence of velocity increases (5-8 mm displacement) to analyze the velocity-dependent behavior of the material, which in most experiments is difficult in the second sequence (8-11 mm displacement) by the occurrence of stick-slip behavior and large stress drops directly after a velocity step (Fig. 3.3). We use the RSFit3000 Matlab script (Skarbek and Savage, 2019) to find the optimal fit for the rate-and-state parameters.

### 3.3.3 Stiffness adjustments

The stiffness of the machine in the direction of shear displacement ( $k_S$ ) is tested by loading a steel blank in the place of the sample material. The displacement measured by the sensor at the base of the machine (Fig. 3.2C) is corrected for the small amount of displacement that takes place in the steel blank by subtracting the sample displacement from the load-point displacement, so that the machine stiffness is calculated from the shear stress over the machine displacement only. Without any alterations,  $k_S$  was measured to be 14 MPa/mm, whereas initial measurements show  $k_c$  is  $\sim 3$  MPa/mm, therefore slip events are only expected when  $k_S$  is reduced. This was achieved by adding an extension that provides space for a stack of disc springs and steel spacers (Fig. 3.2C). By increasing the amount of disc springs relative to solid steel plates,  $k_S$  can be decreased incrementally. We used 1, 4, 8 or 12 disc springs, to achieve values for  $k_S$  of 6.6, 3.2, 2.1 and 1.5 MPa/mm, to capture the transition where  $k_S$  is close to  $k_c$ .

The stiffness in the direction of the normal stress  $k_N$  was varied by the insertion of steel springs below the vertical ram that applies the normal force. The steel springs we used have measured stiffness values of 1.2, 2.0 and 4.1 MPa/mm. The apparatus stiffness normal to the fault as measured by loading a steel spacer instead of a sample is 470 MPa/mm. However, in contrast to the shear direction, where the fault surface is only surrounded by the machine, in the normal direction, the thin fault plane is also surrounded by a few mm's of sample material. The sample material is more elastic than the steel parts of the machine, and the stiffness as experienced by the fault plane is therefore lower than measured on top of the sample. To measure the fault-normal stiffness on the fault surface, we measured the stiffness with a sample consolidated in a similar fashion as the experimental samples. We measure an average normal stiffness of  $\sim 223$  MPa/mm, which changes from 204 MPa/mm before shear to 242 MPa/mm after shear, a change that is relatively small compared to the stiffness decrease by inserting the steel springs. The stiffness of the springs used to lower the fault-normal stiffness is so low compared to the stiffness of the sample, that we expect the sample has no significant effect when the springs are used. A reduced normal stiffness causes non-systematic changes in shear stiffness of  $\pm 1\%$ , from which we conclude the normal and shear stiffness do not influence each other.

### 3.3.4 Slip events

Stick-slip behavior is most common during the last velocity-step, which is why these are analyzed in more detail. Slip event statistics referred to throughout this paper are those that occur during that last millimeter of sliding, at a driving velocity of  $10 \mu\text{m/s}$ . We consider a slip event as such when a drop in shear stress coincides with an increase in velocity of at least 3x compared to the pre-event sample velocity. We define the start of the loading phase as the point where shear stress starts to increase, the start of the slip event as the maximum shear stress reached and the end of the slip event at the lowest shear stress after the event. With that we measure the load duration as the time from the start of the loading to the start of the slip and the slip duration as the time during the stress drop. The slip is the displacement during the slip duration and the stress drop as the peak shear stress to final shear stress. The unloading stiffness of the event is measured by fitting a best-fit curve through the unloading part of a stress-displacement curve. The initial sliding velocity is the minimum sample sliding velocity measured during the loading phase and the peak slip velocity is the maximum sample sliding velocity during the stress drop.

The vertical displacement could not be measured directly on the sample. Instead, we measure compaction during the slip event itself, which is so rapid that it is not immediately corrected for by the servo-controlled vertical load cell and leaves a small stress drop in the normal stress. Scuderi et al. (2016a) measure compaction and dilation by pore fluid volume in gouge and show that when the data is corrected for ongoing thinning of the gouge layer, the compaction during the slip event is comparable to the dilation during the interseismic period. Since in our set-up deformation takes place at the interface of the upper and lower steel plates holding the sample, we do not have to correct for the thinning of a gouge layer, and we can assume that the compaction during the slip event is similar to the dilation in between slip events. The measured normal stress drops are rarely larger than 40 kPa (with two exceptions of 350 kPa), or 0.2% of the applied normal stress and are therefore not likely to directly influence the sliding behavior. With the known vertical stiffness values, we can calculate the vertical compaction from the normal stress drop during the slip event. Since normal stress drops can only be measured when they exceed the noise in normal stress signal of  $\sim 3$  kPa, the minimum compaction needed to be measurable must be about  $2 \mu\text{m}$  when  $k_N=1.2 \text{ MPa/mm}$ , but only  $0.01 \mu\text{m}$  when  $k_N=223 \text{ MPa/mm}$ . For about half of the slip events there was a measurable drop in normal stress and compaction could be quantified.

## 3.4 Results

### 3.4.1 Frictional behavior

Figure 3 gives an overview of the changes in frictional behavior with decreasing normal stiffness (Figure 3.3A) and decreasing shear stiffness (Figure 3.3B). With decreasing normal stiffness we observe that the steady state friction coefficient ( $\mu_{steady-state}$ ) increases from 0.60 to 0.72, although the experiment with  $k_N=2.0$  MPa/mm has a higher  $\mu_{steady-state}$  (0.72) than the experiment with the lowest  $k_N=1.2$  MPa/mm (0.70). Reducing the shear stiffness does not influence the friction coefficient, as shown in the inset in the bottom left of Figure 3.3B. The main plot, where curves are offset vertically and  $\mu_{steady-state}$  is indicated, shows  $\mu_{steady-state}$  is 0.60-0.61, with the exception of the experiment where  $k_S=2.1$  MPa/mm, which has  $\mu_{steady-state}=0.64$ . Figure 4A shows the peak and the steady-state friction coefficients, which both decrease with increasing  $k_N$ . Shear stiffness  $k_S$  does not influence friction coefficient (Figure 3.4B).

As is visible from the plots with decreasing fault normal stiffness in figure 3A as well, is that  $(a-b)$  is higher when fault normal stiffness is lower. This is quantified and shown in Figure 3.4C, that shows  $a-b$  increases from -0.005 to -0.01 at high normal stiffness, to -0.002 to -0.004 at low normal stiffness. This increasing  $a-b$  with decreasing normal stiffness is clearer for the low velocities than for the high velocities. For decreasing shear stiffness  $k_S$ , there is no trend in  $a-b$  (Figure 3.4D). The clear increase in  $a-b$  with decreasing  $k_N$  is not clearly linked to either decreasing  $a$  or increasing  $b$  (Fig. 4E) with normal stiffness. For the lowest velocity ( $v=0.1\mu\text{m/s}$ ),  $a$  decreases from  $\sim 0.011$  to  $\sim 0.006$  ( $v=0.1\mu\text{m/s}$ ), but for the higher velocities, this effect is small:  $a$  decreases from  $\sim 0.006$  to  $\sim 0.003$  for  $v=1\mu\text{m/s}$  and from  $\sim 0.005$  to  $\sim 0.003$  at  $v=10\mu\text{m/s}$  with increasing normal stiffness. Friction parameter  $b$  seems relatively constant with normal stiffness, although for  $1\mu\text{m/s}$   $b$  might increase with increasing stiffness.

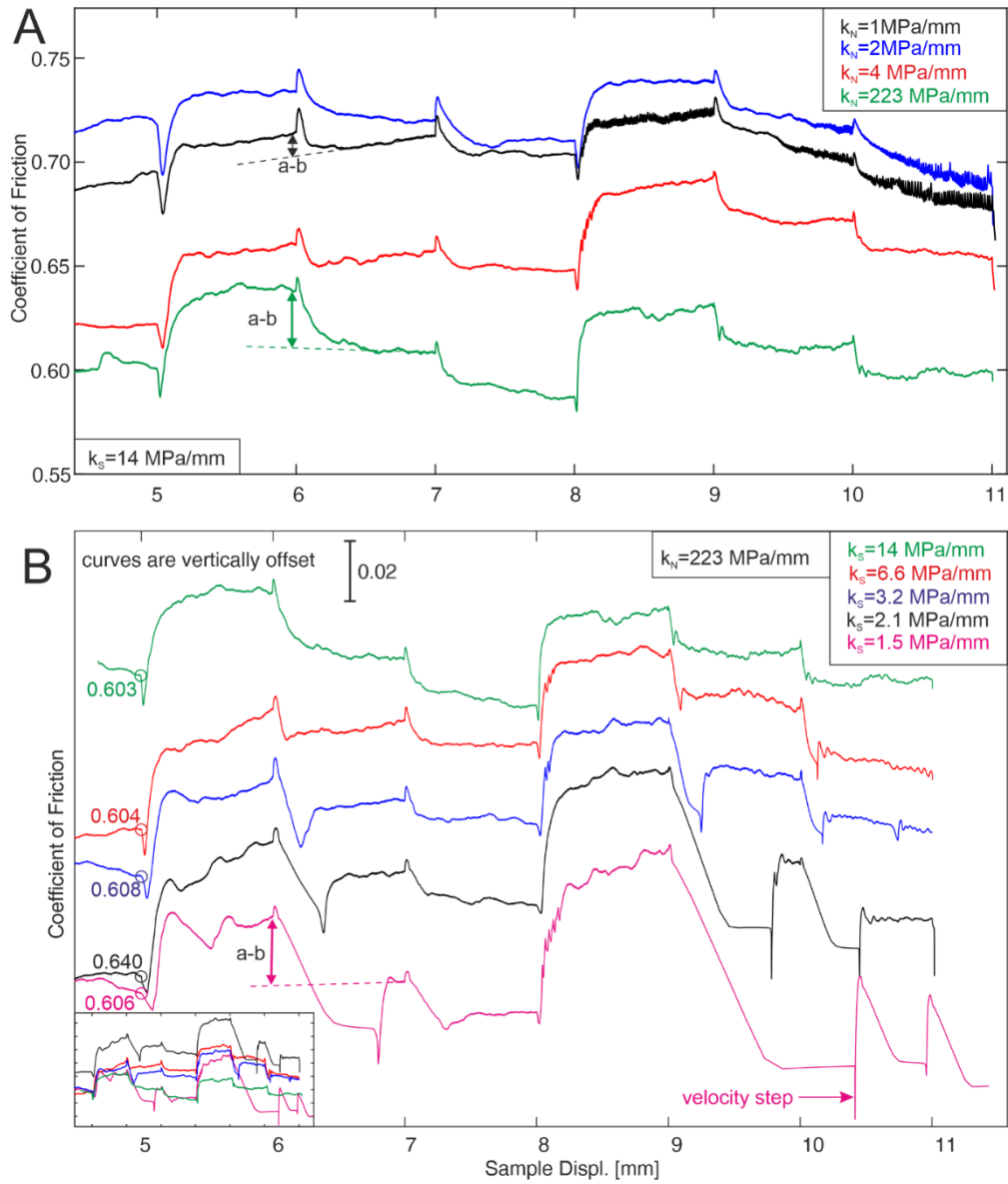


Figure 3.3: friction with displacement for A: varying normal stiffness  $k_N$ , at constant shear stiffness  $k_S$  and B: varying shear stiffness  $k_S$ , at constant the normal stiffness  $k_N$ . In B, curves are offset for clarity, since friction coefficients at 5 mm are relatively constant, as indicated. Inset on left bottom shows not offset curves. In B, for the pink curve with  $kh = 1.5 \mu\text{m/s}$  the velocity step at 10 mm displacement was initiated directly after the first large slip event at a displacement of  $\sim 10.4$  mm. Green curves in A and B are the same experiment, with machine  $k_N$  and machine  $k_S$ .

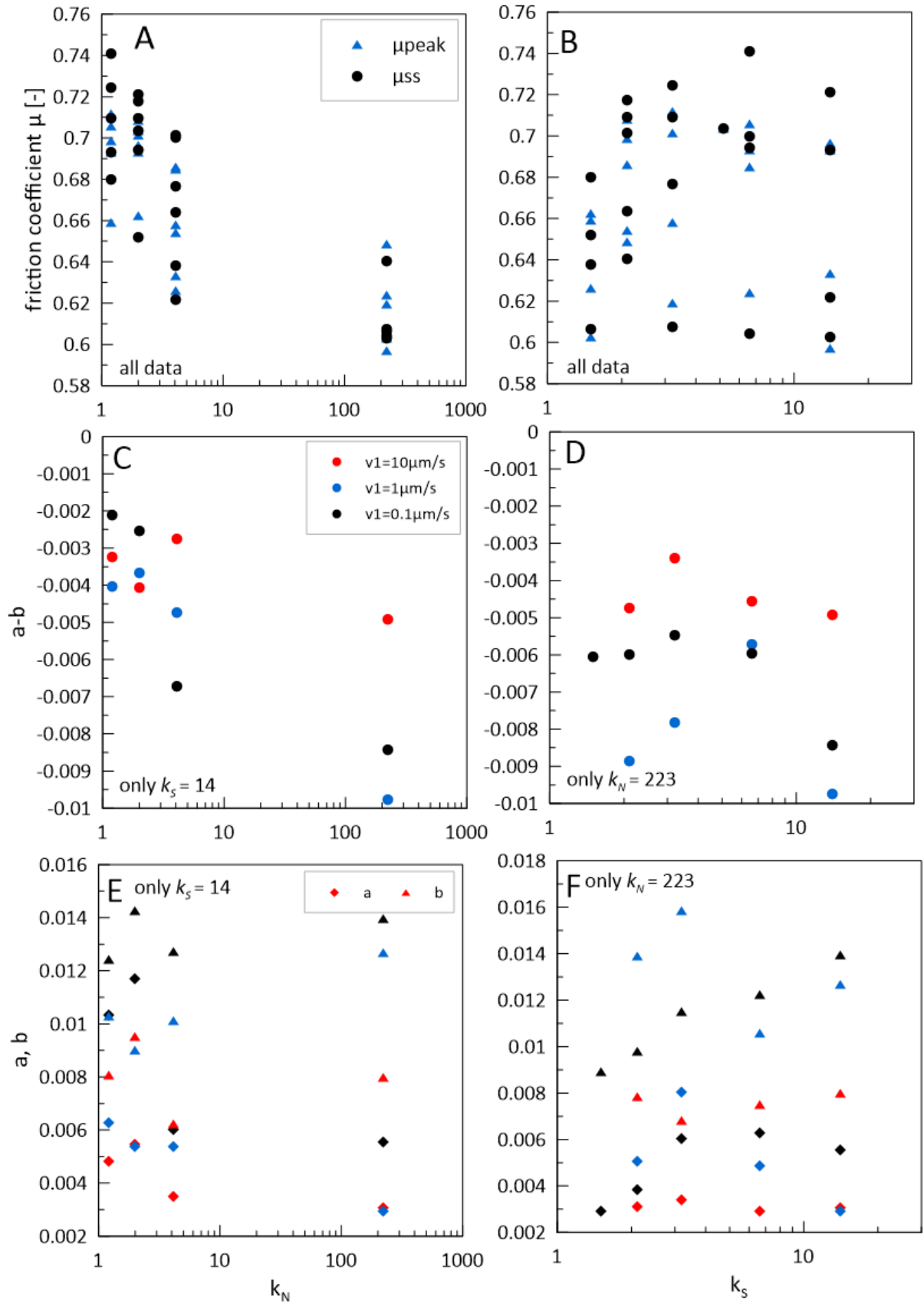


Figure 3.4 A: apparent friction coefficient and B: frictional stability parameter  $a-b$  decrease with  $kv/kh$ . Note peak friction is the peak that occurs after 2-3 mm displacement, friction coefficient may then increase, so that steady-state friction at 5 mm displacement is higher than  $\mu_{peak}$ .

### 3.4.2 Slip event occurrence

Most experiments show slip instabilities, at least during the last mm of sliding at  $10 \mu\text{m/s}$ , which is shown in figure 5. Out of all possible combinations of shear stiffness  $k_S$  and normal stiffness  $k_N$ , the only two experiments that show perfectly stable sliding are when  $k_S$  is 14 MPa/mm and  $k_N$  is 4.1 or 223 MPa/mm (top left in Fig. 3.5). Other relatively stable experiments are when normal stiffness is 4.1 MPa/mm and shear stiffness is 6.6 MPa/mm where only very small and slow slip events occur. Shear stress irregularities with low peak slip velocities occur when  $k_N$  is 4.1 MPa/mm and shear stiffness is 2.1 MPa/mm. Also the experiment with  $k_N$  of 2 MPa/mm and  $k_S$  is 1.5 MPa/mm is remarkably stable and only starts to show slip instabilities after more than a mm of sliding at  $10 \mu\text{m/s}$ .

At a constant high normal stiffness of 223 MPa/mm (left column in Fig. 3.5), reducing the shear stiffness causes a transition from stable sliding at  $k_S=14$  MPa/mm to relatively small and symmetrical slip events at shear stiffness values of 6.6 to 3.2 MPa/mm (Fig. 3.6A). The ratio of load duration to unload duration, which quantifies the symmetry of events, are 1.2 and 1.1 on

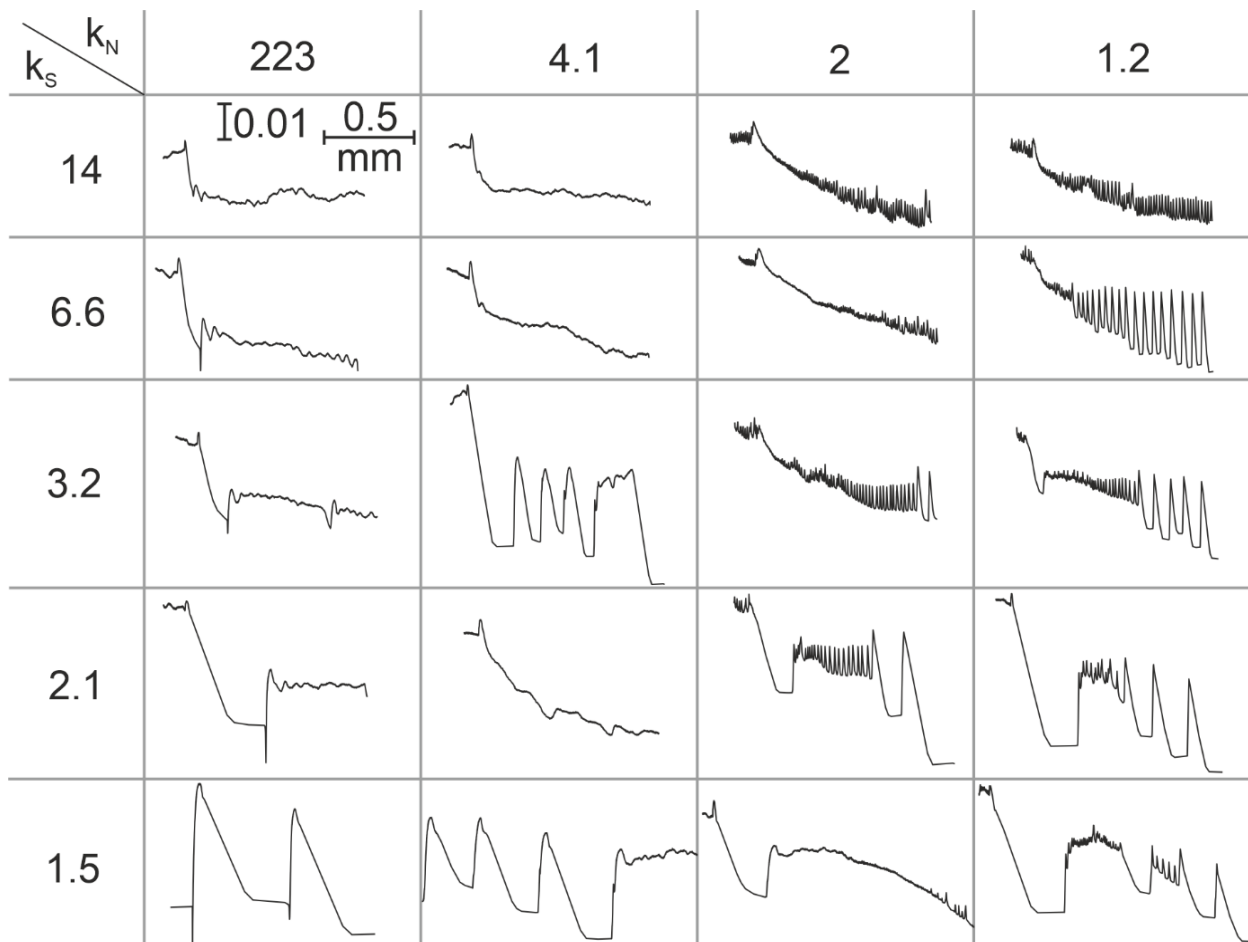


Figure 3.5: slip stability during the last mm of sliding, stiffness values are in MPa/mm

average for  $k_S$  of 6.6 and 3.2 MPa/mm, meaning the loading and unloading take almost equally long and these events are relatively symmetrical. When shear stiffness is reduced to 2.1 MPa/mm, sliding is surprisingly stable (Fig. 3.5). When shear stiffness is then reduced further to  $k_S=1.5$  MPa/mm, very large ( $>800$  kPa) stress drops occur, which are asymmetrical and have load/unload ratios of 0.02 (Fig. 3.6B). Similar large events occur when  $k_N=4.1$  and  $k_S=1.5$  MPa/mm, but there the large events disappear after 3 events. Also when  $k_N=4.1$  and  $k_S=3.2$  MPa/mm these large events occur, but disappear after three events, but then another large event happens after continued sliding.

On the other hand, reducing the normal stiffness  $k_N$  at a constant high shear stiffness of 14 MPa/mm (top row in figure 3.5), shows small, short period stick-slip behavior when  $k_N$  is reduced to 2.0 or 1.2 MPa/mm (Fig. 3.6C). At  $k_N=2.0$  MPa/mm, the first 10 slip events have load/unload ratios of  $\sim 1.1$  and are therefore relatively symmetrical, after which the load/unload ratio decreases to 0.33. At  $k_N=1.2$  MPa/mm, the small events that occur at low  $k_N$  start growing larger with displacement. Interesting to note is that these event only partly gradually grow larger, as is

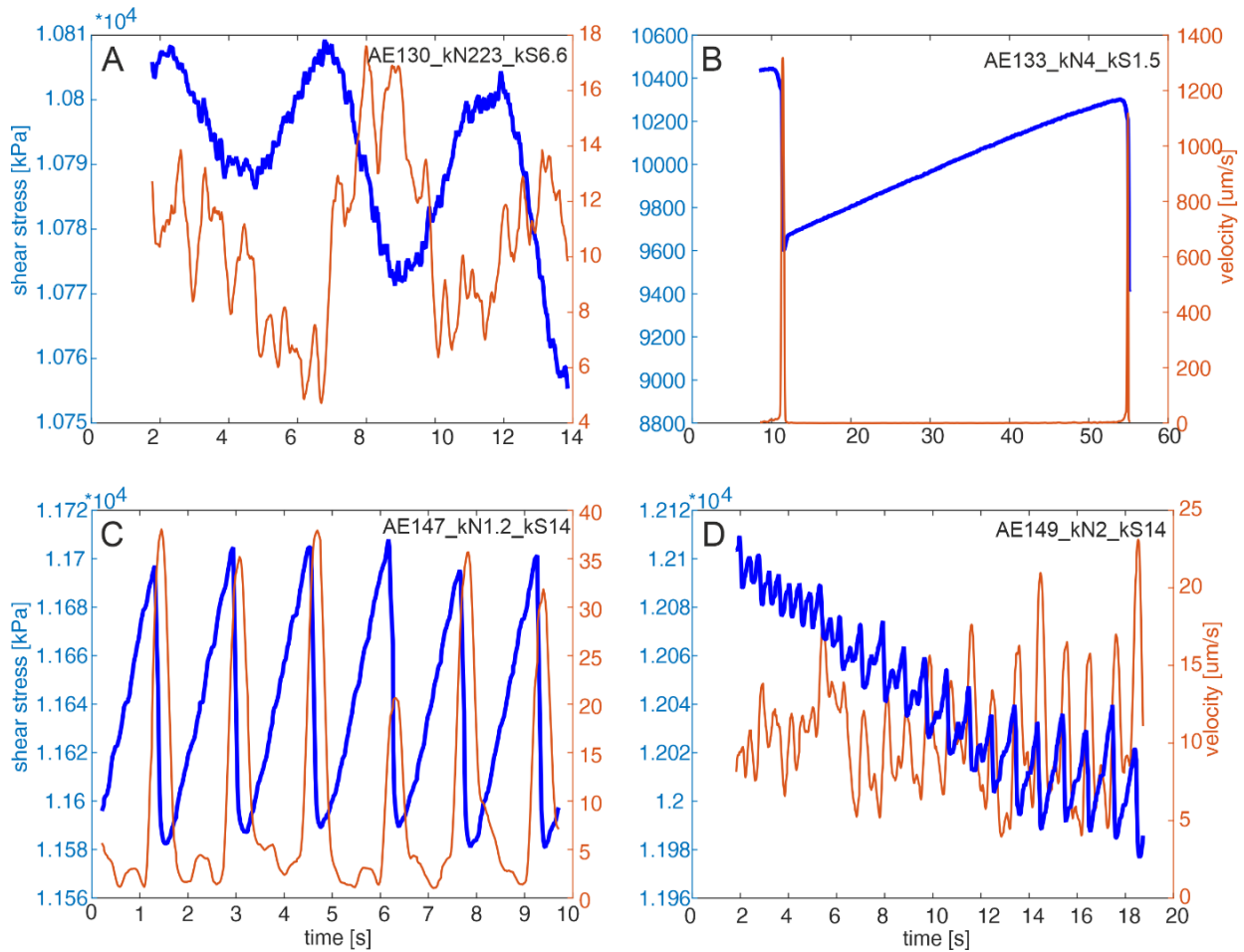


Figure 3.6: Examples of slip events, A: oscillatory events, B: very large stress drop events, C: small rapid stick-slip, D: events grow by period doubling

common when slip events start (e.g. Leeman et al., 2016) and partly grow larger by period-doubling (e.g. Abe and Kato, 2013) when two small events combine into one event double the size (Fig. 3.6D).

### 3.4.3 Slip event statistics

To look into the effect shear stiffness alone has on slip event velocity and stress drop, we focus on the events that occur at the lowest normal stiffness  $k_N=1.2$  MPa/mm (right column in Fig.3.5), because at this normal stiffness, slip events occur at all shear stiffness values used. Figure 3.7A shows there is no clear dependence of stress drop on shear stiffness. The grouped data points show in a different way the observation shown in figure 3.6D, that events do not gradually grow larger, but there is a step from small stress drop events to larger stress drop events with continued sliding. Maximum values for stress drop are  $\sim 500$  kPa for all shear stiffness values below 14 MPa/mm. The maximum slip velocities (Fig. 3.7B) show a similar grouping in data points, where especially for slip events that occur at low  $k_S$  there is a distinction between relatively slow events ( $v_{peak} \sim 40$   $\mu\text{m/s}$ ) and events with increasing peak slip velocities for decreasing shear stiffness, up to  $\sim 1$  mm/s. The compaction measured during the slip event ranges between 2 and 15  $\mu\text{m}$  and does not show a clear dependency on shear stiffness, although data spread is larger at low  $k_S$  (Fig. 3.7C).

To analyze the effect of normal stiffness on the slip events, we focus on the events that occur at the lowest shear stiffness  $k_S=1.5$ MPa/mm (bottom row in Fig. 3.5), since at this shear stiffness slip events occur at all values of normal stiffness. Figure 3.7D shows that stress drop gradually increases with increasing normal stiffness for some events, up to 886 kPa for the largest event at  $k_N=223$  MPa/mm. Also here we observe smaller slip events, with stress drops  $\sim 40$  kPa. The peak slip velocity increases with increasing normal stiffness for these large events (Fig. 3.7E), up to 2.4 mm/s for the largest stress drop event at  $k_N=223$  MPa/mm. The smaller events with stress drops  $\sim 40$  kPa have lower peak slip velocities of  $\sim 30$   $\mu\text{m/s}$ . The compaction data for varying normal stiffness do not show a very clear relationship (Fig. 3.7F), but the largest compaction (13  $\mu\text{m}$ ) occurs at the lowest normal stiffness of 1.2 MPa/mm and only very little compaction (1.6  $\mu\text{m}$ ) occurs for the large events at  $k_N=223$  MPa/mm.

When we include all data (Fig. 3.7G&H), similar trends can be observed as for the separate parameters. The opposite trends where stress drop and peak slip velocity decrease with increasing  $k_S$  (Fig. 3.7A&B) and increase with increasing  $k_N$  (Fig. 3.7D&E) amplify each other. The ratio  $k_N/k_S$  shows that larger stress drops occur at higher  $k_N/k_S$  ratios, although small events

occur that do not follow this trend (Fig. 3.7G). The peak slip velocity shows a similar picture, higher peak slip velocities occur for increasing  $k_N/k_S$  ratio, but slower slip events occur as well (Fig. 3.7H), which are the events with the smaller stress drops. Event stress drop and peak slip velocity therefore seem controlled by the  $k_N/k_S$  ratio and not specific values for stiffness. The compaction data, which does not vary with shear stiffness and may decrease with increasing normal stress, does not show any trends when plotted over  $k_N/k_S$  ratio (Fig. 3.7I).

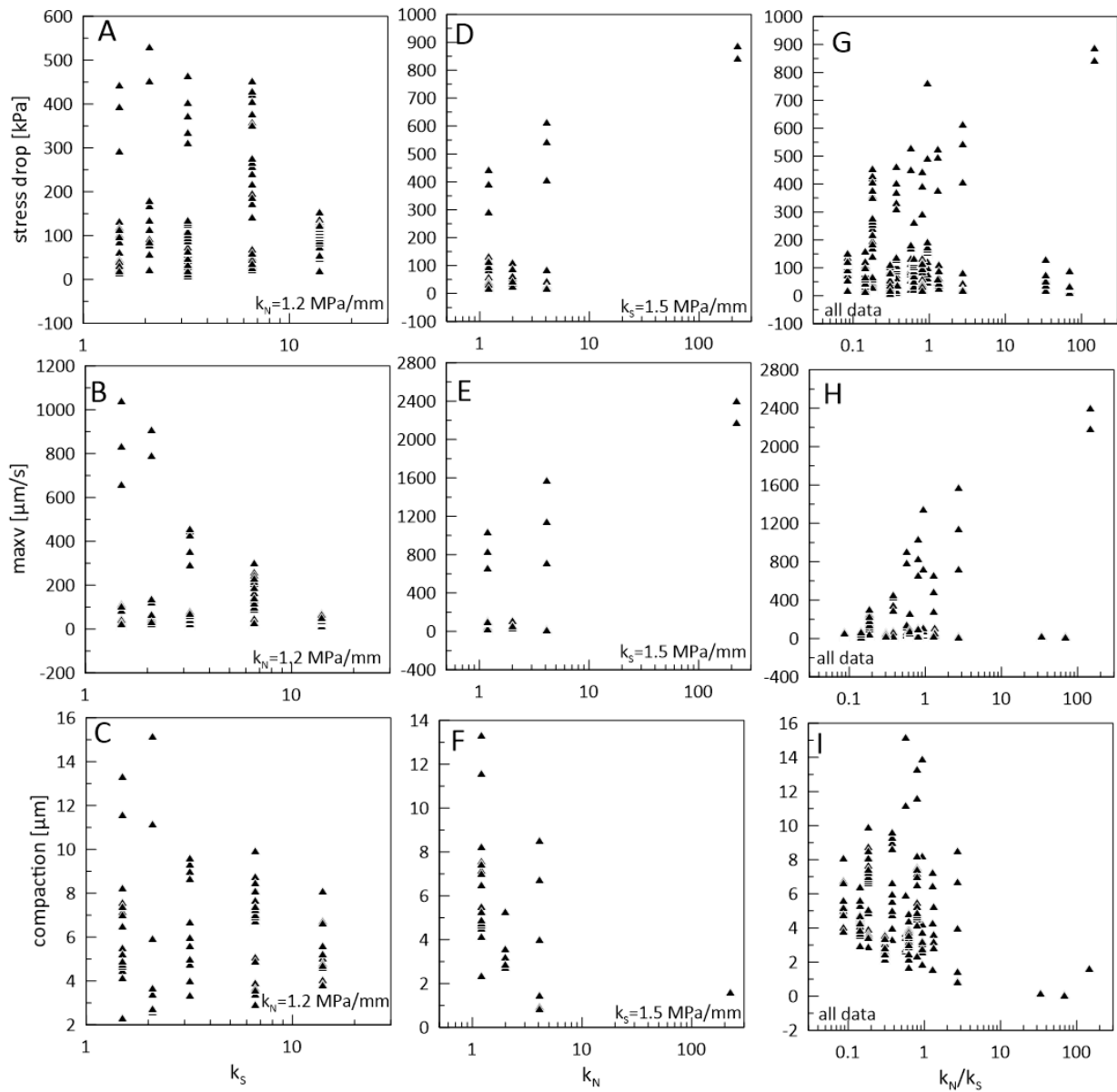


Figure 3.7: Stress drop, peak slip velocity and compaction during the slip event with varying shear stiffness (A-C), where the normal stress is kept constant at 1.2 MPa/mm, normal stiffness (D-F), where the shear stiffness is kept constant at 1.5 MPa/mm and (G-I) all data plotted over the ratio of fault normal stiffness to shear stiffness  $k_N/k_S$ .

## 3.5 Discussion

### 3.5.1 Effects on friction

Our results clearly show an inverse dependence of friction coefficient on the applied normal stiffness (Figure 3.4A). Volumetric strain induces work against the normal stress; dilation increases the observed friction, whereas compaction decreases the apparent friction (Edmond and Paterson, 1972; Marone et al., 1990). Marone et al. (1990) show that friction coefficient increases with dilation rate as:  $\mu = \mu_0 + (d\phi/d\gamma)$ , in which  $d\phi/d\gamma$  is the change in porosity per change in shear strain. The higher friction coefficient we observe throughout the experiment at lower  $k_N$ , could therefore be explained by a continuous porosity increase with shear strain or decreasing porosity at high  $k_N$ . The volumetric strain could occur as dilation when the normal stiffness is low, since dilation requires less work against lower stiffness, but we cannot measure vertical displacement accurately enough in our set-up to quantify dilation or compaction.

The increase in frictional stability parameter  $a-b$  that we observe with decreasing  $k_N$ , we suggest can also be explained by volumetric deformation. Our data is inconclusive, but the increase in  $a-b$  is likely due to an increase in  $a$  with decreasing  $k_N$ . The definition of the rate-and-state parameters is empirical, but  $a$  has been related to creep at the asperity contacts, which is an Arrhenius activated process that depends on an activation volume (Rice et al., 2001). It has been used to explain higher values for  $a$  when the deformation volume is larger (Ikari and Hüpers, 2021). As we explain the higher friction coefficient by more volumetric strain occurring at lower  $k_N$ , the larger deformation volume might also explain the larger values for  $a$  and therefore  $a-b$  we observe at lower  $k_N$ . However, our frictional data is not very clear whether  $a-b$  increases with decreasing  $k_N$  because of an increase in  $a$  or that this might be accompanied by a decrease in  $b$  with decreasing  $k_N$ .  $b$  values are interpreted as a change in contact area with changing sliding velocity (Dieterich and Kilgore, 1994; Ikari et al., 2016). Dilation increases the pore space and therefore reduces the real contact area in a gouge (Wang and Scholz, 1994; Beeler, 2007). Lower real contact areas lead to higher effective normal stresses at the contact, which can lead to faster contact growth and therefore high  $b$  values. If this mechanism occurs during our experiments, this would result in higher  $b$  values at lower  $k_N$ , which we do not observe, therefore an increase in  $a$  due to more volumetric deformation at low  $k_N$  seems the best explanation for the observed increase in  $a-b$  with decreasing  $k_N$ .

### 3.5.2 Occurrence of stick-slip

#### 3.5.2.1 Critical stiffness $k_c$

For the events that occur at constant high  $k_N$  of 223 MPa/mm (left column in Fig. 3.5), that shows the transition through symmetrical stable oscillations to large asymmetrical stick-slip events with decreasing  $k_S$ , the stiffness criterion  $k_S < k_c$  that is explained in the methods, can explain the occurrence of the different event types. The symmetrical, stable oscillations in slip have been described as the laboratory equivalent of slow slip events (Scuderi et al., 2016b; Leeman et al., 2018). Slow slip events with relatively long stress drop durations occur when  $k_S \approx k_c$ , where the duration of stress drop decreases as there is a transition to fast audible stick-slip events when  $k_S < k_c$  (Scuderi et al., 2016b). We observe as the same transition as the events become asymmetrical, larger and faster with decreasing  $k_S$ . Therefore, the variety of events we observe at  $k_N$  of 223 MPa/mm fits the predicted and previously observed transition from stable sliding to symmetrical slow slip events, to fast stick-slip events.

Figure 3.8 shows a plot of  $k_S$  versus  $k_c$ , with the 1:1 line representing the stiffness criterion indicated.  $k_c$  does not show any clear trends with shear or normal stiffness. Strictly speaking, the stiffness criterion is only satisfied for two experiments with  $k_N=1.2$  MPa/mm, which indeed show stick-slip events. The events that occur at  $k_N=4.1$  MPa/mm, including the large stick-slip events when  $k_S=3.2$  MPa/mm, that do not fit with the pattern in figure 3.5, can almost be explained by

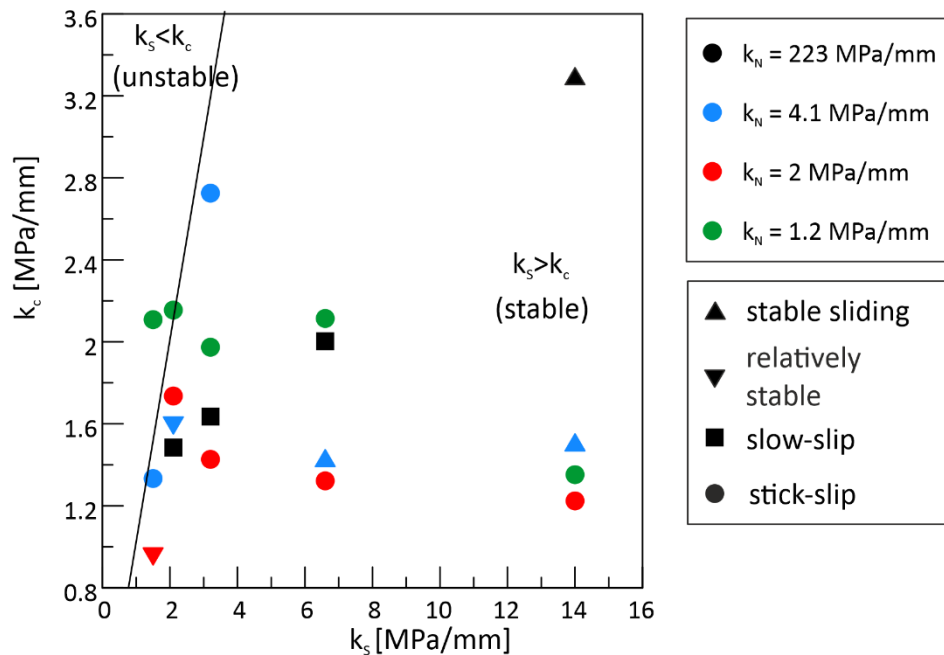


Figure 3.8: Critical stiffness  $k_c$  calculated from friction parameters over shear stiffness  $k_S$ , indicated is the 1:1 line where the critical stiffness theory predicts the transition from stable to unstable sliding. Note for the experiment with  $k_N=223$  and  $k_S=1.5$  the RSF parameters could not be fitted and  $k_c$  is not calculated.

the critical stiffness criterion. The events that show stick-slip behavior are the close to satisfying the critical stiffness criterion, whereas the stable experiments are far away from satisfying the critical stiffness criterion. The experiment at  $k_N = 2$  MPa/mm and  $k_S$  is 1.5 MPa/mm also does not fit the pattern in figure 3.5, because sliding is stable for the first 1.0 mm of displacement of the last velocity step, and small slip instabilities only start with continued sliding after  $>1.3$  mm of displacement. This surprisingly stable experiment can be explained by being relatively far below the stiffness criterion. It should be noted that  $k_c$  values are calculated using the velocity step at 7 mm displacement, whereas the slip events generally occur after the velocity step at 10 mm displacement. The velocity increase from 1 to 10  $\mu\text{m/s}$  is the same for those two steps, but the slip instabilities make it difficult to get reliable  $a-b$  and  $D_c$  values from the second step at 10 mm displacement. For the experiment with the largest stick-slip events at  $k_S=1.5$  MPa/mm and  $k_N=1.2$  MPa/mm, the velocity step at 7 mm displacement could also not be modelled reliably and  $k_c$  is not calculated. Frictional behavior can change over displacement, although we show in Chapter 2 that for the quartz  $a-b$  and  $D_c$  vary little with displacement after an initial run-in phase. Only small variations in frictional parameters could increase  $k_c$  enough to explain the variations in sliding behavior observed at low  $k_S$ , but not those at high  $k_S$  and low  $k_N$ .

The largest events that occur, at  $k_S=1.5$  MPa/mm and  $k_N=223$  or 4.1 MPa/mm, and during the experiment with  $k_S=3.2$  MPa/mm and  $k_N=4.1$  MPa/mm (Fig. 3.6B), resemble events predicted by slip weakening models or dynamically propagating cracks (Ida, 1972; Palmer and Rice, 1973; Andrews, 1976; Freund, 1979). These models predict the shear stress to fall from a high yield shear stress level or static friction, over a characteristic length scale, to a lower value of dynamic or sliding friction. The energy released by the stress drop is converted into surface energy that dynamically propagates the formed crack. These early earthquake models have the drawback that they do not explain how the shear stress level or friction can increase again and therefore cannot explain the recurrence of stress drops. In our experiments, we see these kind of events recur two or three times, after which they may disappear ( $k_S=1.5$  and  $k_N=4.1$  MPa/mm), but they can reappear after continued sliding ( $k_S=3.2$  and  $k_N=4.1$  MPa/mm). The occurrence of these events is well-explained by the critical stiffness criterion, yet occurrence of such large stress drops warrant further research.

The events that occur at constant high  $k_S$  and low  $k_N$  of 1.2 or 2 MPa/mm, cannot be explained by the critical stiffness criterion.  $k_N$  was shown to influence friction parameter  $a-b$  (Figure 3.4C), but the lower  $a-b$  values are measured at higher  $k_N$ . Higher  $k_N$  values therefore give stronger velocity-weakening behavior, based on which the slip instabilities would be expected at high  $k_N$ , not at low  $k_N$  as we observe. Despite the decreasing  $a-b$  values for increasing  $k_N$ , and  $k_c$  increasing

for decreasing  $a-b$  (Equation 3.5), there is no clear dependency of  $k_c$  on  $k_N$  (Fig. 3.8). The critical stiffness criterion can therefore not explain why slip events are observed when only  $k_N$  is lowered, as the influence of  $k_N$  on  $k_c$  is minor.

### 3.5.2.2 *Wrinkle-like slip pulses*

An alternative explanation for the events that occur at low  $k_N$ , but high  $k_S$  is that these events occur by a different mechanism that is not described by the stiffness criterion. An unavoidable effect of reducing the normal stiffness on the top of the sample, which in this apparatus cannot be matched with a similar reduction of normal stiffness on the bottom of the sample, is that there is a difference in the normal stiffness on both sides of the fault. Modelling studies have revealed fundamental differences between sliding behavior of elastically similar and elastically dissimilar solids (Adams, 1995; Ben-Zion, 2001; Rice et al., 2001). In elastically dissimilar solids a different type of instabilities can occur, described as the wrinkle-like slip pulses or Weertman slip pulse (Weertman, 1980; Andrews and Ben-Zion, 1997; Brietzke et al., 2009).

The wrinkle-like slip pulse is analogous to the wrinkle in a carpet, where material dilates and net movement in the direction of the wrinkle occurs (Andrews and Ben-Zion, 1997; Andrews and Harris, 2005). The wrinkle-like slip pulse propagates at the generalized Rayleigh velocity, for frictionless slip without opening (Weertman, 1980; Rice et al., 2001). When there is an elasticity contrast, this type of events can occur as long as the generalized Rayleigh velocity exists, which for typical rocks is the case for S-wave velocity contrasts of up to 30-40% (Shi and Ben-Zion, 2006). Currently the discussion is not whether wrinkle-like slip pulses occur, but how important they are in natural settings, and if they have a significant influence on rupture with crack-like propagation (Andrews and Harris, 2005; Brietzke et al., 2009). The slip instabilities we observe at high  $k_S$ , but low  $k_N$ , where the stiffness criterion is not satisfied and the occurrence of instabilities can therefore not be explained as crack-like ruptures, may however have a large component of wrinkle-like slip pulse.

Characteristics to distinguish wrinkle-like slip pulses are that they propagate only in one direction (Weertman, 1980; Andrews and Ben-Zion, 1997), the pulses commonly show self-sharpening and can diverge (Ben-Zion and Huang, 2002), and comparably low rupture propagation speeds limited to the generalized Rayleigh velocity (Weertman, 1980). These properties to distinguish between wrinkle-like slip and crack-like slip could be measured in laboratory experiments using for example acoustic emission sensors (Shlomag and Fineberg, 2016), but our device is not equipped with those sensors.

Other important characteristics is that compared to crack-like slip, wrinkle-like slip pulses have more fault-normal movement (Ben-Zion, 2001), which results in stronger ground motion (Brietzke et al., 2009) and a measurable drop in contact area and normal stress excursion (Shlomai and Fineberg, 2016). Numerical modelling studies indicate that as the stiffness contrast increases, slip and slip velocity should increase (Ben-Zion and Huang, 2002; Shi and Ben-Zion, 2006). We observe that indeed the events that occur at low  $k_N$  have more compaction, which as explained in the methods is in fact a normal stress drop (Fig. 7F), consistent with what would be expected if these events have a larger component of wrinkle-like slip. To see if slip and slip velocity increase with stiffness contrast, we compare the slip instabilities that occur when  $k_N=2.0$  and  $1.2$  MPa/mm at high  $k_S$ , because these are most likely pure wrinkle-like slip pulses. We measure the average of all slip instabilities during the last millimeter of sliding (Fig. 3.5), which for the experiment at  $k_N=2.0$  and  $k_S=14$  MPa/mm is  $6.9$   $\mu\text{m}$  of slip with a peak slip velocity of  $33$   $\mu\text{m/s}$ . For the experiment with  $k_N=1.2$  and  $k_S=14$  MPa/mm, slip events have an average slip of  $11$   $\mu\text{m}$  and an average peak slip velocity of  $44$   $\mu\text{m/s}$ . The experiment with a larger stiffness contrast ( $k_N=1.2$  MPa/mm) therefore has larger event slip and higher slip velocities, as would be expected for wrinkle-like slip pulses.

When both  $k_N$  and  $k_S$  are varied, we observed irregular slip events (bottom right in Fig. 3.5). This is well-explained by combining our explanations that at these conditions both the critical stiffness criterion is satisfied and wrinkle-like slip pulses may occur. Both type of events can influence each other, crack-like slip may trigger secondary wrinkle-like slip pulses and wrinkle-like slip pulses can lower the shear stress on asperities to cause crack-like slip (Brietzke et al., 2009). This also explains why the largest events occur at high  $k_N$  and low  $k_S$  (Fig. 3.5&3.7), because the crack-like slip is not triggered by wrinkle-like slip pulses.

### 3.5.2.3 *Earthquake scaling relationships*

Despite the different triggering mechanisms we propose, we observe that slip event characteristics follow relationships known from previous laboratory work and nature. In figure 3.9, we distinguish between the events that occur at normal stiffness values of  $223$  and  $4.1$  MPa/mm (black) and the events that occur at normal stiffness values of  $2.0$  and  $1.2$  MPa/mm (blue). When  $k_N$  is  $223$  or  $4.1$  MPa/mm, there are no events at high  $k_S$  and therefore we infer there is no component of wrinkle-like slip at these values of  $k_N$ . This distinction is not necessary for the continuum we observe from slow to fast slip events where the inter-event sliding velocity is inversely related to the peak slip velocity during the events (Fig. 3.9A), as was also observed by Ikari (2019) and will be shown for the events in the Hikurangi margin in Chapter 4. Stress drop

increases with peak slip velocity (Fig. 3.9B), consistent with previous observations (Johnson and Scholz, 1976; Okubo and Dieterich, 1984) and the events that occur at low  $k_N$  follow the same trends as the events at high  $k_N$ . A plot of stress drop with recurrence interval (Fig. 3.9C) is largely consistent with previous work that has shown stress drop increases with recurrence interval (Kanamori and Allen, 1986; Vidale et al., 1994). The symmetrical slow events such as the example in figure 3.6A, which occur at high  $k_N$  and therefore are among the black data points, have lower than expected stress drops for the recurrence interval and plot below the general trend. This difference between SSEs and ordinary earthquakes has previously shown and has been linked to an inertial overshoot that enables ordinary earthquakes slip to overcome rough patches (Brodsky and Mori, 2007). Such an overshoot is larger in systems with lower  $k_S$  (Gu and Wong, 1991), which is also visible in our data by the stress drop that occurs directly after velocity-steps, which become larger with decreasing  $k_S$  (Figure 3.3B).

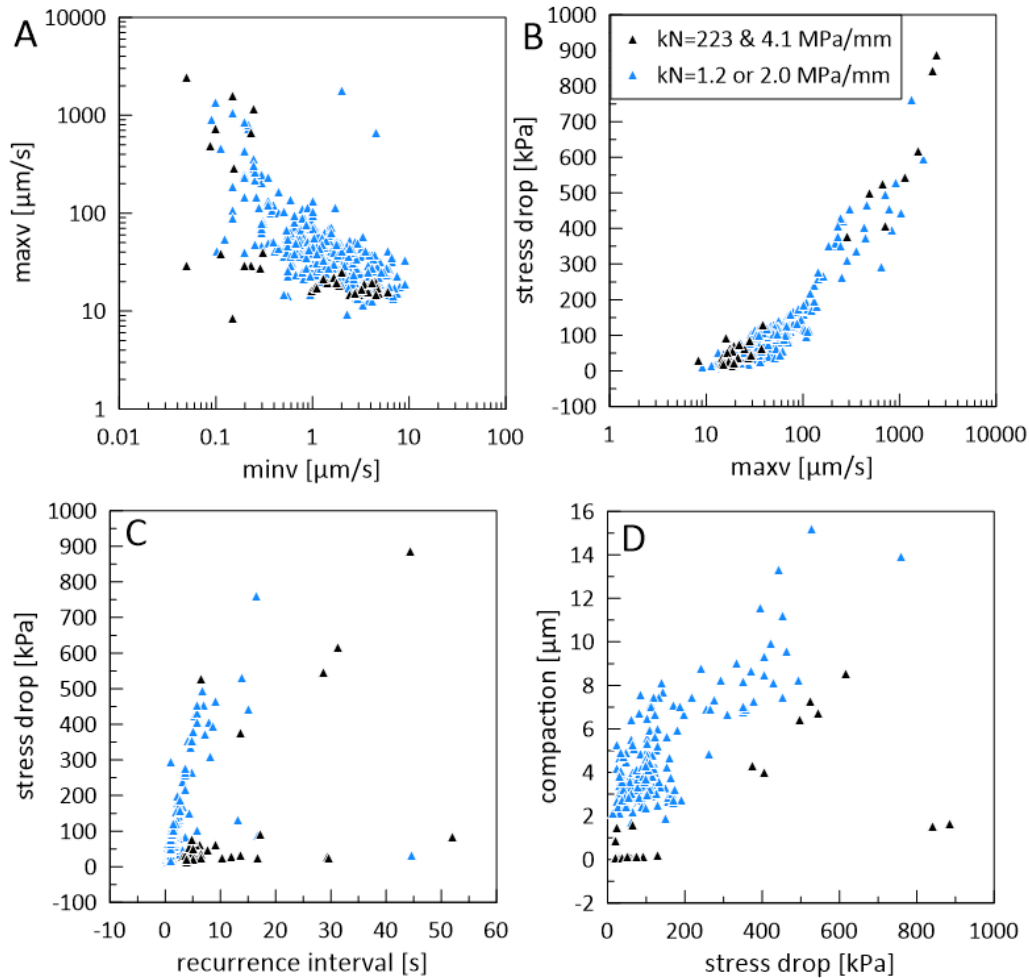


Figure 3.9: Relationships expected for earthquakes for all events that occur at  $v=10 \mu\text{m/s}$ . A: peak slip velocity over minimum slip velocity during the loading phase. B: event stress drop over peak slip velocity. C: Stress drop with recurrence interval. D: compaction during the stress drop over stress drop size. Black or blue points signify  $k_N$  values where wrinkle-like slip is limited (black) or common (blue), see text for explanation.

For the slip events with high stress drops, there may be a difference between the events at high  $k_N$ , that follow a shallower trend than the events at low  $k_N$  (Fig. 3.9C). The extra component of wrinkle-pulse slip for events at low  $k_N$  may lead to higher stress drops for the same recurrence interval, although more slip events at high  $k_N$  would be helpful to confirm this. The compaction during slip events (Fig. 3.9D), that did not show a clear trend with either shear or normal stiffness, does show a trend with increasing stress drop. As mentioned before, slip events with a component of wrinkle-like slip have more ground motion (Brietzke et al., 2009) and more fault-normal motion on the more compliant side (Ben-Zion, 2001). The observation that slip events with low  $k_N$  have relatively higher compaction for the same stress drop can be explained by a component of wrinkle-like slip. However, the way compaction is measured (see Methods) from an instantaneous drop in the normal stress and the spring stiffness also means that small amounts of compaction during experiments with low  $k_N$  are not observed.

### 3.5.3 Application for natural faults

#### 3.5.3.1 Shear stiffness

Our findings consist of two components; reducing shear stiffness can induce a transition from stable sliding to slow slip events to fast slip events, and reducing normal stress on one side of the fault can also trigger a transition from stable sliding to short-period stick-slip events. The importance of shear stiffness and the transition in slip behavior has been previously studied and depends largely on the development of  $k_c$  with depth, which varies with friction parameters  $a$ ,  $b$  and  $D_c$  and effective normal stress (Scholz, 1998; Leeman et al., 2016). The stiffness of the host rock  $k_S$  varies with depth because it depends on the host rocks shear modulus, which increases with depth (Jeppson and Tobin, 2015), but this effect is small compared to the variation in  $k_c$  with depth. This gives rise to the general picture of a transition in slip behavior with depth, where in the seismogenic zone the condition  $k_S < k_c$  is met and earthquakes occur, which is flanked on both the updip and downdip sides by a transition region where slow slip events may occur (Scholz, 1998; Saffer and Wallace, 2015).

In nature various observations show the transition from stable to slow to fast slip with depth is not as simple as we describe, and occurrence of slow slip and the interaction with fast earthquake slip may be complex (Obara and Kato, 2016). The wrinkle-like slip pulses that we observe cannot explain this complexity. Whereas we see interacting events when both the critical stiffness criterion is satisfied and the fault-normal stiffness is reduced enough for wrinkle-like slip pulses to occur, there are no experiments where an interaction between slow slip events and

wrinkle-like slip pulses occur. Instead, only fast events occur when  $k_S \approx k_C$  and  $k_N$  is low. The connection from laboratory observations of slow to fast slip events caused by a reduced shear stiffness, to observations of natural earthquake behavior has been previously studied (Bürgmann, 2018; Ikari, 2019) and our observations with varying shear stiffness largely confirm previous laboratory studies (Baumberger et al., 1999; Scuderi et al., 2016b; Leeman et al., 2018). The condition how stiffness controls earthquake behavior is therefore relatively well constrained, but one important factor is often overlooked, which is how the shear stiffness on natural faults may vary in space and time.

### 3.5.3.2 *Stiffness reduction and asymmetry*

Natural processes that may influence the overall stiffness of the overlying rock and therefore also the vertical stiffness include lithification, gouge formation or fault zone brecciation and loading effects. Lithification cements pore space in rock, therefore making stronger bonds that are likely to deform less upon compression, and therefore fault normal stiffness increases. Brecciation, gouge formation or off-fault damage on the other hand reduce the normal stiffness (Singh and Pathak, 2013). Another effect is that of loading, since loaded materials are stiffer. This results in an increase in shear modulus with normal stress (Jeppson and Tobin, 2015) and also normal stiffness increases for higher applied normal stress (Singh and Pathak, 2013). An additional point is that generally a stressed material is harder to deform, an effect commonly known in laboratory deformation devices, as measured shear stiffness increases with normal load (Chapter 4). Therefore, it seems likely that the opposite effect,  $k_N$  depending on shear stress also occurs and the interplay between stiffness and the continuous shear loading and unloading during earthquake cycles might be complex.

Processes that may cause asymmetry of stiffness in a fault zone can be roughly divided into differences in intrinsic rock properties and asymmetric damage zones. Apart from pure strike-slip faults, faults will juxtapose rocks from different depths, which have different degrees of lithification, which as previously discussed will influence the stiffness. When fault offset is large enough, the fault may also juxtapose two different lithologies, with different elastic moduli that control the rock stiffness. Damage zones around faults, regions of increased fracture density or pulverized rocks, can be asymmetric (Dor et al., 2006). The microfracture density decreases with the distance from the fault core and the stiffness of the rock increases (Faulkner et al., 2006), slightly larger, mesoscopic fractures can decrease the elastic shear modulus up to 75% (Griffith et al., 2009).

### 3.5.3.3 Normal stiffness and slip event occurrence

To relate our new findings, that decreasing the normal stiffness on one side of a fault increases the friction coefficient, increases  $a-b$  and causes slip instabilities, to natural settings, we point out that at this moment we cannot test if the behavior we observe is due purely to the reduction of normal stiffness, or due to the asymmetry in elastic properties this induces.

Laboratory experiments under conditions where we expect and influence of normal stress show that increasing cementation, which should lead to higher  $k_N$ , causes negative and decreasing  $a-b$  and increasing stick-slip behavior (Ikari and Hüpers, 2021). Gouge formation during sliding of two initially bare rock surfaces has an opposite effect, a thicker layer of gouge, which should lower  $k_N$ , leads to higher  $a-b$  values and stabilization in slip behavior (Marone et al., 1990). This shows that both of these studies have frictional parameters that develop in a similar way to what we observe, increasing  $a-b$  for decreasing  $k_N$ . However, neither of these studies reports that gouge formation or lithification leads to unstable slip.

Whereas the increase in friction parameter  $a-b$  might be explained as a direct effect of decreasing  $k_N$ , the slip instabilities that occur at low  $k_N$  seem to require asymmetry in  $k_N$ , which we would expect if these events are wrinkle-like slip pulses. In our experiments, the slip instabilities occur when  $k_N$  is lowered to 2.0 or 1.2 MPa/mm and do not occur when  $k_N$  is 4.1 MPa/mm. The normal stiffness of the sample below the ‘fault zone’ is unknown, but if it is in the range of the unmodified normal stiffness above the sample (223 MPa/mm), a relatively large asymmetry in stiffness is required before these slip events occur.

That the stiffness contrast has to be large could explain why it is argued that the effect of wrinkle-like slip pulses is limited on natural faults (Andrews and Harris, 2005). Le Pichon et al. (2005) report for the North Anatolian fault the ratio of elastic stiffness on both sides of the fault can be 10 and 30, due to combined effects of fault gouge presence, fluid pressures or the difference between static elastic properties and the dynamic elastic properties measured by seismic velocities. If the more compliant side of the fault is also more permeable, which might be expected if fracture density is higher, elastic and poro-elastic effects enhance each other in reducing the normal stress and promoting wrinkle-like slip pulses (Dunham and Rice, 2008). Therefore it seems possible that large stiffness asymmetry may occur on natural faults. One puzzling factor is how self-sustaining this mechanism is, as numerical models and geological observation suggest the stiffer side of the fault get damaged more (Ben-Zion and Shi, 2005; Dor et al., 2006). Successive ruptures increasing the damage preferentially on the stiffer side would reduce the

stiffness of the stiffer lithology and therefore reduce the stiffness contrast. However, recurring uni-directional ruptures on faults with a stiffness contrast have been used to explain the highly asymmetric damage zone on a strike-slip fault in Japan (Mitchell et al., 2011).

### 3.6 Conclusion

We use laboratory direct shear experiments to study the influence of host rock stiffness on frictional behavior and slip stability, by independently varying the fault-normal stiffness  $k_N$  and the shear-parallel stiffness  $k_S$ . A lower  $k_N$  causes the friction coefficient to increase and the frictional stability parameter  $a-b$  to be less negative, which we propose is due to more volumetric deformation at low  $k_N$ . At a constant, high  $k_N$ , lowering the shear stiffness  $k_S$  leads to a transition from stable sliding, through slow slip to large stick-slip events, which is well explained by the critical stiffness theory. Decreasing the fault normal stiffness, leads to small, rapid slip instabilities, which are unexpected based on the critical stiffness theory, because the higher  $a-b$  at low  $k_N$  predicts a tendency for more stable sliding. These events can be explained as wrinkle-like slip pulses, that occur when there is a contrast in stiffness on the fault, which is the result of our experimental set-up which only allows for decreasing  $k_N$  on one side of the fault. When both shear and fault normal stiffness are low, we observe chaotic events, as a result of both mechanisms interacting.



## 4 Plate-rate frictional behavior of sediment inputs to the Hikurangi subduction margin: How does lithology control slow slip events?

*Agathe M. Eijsink and Matt J. Ikari*

### Highlights:

- Hikurangi SSEs occur in carbonate-rich sediments
- Rate-and-state friction and critical stiffness criterion can partly explain SSEs, but SSEs can occur under velocity-strengthening conditions
- SSE characteristics fit with trends expected from ordinary earthquake seismology
- SSE generation in Hikurangi is probably related to heterogeneity on fault surfaces

### 4.1 Abstract

The northern Hikurangi subduction margin hosts shallow (<15 km) slow slip events (SSEs), which recur every 1-2 years. The sedimentary sequence on the incoming plate is representative of the shallow fault material where the SSEs will take place once they enter the subduction zone. Frictional behavior is material-specific and depends on sliding velocity, but it is unknown how these sediments behave at plate-rate velocities. Knowledge about the frictional behavior of these sediments is required to know which lithologies are capable of hosting SSEs, and what mechanisms are causing them. We performed laboratory shearing experiments testing the major lithologies sampled during IODP Expedition 375, at velocities ranging from the plate convergence rate at the Hikurangi margin (5 cm/year), up to those characteristic of the shallow SSEs (160 and 530 cm/year), under simulated in-situ as well as standardized conditions. At these conditions, the stronger calcite-rich pelagic sediments display the velocity-weakening behavior required for slip events, whereas most other lithologies are velocity-neutral to strengthening. We observe spontaneous SSEs in the calcite-rich pelagic sediments, which show partial locking in between sliding events, which fits with the spectrum of slow to fast earthquakes. At the Hikurangi margin, this requires the carbonate-rich unit is introduced in the interplate fault zone, which we suggest occurs because the rough incoming plate makes a geometrically complex fault zone in which a variety of lithologies can be present.

## 4.2 Plain language summary

In the Hikurangi subduction zone offshore north-east New Zealand, the movement between the downgoing and overriding tectonic plates can occur as slow slip events (SSEs). During SSEs the two plates move relative to each other, a process in many aspects similar to ordinary earthquakes, except SSEs take weeks instead of seconds and no ground-shaking can be felt on the surface. SSEs occur in many subduction zones worldwide, but at the Hikurangi margin they occur shallow, relatively often and close to many mostly land-based GPS stations that track the movement of the two plates, which makes them ideal to study. A recent research expedition (IODP expedition 375) to learn more about the circumstances that control where and when SSEs occur, drilled the stack of sediments going into the subduction zone. In this paper, we test all the major different sediment types going into the subduction fault zone to find out which one of them is responsible for the SSEs. Using a laboratory device that mimics the subduction zone, we find the calcite-rich samples spontaneously show slip events that are similar to the SSEs observed in the Hikurangi margin.

## 4.3 Introduction

Over the last few decades, slow slip events (SSEs) have been recognized in most major subduction zones worldwide (Schwartz and Rokosky, 2007). SSEs have longer durations (weeks to months) than low frequency (<1 s) and very low frequency (~seconds) earthquakes (Ide et al., 2007), but in contrast to those other slow earthquakes, SSEs do not emit detectable seismic waves. For this paper, we follow the definition of Bürgmann (2018), that an SSE is an aseismic slip transient with a duration of minutes to decades. With the lack of a seismic signal, although some low-frequency seismic energy can be generated, SSEs have been recognized mostly by the deployment of dense GPS networks, which measure the movement of the overriding plate. SSEs manifest themselves as a temporary reversal of the upper plate moving together with the subducting plate, to movement in the opposite direction, towards the trench, during periods of slip on the subduction interface (Dragert et al., 2001). Alternatively, SSEs can be observed by migration of the non-volcanic, episodic tremor that can accompany SSEs (Obara et al., 2004), vertical displacement measured by pressure changes in ocean bottom pressure gauges (Linde and Sacks, 2002) or a combination of those methods (Ito et al., 2013). At the Hikurangi margin, development of ocean bottom pressure gauges have revealed that slow slip propagates to <2 km of the seafloor (Wallace et al., 2016), providing an excellent study opportunity (Wallace, 2020).

This motivated International Ocean Discovery Program (IODP) Expedition 375 (Wallace et al., 2019), during which the composition and conditions in the subducting and overriding plate were characterized and observatories were installed to monitor temporal variations during multiple SSE cycles.

SSEs have been predicted to occur at the transition zones from stable to unstable sliding from friction experiments (Baumberger et al., 1994; Leeman et al., 2016), models (Ruina, 1983; Gu et al., 1984) and theory (Rice and Ruina, 1983), which translated to a subduction zone means the updip and downdip limits of the seismogenic zone (Scholz, 1998). Frictional behavior is material specific and depends on sliding velocity (Dieterich, 1978). The velocity-dependent nature of friction is important because only if friction decreases with sliding velocity (velocity-weakening behavior), will fault spontaneous speed up in an earthquake like manner (Scholz, 1998). Recent studies have shown there are significant differences between sliding friction at realistic plate-rate velocities of nanometers per second (centimeters per year) and the higher velocities more commonly used in laboratory experiments of micrometers per second (Ikari and Kopf, 2017). Spontaneous laboratory slow slip events can under specific circumstances, including sliding at such low, realistic velocities (Rabinowitz et al., 2018; Ikari, 2019). Since the velocity-dependent frictional behavior is material-specific, it is important to test the lithologies going into the subduction zone. Because at the Hikurangi margin, SSEs occur shallow compared to other subduction zones, sediments going into the subduction zone will not undergo extensive changes from the state they are in at the seafloor, to their state along the megathrust where they host the SSEs. Therefore, sediments cored at a relatively undisturbed part of the incoming plate, IODP site U1520 (Fig. 4.1) have the same lithology, deformation history and microstructures as the sediments in the deformation zone, which are inaccessible for coring. Assuming the lithologies cored at site U1520 are representative for the sediments going into the megathrust deformation zone, one of these must be responsible for the shallow SSEs observed at the Hikurangi margin.

The aim of this paper is to test the lithological controls on SSE occurrence, using laboratory friction experiments for all the main lithologies cored at site U1520 by IODP Expedition 375, including sliding at velocities close to plate-rate and velocities representative for those reached during SSEs. We use the presence or absence of spontaneously occurring slow slip events combined with analysis of the frictional behavior and critical stiffness to interpret the origin of shallow slow slip events observed at the Hikurangi subduction margin.

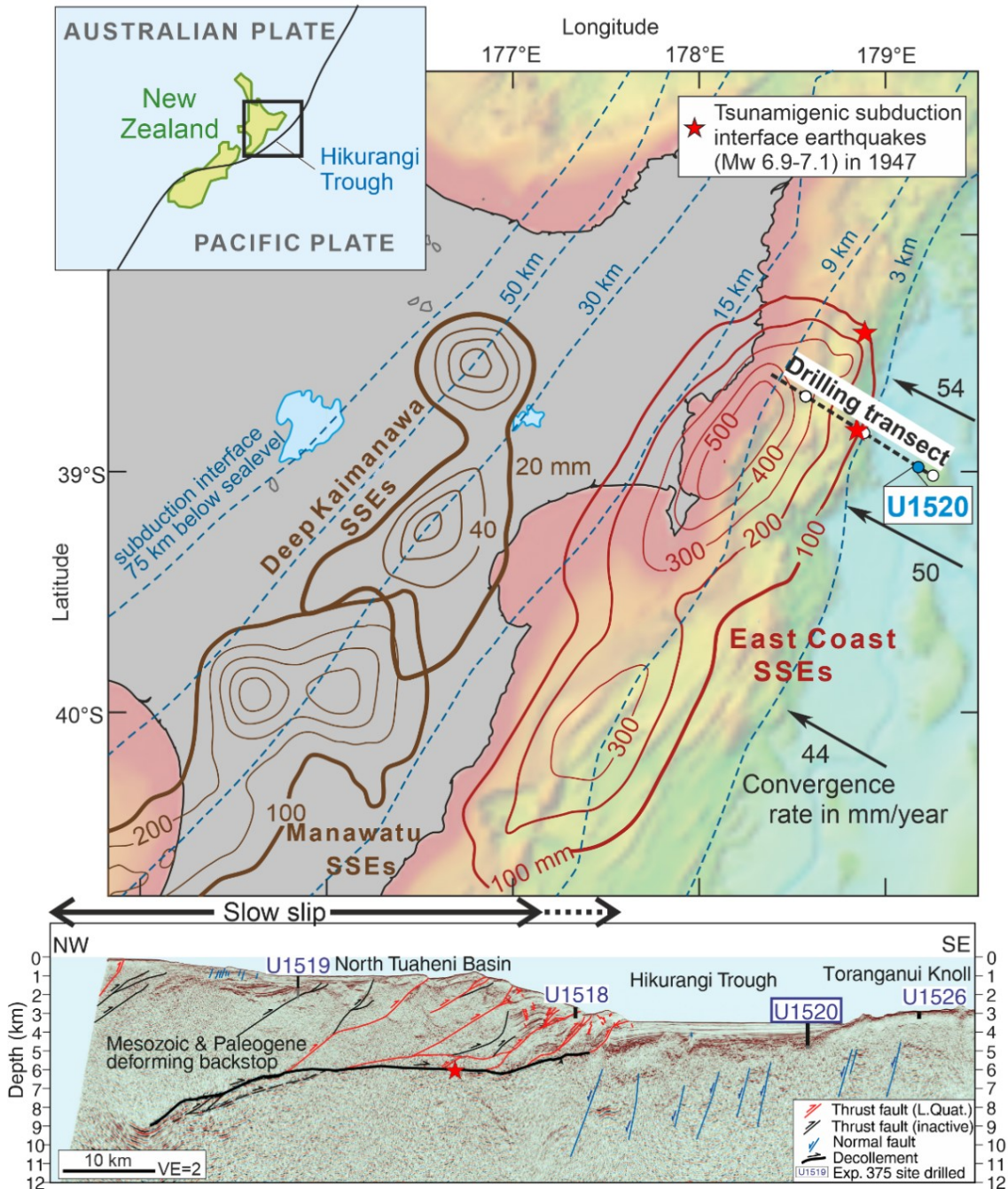


Figure 4.1 Geological setting: Bathymetric map (NIWA 2016) with outlines of cumulative slip during slow slip events between 2002 and 2014 (Wallace, 2020), the shallow East Coast SSEs are in red. Black arrows with plate convergence rate use data from Wallace et al. (2012), blue dashed lines indicate depth to subduction interface (data from Williams et al., 2013). Indicated is the drilling transect of IODP Expedition 375, with the location of site U1520 used in this study in blue. Below: Seismic section 05CM-04 along the drilling transect, interpretation by Barnes et al. 2020, with the interpreted extent of the slow slip event in 2010 indicated on top. (After Wallace 2020 and Barnes et al., 2020).

#### 4.4 Geological Setting

At the Hikurangi subduction margin, offshore the east coast of the North Island of New Zealand, the Pacific plate is subducting underneath the Australian plate (Fig. 4.2) with oblique plate convergence rates of 3-6 cm/year, increasing from south to north, with values around 5 cm/year at our study location (DeMets et al., 1994; Wallace et al., 2004). The lateral component is accommodated largely (35-80%) by dextral movement along the transform North Island fault system (Nicol and Beavan, 2003; Nicol and Wallace, 2007) and by rotations of the tectonic blocks that make up the north island (Wallace et al., 2004, 2012a). The subducting crust is relatively old and cold (Fagereng and Ellis, 2009), with a shallow subduction angle (10 degrees; (Reyners, 1998)) attributed to the subduction of the buoyant Hikurangi Plateau (Wood and Davy, 1994). The incoming plate is marked by a rough topography with subducting seamounts in the north, with increasing sediment cover towards the south (Lewis et al., 1998; Plaza-Faverola et al., 2012). Subducting seamounts have caused erosion of the accretionary wedge in the north, leaving erosional scars (Lewis et al., 1998; Collot et al., 2001), which have resulted in a steep and narrow accretionary wedge in the north, that widens southward (Ghisetti et al., 2016). Internal deformation in the overlying plate is limited, meaning most deformation takes place on the subduction megathrust (Nicol and Beavan, 2003).

The shallow SSEs occur at the northern part of the Hikurangi subduction margin, offshore from Cape Turnagain to the Raukumara Peninsula, where the margin is characterized by a high number of seamounts and erosion of the accretionary prism. Deeper (25-60 km) SSEs occur further south along strike, although Wallace and Eberhart-Phillips (2013) found smaller deep SSEs occur directly downdip from the shallow East Coast SSEs. The deeper SSEs have long durations (>200 days) and recurrence intervals of 5-6 years (Wallace and Beavan, 2010), whereas the shallow SSEs last about 2-4 weeks and recur every 18 to 24 months in the study area and approximately every 5 years further south near Cape Turnagain (Wallace et al., 2012b). The shallow SSEs can reach up to ~15 cm slip (Wallace and Beavan, 2010), similar to the deep, southern SSEs which were modelled to have ~15 cm of slip on the main slipping patches (Wallace et al., 2012b). Recently employed ocean bottom seismometers and absolute pressure gauges have revealed ~5 cm of slip occurs within 2 km of the seafloor of which some might continue to the trench (Wallace et al., 2016). IODP expedition 372/375 took place in this area where shallow slow slip occurs (Fig. 4.1) and these shallow SSEs are the focus of this paper.

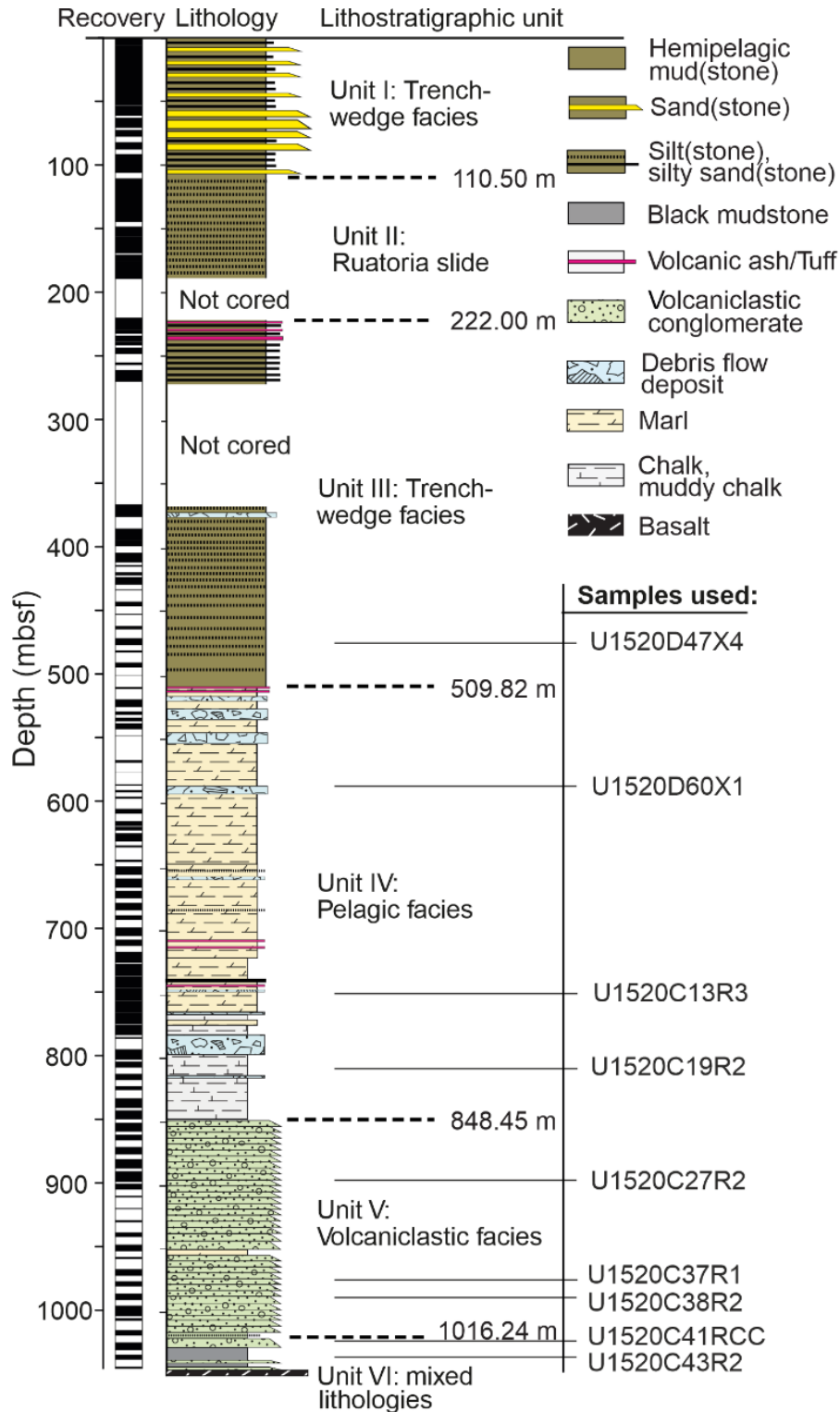


Figure 4.2 Lithostratigraphic overview of IODP site U1520, showing the depths and lithologies of the samples used in this study on the lower right (After: Barnes et al., 2019).

## 4.5 Materials and Methods

### 4.5.1 Materials

One of the targets of IODP expedition 375 was to characterize the sediments entering the Hikurangi subduction zone. The material used in this study comes from IODP Site U1520 (Fig. 1), which penetrates a relatively undisturbed sedimentary sequence on the incoming plate, in front of the part of the trench where the shallow SSEs take place (Fig. 4.1). The sequence is comprised of 6 lithological units (Fig. 4.2; see Barnes et al., 2019 for more detailed descriptions), starting with Unit I: a hemipelagic mudstone with coarser interbeds, interpreted as trench-wedge facies. Unit II consists of hemipelagic silt, with regularly spaced silty interbeds that are interpreted to be turbidites. Unit III also consists of hemipelagic mud and is similar to unit I, but interbeds are thinner and finer in grain size. Unit IV consists of ~350 m of pelagic carbonates, mostly marl with some intervals with higher clay content referred to as calcareous mudstone, and the lowermost ~50m chalk, all interbedded by debris flows and volcanic tuff layers. The 170m thick Unit V consists of volcanoclastic conglomerates made up of mm to cm scale clasts, cemented with calcite and zeolite. The deepest unit VI is highly variable in lithology with green and blue volcanoclastic conglomerates and mudstones, and also includes an organic-rich black mudstone.

For the experiments, Unit I and II are not considered, because these shallow sediments are most likely accreted into the accretionary prism present along the transect and the turbiditic Unit II might be a local feature (Barnes et al., 2019). Therefore, both of these units are not likely to form the décollement or cause the SSEs. From the other units, 9 different samples were selected, representing the major lithological components of the sediment column (Fig. 4.2, Table 4.1).

### 4.5.2 Friction experiments

We performed laboratory shear experiments using a single direct shear device (Giesa RS5, see inset in figure 4.2). We used 2 types of samples; (1) intact samples, which are cylinders trimmed from core samples with a diameter of 25 mm and a height of ~20-25 mm, or (2) powdered samples, for which core material was dried in a low humidity, room temperature drying box and then crushed and sieved to a diameter of <180  $\mu\text{m}$ . The powders were mixed with deionized water to form a stiff paste and cold-pressed into a cylindrical cell of the same diameter as the intact samples. For powdered samples, the two shear plates containing the cylindrical sample were then placed in the testing device, in a water basin filled with mock seawater, loaded with the normal stress and powdered samples were allowed to consolidate for ~24 hours.

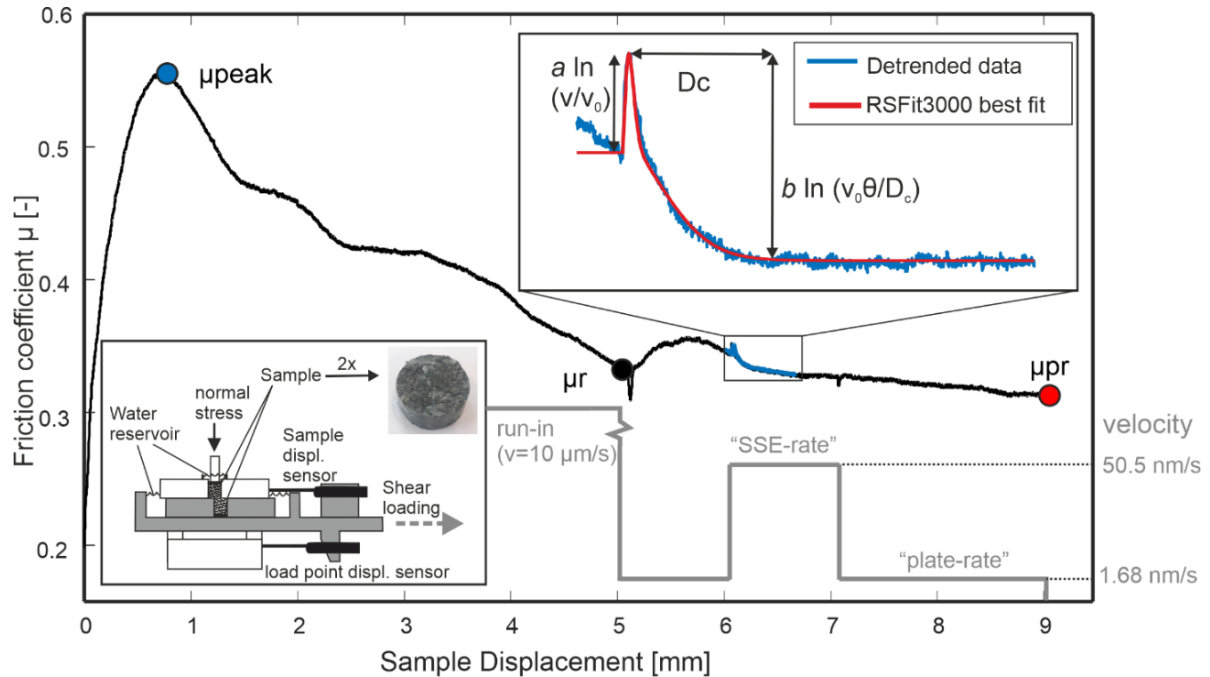


Figure 4.3: Data example of friction with displacement (AE018; intact volcanoclastic conglomerate, in-situ normal stress), indicated on the bottom are the imposed driving velocities (grey). Circles show where the friction coefficients  $\mu_{\text{peak}}$ ,  $\mu_{\text{ss}}$  (steady-state) and  $\mu_{\text{pr}}$  (plate-rate) are measured. Top right shows analysis of velocity-dependent friction upon a velocity-step. Inset on bottom left shows the experimental device (Giesa RS5), which imposes shear stress on the sample by displacing the grey part to the right. Note the two displacement sensors that distinguish between the displacement in the device (load-point) and that measured directly on the sample.

The experimental procedure first started with a direct measurement of cohesion, achieved by displacing the bottom plate of the sample cell relative to the upper plate, which induces shear loading of the sample. The test is conducted under zero normal load, and the sample is sheared for up to 2 mm, until failure. The peak stress during failure is the cohesion of the sample. After this, the sample cell was reset to its original position, for the intact samples, the water basin was filled with brine at this point, and consolidated for  $\sim 24$  hours (intact samples) or  $\sim 72$  hours (powdered samples) until the compaction rate becomes negligible. After this, the pore water pressure from the fully drained samples is assumed to be at atmospheric pressure as the water reservoirs are open to atmosphere, so that the applied normal stress can be assumed to be equal to the effective normal stress. The experiments were conducted at room temperature.

The direct shear device has two horizontal displacement sensors, one directly on the sample (sample displacement), and one close to where the horizontal shear stress is applied (load point displacement sensor) (Fig. 4.3). Driving velocities reported are the input velocity aimed for, and generally close to the load point velocity, calculated from the load point displacement data. The two displacement sensors allow for accurate comparison between the load point velocity and the sample velocity, which in the case of (slow) slip events differ. The choice of driving velocities is different for the tests under in-situ normal stress, and for tests under a reference normal stress of 10 MPa.

#### 4.5.2.1 *in-situ normal stress*

For the majority of the experiments, we applied a normal stress that represents the in-situ effective normal stress, which varies between 4.0 and 9.4 MPa and was calculated for each individual sample from the depth, measured shipboard density measurements on core samples and assuming hydrostatic pressure (Table 4.1). Intact samples were always subjected to the in-situ effective normal stress, since the intact structure of the sample is representative only for the effective normal stress at which it was formed. For samples that showed SSEs, we additionally conducted experiments on those samples with powdered equivalents at in-situ effective normal stress, to test the influence of the intact structure.

After consolidation, the shearing procedure started with an initial run-in phase at a driving velocity of 10  $\mu\text{m/s}$  for 5 mm of displacement (Fig. 4.3). This will form an initial surface along which the sliding will occur, and since 10  $\mu\text{m/s}$  is in the range of driving velocities commonly used in laboratory experiments, it also allows for comparison with previously published friction measurements. After the run-in, the shearing velocity was decreased to 1.68 nm/s or 5.3 cm/year, matching the plate convergence rate in the study area (4-6 cm/year (Wallace and Beavan, 2010)). After 1 mm of displacement, a 30x increase in shear rate was applied to 50.5 nm/s or 160 cm/year, which is in the range of velocities measured during shallow SSEs at the Hikurangi margin (Wallace et al., 2016). After another 1 mm of displacement, we decreased the shear rate to the plate-rate velocity again for another 2 mm of displacement (Fig. 4.3). The velocity steps are to determine the velocity dependence of friction (see section data analysis) and the longer final stage of sliding at plate-rate velocity was used to allow spontaneous SSEs to occur and to reach a microstructural steady state.

#### 4.5.2.2 *Standardized tests*

For samples that showed velocity-weakening behavior during in-situ normal stress experiments, we performed an additional series of tests at a standardized normal stress of 10 MPa. These tests allow comparison of those samples at similar conditions, since the applied normal stress affects the friction, the stiffness of the machine and influences the samples critical stiffness value, calculated from frictional parameters and the normal stress. Therefore, to isolate the effect of lithology on slip event occurrence, these tests at a constant normal stress are needed.

The samples for the “standardized” experiments at 10 MPa normal stress are made of powdered material, since the structure of the intact sample represents that of the in-situ state and not necessarily that of the same sample consolidated to higher normal stress. The shearing

procedure started with a similar initial run-in at 10  $\mu\text{m/s}$  for 5 mm of displacement, after which we decreased the driving velocity to 1.68 nm/s (plate-rate) for 0.7 mm of sliding. We then implemented a velocity stepping sequence using the commonly used  $\sim 3$ -fold velocity increases from 1.68 nm/s up to 168 nm/s, with 0.7 of displacement at each sliding velocity, to compare how frictional stability changes with velocity and since 3-fold increases are standard, this allows us to compare the values we find with previous work. Again we finish the sequence by a second phase of sliding at plate-rate velocity for 2 mm of displacement (Table 4.1).

#### 4.5.1 Friction data analysis

During the experiments, we measure the shear stress ( $\tau$ ) that is needed for sliding at our desired velocity. The shear stress depends on the coefficient of friction  $\mu$ , the effective normal stress  $\sigma'_n$  and the cohesion  $C$ :

$$\tau = \mu\sigma'_n + C \quad (4.1)$$

Assuming that cohesion is negligible on a well-formed sliding plane, which is formed during the run-in, we calculate the friction coefficient by normalizing the shear stress by the normal stress to compare the frictional behavior of experiments that all have different applied normal stresses. We report the friction coefficients at the peak ( $\mu_{peak}$ ) that occurs after sliding is initiated, the residual friction  $\mu_r$  at the end of the run-in at 10  $\mu\text{m/s}$ , and at the end of the experiment at a sliding velocity of 1.7 nm/s  $\mu_{pr}$ . The residual friction in most cases represents steady-state sliding friction, but some material have a slip-dependent friction trend, in which case friction does not reach a steady state within 5 mm of sliding. To compare those experiments, the residual friction is measured after the same amount of slip.

The velocity steps were used to determine the velocity-dependent frictional behavior. The evolution of the friction coefficient upon a change in velocity can be described used the following relationship, known as the rate-and-state framework (Dieterich, 1979; Ruina, 1983):

$$\mu = \mu_0 + a \ln\left(\frac{V}{V_0}\right) + b_1 \ln\left(\frac{V_0\theta_1}{D_{c1}}\right) + b_2 \ln\left(\frac{V_0\theta_2}{D_{c2}}\right) \quad (4.2)$$

$$\frac{d\theta_i}{dt} = 1 - \frac{V\theta_i}{D_{ci}}, i = 1, 2 \quad (4.3)$$

Table 4.1 list of samples and experiments

Sample	Unit: lithological description	Composition [wt.%] (abundance >5%)	Depth [mbsf]	Experiment	Sample type	Applied $\sigma_{xx}$ [MPa]	sliding velocities [mm/s] (displacement[mm])
U1520D47X4	III: siltstone	45% phyllosilicates, 21% plagioclase, 13% quartz, 5% calcite, 5% clinopyroxene	477.0	AE004 AE066	intact powder	4.0 10.0	10 000 (5 mm); 1.68 (1); 50.5 (1); 1.68 (2) 10 000 (5 mm); 1.68 (0.7); 5.05 (0.7); 16.8 (0.7); 50.5 (0.7); 168 (0.7); 1.68 (2)
U1520D60X1W	IV: marl	76% calcite, 14% plagioclase	587.6	AE005 AE060	intact powder	4.9 10.0	10 000 (5 mm); 1.68 (1); 50.5 (1); 1.68 (2) 10 000 (5 mm); 1.68 (0.7); 5.05 (0.7); 16.8 (0.7); 50.5 (0.7); 168 (0.7); 1.68 (2)
U1520C13R3	IV: marl (calcareous mudstone)	46% phyllosilicates, 38% calcite, 12% plagioclase	751.11	AE002 AE023 AE064	intact powder powder	6.5 6.5 10.0	10 000 (5 mm); 1.68 (1); 50.5 (1); 1.68 (2) 10 000 (5 mm); 1.68 (1); 50.5 (1); 1.68 (2) 10 000 (5 mm); 1.68 (0.7); 5.05 (0.7); 16.8 (0.7); 50.5 (0.7); 168 (0.7); 1.68 (2)
U1520C19R2	IV: chalk	99% calcite	807.4	AE011 AE034 AE062	Intact powder powder	7.1 7.1 10.0	10 000 (5 mm); 1.68 (1); 50.5 (1); 1.68 (2) 10 000 (5 mm); 1.68 (1); 50.5 (1); 1.68 (2) 10 000 (5 mm); 1.68 (0.7); 5.05 (0.7); 16.8 (0.7); 50.5 (0.7); 168 (0.7); 1.68 (2)
U1520C27R2	V: volcanics	67% phyllosilicates, 16% calcite	897.5	AE018	intact	8.0	10 000 (5 mm); 1.68 (1); 50.5 (1); 1.68 (2)
U1520C37R1	V: volcanics	59% phyllosilicates, 7% Mg-rich calcite, 5% plagioclase	977.8	AE027	intact	8.8	10 000 (5 mm); 1.68 (1); 50.5 (1); 1.68 (2)
U1520C38R2	V: volcanics	53% calcite, 28% phyllosilicates, 6% clinoptilolite, 5% amphibole	988.4	AE053 AE068	intact powder	8.9 10.0	10 000 (5 mm); 1.68 (1); 50.5 (1); 1.68 (2) 10 000 (5 mm); 1.68 (0.7); 5.05 (0.7); 16.8 (0.7); 50.5 (0.7); 168 (0.7); 1.68 (2)
U1520C41RCC	VI: blue volcanics	56% phyllosilicates, 14% amorphous, 8% calcite, 5% iron oxides	1019.7	AE044	intact	9.2	10 000 (5 mm); 1.68 (1); 50.5 (1); 1.68 (2)
U1520C43R2cyl_10/13	VI: black mudstone	50% clinoptilolite, 19% phyllosilicates, 16% plagioclase	1036.5	AE038	intact	9.4	10 000 (5 mm); 1.68 (1); 50.5 (1); 1.68 (2)

In which  $\mu_0$  is the friction coefficient at a reference sliding velocity  $V_0$ ,  $a$ ,  $b_1$  and  $b_2$  are dimensionless parameters that scale the direct ( $a$ ) and evolution ( $b_{1,2}$ ) effects observed after a velocity change, and  $D_{c1}$  and  $D_{c2}$  are characteristic sliding distances in meter (Fig. 4.3).  $\theta_{1,2}$  are the state variables that describe the evolution of the contact in units of time. In most cases, the data is well-described by a single state variable, so that  $b_2 = 0$  and  $D_{c1} = D_{c2}$ . We obtain a best-fit model to our experimental data by inverse modelling techniques, using a Matlab script RSFit3000 (Skarbek and Savage, 2019).

Equation 3 is called the slowness or Dieterich law, which describes the evolution of the contact over time. At steady state  $d\theta/dt = 0$  and equation 4.2 reduces to:

$$a - b = \frac{\Delta\mu_{ss}}{\Delta \ln(V)} \quad (4.4)$$

in which  $\Delta\mu_{ss}$  is the difference in steady state friction coefficient  $\mu$  at the sliding velocities  $V$  before and after the velocity step and  $b = b_1 + b_2$ . This resulting  $(a-b)$  is important in evaluating the stability of a fault, since positive  $(a-b)$  means friction increases with increasing velocity (velocity-strengthening behavior), which generally leads to stable sliding, whereas negative  $(a-b)$  or velocity-weakening behavior is one of the prerequisites for slip instabilities, including SSEs. Whether or not velocity-weakening behavior leads to unstable sliding, depends on the stiffness of the sample  $k_c$  compared to the stiffness of the surroundings  $k$ , which during experiments is the machine stiffness (Cook, 1981; Ruina, 1983):

$$k < k_c = \frac{(b-a)\sigma'_n}{D_c} \quad (4.5)$$

In which  $b=b_1 + b_2$  and we assume  $D_c=D_{c1}$  from equation 4.2. This criterion can only be satisfied when  $(b-a)$  is positive, meaning that instabilities can only occur in velocity-weakening materials. Periodic oscillations in friction are predicted to occur when  $k \approx k_c$  or  $k/k_c \approx 1$  (Ruina, 1983; Gu et al., 1984), which can be recreated in the laboratory (Baumberger et al., 1994, 1999; Leeman et al., 2016, 2018), and are thought to be the laboratory equivalent of SSEs.

Equation 4.5 shows that the critical stiffness  $k_c$  is dependent on effective normal stress  $\sigma'_n$ , however the influence of effective normal stress on machine stiffness  $k$  should also be considered. We measured this by subjecting a steel blank in the sample cell to shear loading and unloading cycles with and found the unloading stress to linear increase from 5.3 MPa/mm at 2 MPa normal stress to 9.4 MPa/mm at 10 MPa normal stress.

#### 4.5.1 Slow Slip Event analysis

During sliding at constant driving velocity, several experiments show repetitive or irregular stress drop events. These shear stress drops are interpreted as laboratory SSEs only when they coincide with a clear observable decrease of sample velocity below the load point velocity during the loading phase where shear stress increases, followed by a clear peak in sample velocity during the subsequent stress drop. We apply the criterion that peak velocity during stress drop must be at least 3 times the minimum velocity measured during the loading phase. This number is based on the noise in our velocity data, which is calculated from the sample displacement, at times when no slip events occur. All stress drops were analyzed systematically and for those that fulfill our criteria to be SSEs, we calculate stress drop as the difference between peak shear stress and minimum shear stress after the event, the event slip as the sample displacement during the stress drop and stiffness during the stress drop by fitting a linear best-fit through the stress drop part of the stress-sample displacement curve. We differentiate between slip duration as time during stress drop and total duration as the time from when the shear stress starts to increase to the end of the stress drop. The recurrence interval, is the time from peak stress of the event before to the peak stress of the slip event. Minimum sliding velocities are the lowest velocity measured during the loading phase of the SSE, the peak slip velocity is the highest velocity measured during the slip phase.

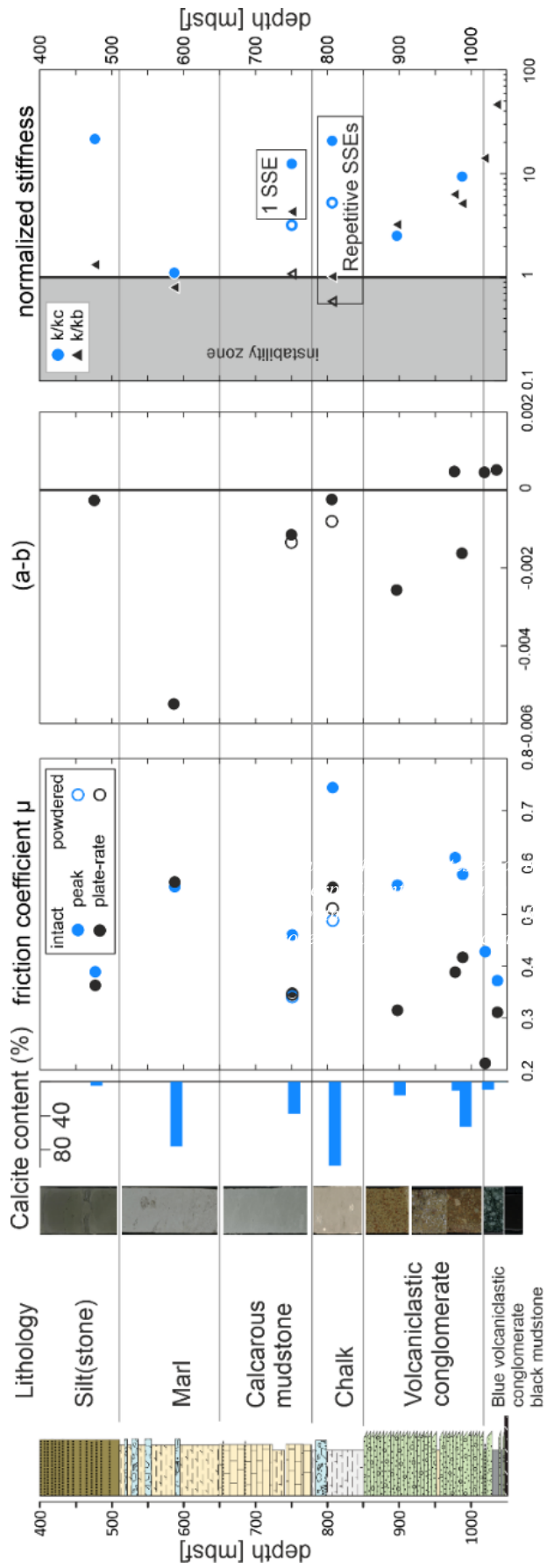


Figure 4.4 Samples tested at in-situ normal stress: the three graphs show friction coefficient  $\mu$  at peak value, end of the run-in (steady-state) and end of the experiment (plate-rate) as defined in Figure 3; frictional stability parameter (a-b) for the three velocity steps; and normalized stiffness calculated from the velocity upstep of 1.68 to 50.5 mm/s (plate-rate to SSE-rate). Open symbols represent the powdered equivalent of the intact samples. Note: the core photos and calcite content (3<sup>rd</sup> and 4<sup>th</sup> column) are specific for the sample tested, and not necessarily representative for the entire interval.

## 4.6 Results

### 4.6.1 Frictional behavior

The friction coefficients at in-situ normal stresses (Fig. 4.4) show no clear trend with depth, but rather with lithology. The calcite-rich chalk (99%) and marl (76%) are relatively strong with a residual friction coefficient ( $\mu_r$ )  $>0.5$ , whereas the lowermost lithologies, a blue volcanoclastic conglomerate and a black mudstone are the weakest with  $\mu_r$  of 0.25 and 0.27. The volcanoclastic conglomerates as well as the clay-rich calcareous mudstone and siltstone have  $\mu_r \approx 0.4$ . The differences between the friction coefficients at 10  $\mu\text{m/s}$  ( $\mu_r$ ) and at the plate-rate of 1.7  $\text{nm/s}$  shown in figure 4 ( $\mu_{pr}$ ) are  $<0.05$ . Other than lower peak friction coefficients during initial run-in, the powdered equivalents of the SSE-showing samples tested at in-situ normal stress show similar friction coefficients as their intact counterparts. The standardized experiments at 10 MPa normal stress show similar trends as the intact samples (Fig. 5A). The calcite-rich lithologies show higher friction coefficients ( $\mu_r > 0.55$ ) than the volcanoclastic conglomerate ( $\mu_r = 0.31$ ), calcareous mudstone ( $\mu_r = 0.28$ ) and siltstone ( $\mu_r = 0.34$ ). The friction coefficients during the second phase of sliding at plate-rate are close to the initial plate-rate sliding phase, indicating that for most samples the displacement effect is small, except for the siltstone, which weakens with displacement.

The friction rate parameter  $a-b$  also does not show a trend with depth, but important observations for the in-situ experiments are that the lowermost, weakest lithologies are velocity-strengthening ( $a-b \approx 0.0005$ ), whereas most of the other lithologies are velocity-weakening (Fig. 4.4). Figure 4.5A shows that during the standardized experiments, the marl shows constant negative  $a-b$  values of  $\sim -0.004$ . The chalk has  $a-b$  values decreasing from slightly positive ( $<0.001$ ) at low velocities to negative at 51  $\text{nm/s}$  ( $-0.002$ ) and 168  $\text{nm/s}$  ( $-0.003$ ). All other lithologies show a mix of positive and negative values, mostly around 0.

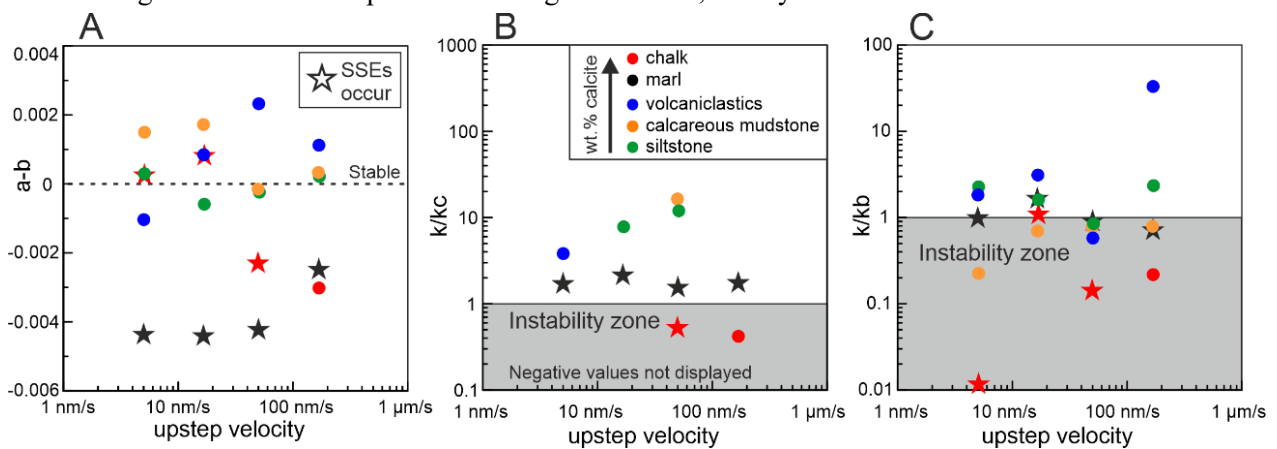


Figure 4.5: Samples tested at 10 MPa, driving velocities during which SSEs occur are highlighted with a star, A: stability parameter  $a-b$ . B: normalized stiffness  $k/kc$ , where negative values that occur when  $(a-b)$  is positive are not displayed on a logarithmic scale and C: normalized stiffness  $k/kb$

#### 4.6.2 Slow slip events

In total, 5 experiments showed SSEs. These include two intact samples at in-situ normal stress, the calcareous mudstone and the chalk. The chalk also showed SSEs during the experiment at in-situ normal stress with a powdered equivalent of the intact sample. At the standardized normal stress, also two lithologies show SSEs, the chalk, which also had SSEs at in-situ normal stress, and the marl, which showed stable sliding at in-situ normal stress. This shows the necessity of the ‘standardized’ tests, as the tendency for slip instabilities increases with effective normal stress, due to effects the effective normal stress has on both the critical sample stiffness and machine stiffness (see methods). When SSEs occur, this happens during the first and second phase of sliding at plate-rate velocity (1.7 nm/s), but in some of the experiments there are differences in stress drop, duration and velocity between the first and last phase of plate-rate sliding. Additionally, the standardized experiments also show SSEs at higher sliding velocities than plate-rate. A complete overview of all events at plate-rate sliding velocity is given in .

Out of the nine intact samples tested, only the calcareous mudstone and the chalk showed spontaneous laboratory SSEs, which occurred only while driving at plate-rate sliding velocities. In the calcareous mudstone (751 mbsf), one event occurred during otherwise steady-state sliding (Fig. 4.6A). In a period of ~8 hours, the shear stress increased from ~2.36 MPa to ~2.41 MPa and simultaneously the sample velocity decreased to about 0.5 nm/s, significantly below the driving velocity of 1.7 nm/s. This was followed by a plateau phase of ~10 hours where the shear stress remains high, after which there is a sudden drop in shear stress of ~49 kPa in ~55 minutes, while the sample velocity spikes up to 4.2 nm/s. After this single SSE, steady-state sliding is resumed at a similar shear stress as before the event, which continues for the remainder of the experiment.

The intact chalk (807 mbsf) shows irregular shear stress drops towards the end of the first plate-rate sliding phase, of which 4 coincide with a velocity increase large enough to qualify as SSEs. When the driving velocity is increased to SSE-velocity (50.5 nm/s), stable sliding occurs. When the driving velocity is decreased to plate-rate again, repetitive SSEs start within 0.2 mm of displacement. The SSEs occurring during this experiment are symmetric loading/unloading

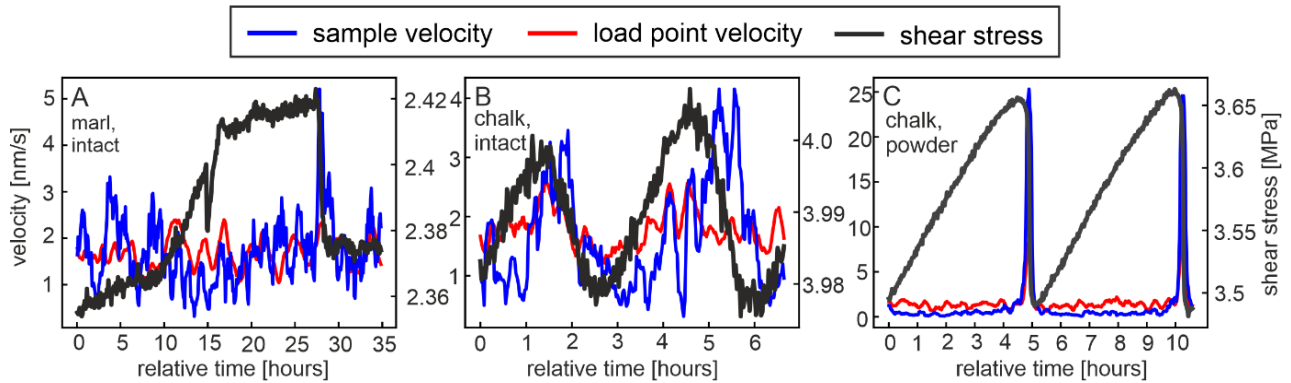


Figure 4.6: Examples of slow slip events at in-situ normal stress, A: single event in the intact lower calcareous mudstone AE002 (the shear stress drop at 15 hours is a machine effect). B: relatively sinusoidal SSE-cycles in the intact chalk sample AE011. C: asymmetrical SSEs with high maximum velocities in the powdered chalk sample AE034.

cycles (Fig. 4.6B), that have slip durations of  $\sim 1$  hour. The stress drops are 9-30 kPa, with an average minimum velocity during the loading of 0.61 nm/s, and an average peak slip velocity of 3.3 nm/s over the 65 events measured (Table 4.2).

Experiments on the powdered equivalents of two intact samples that showed SSEs resulted in stable sliding for the entire experiment on the calcareous mudstone. The powdered equivalent of the chalk shows SSEs that start within 0.2 mm of displacement after the driving velocity was decreased to the plate-rate value, disappear when the sliding velocity is increased to SSE-rate and reappear immediately after the sliding velocity is decreased to the plate-rate driving velocity for the second time. Compared to the intact sample, the SSEs during the powdered experiment have higher stress drops of 126-197 kPa, the event cycles are asymmetrical, with loading phases of  $\sim 5$  hours that are significantly longer than the unloading phases of up to 50 minutes (Fig. 4.6C). The minimum velocity during loading is 0.18 nm/s on average, with a measured average peak slip velocity of 20 nm/s, for a total of 56 events. The differences between the events during the first and the second phase of plate-rate sliding are minor (Table 4.2).

During the “standardized” experiments with powdered samples at a consistent normal stress of 10 MPa, two samples show SSEs. These are the chalk (807 mbsf), that also showed SSEs in the intact and the powdered sample at an in-situ normal stress of 7.1 MPa; and the marl (588 mbsf), which did not show SSEs under an in-situ normal stress of 4.9 MPa (Fig. 4.7). The chalk shows clear SSEs during the first phase of sliding at plate-rate (1.7 nm/s), with durations of 104 minutes and maximum slip velocities of 3.2 nm/s. The SSEs continue when the sliding velocity is increased to 5.1, 17 and 51 nm/s, with stress drops constant around  $\sim 20$  kPa (Fig. 4.8A) and maximum sliding velocities  $\sim 2x$  the driving velocity (Fig. 4.8B). When the driving velocity is increased to 170 nm/s, the number of smaller stress drops without significant velocity peaks increases (Fig. 4.7B), but no stress drop coincides with a significant increase in velocity, to qualify

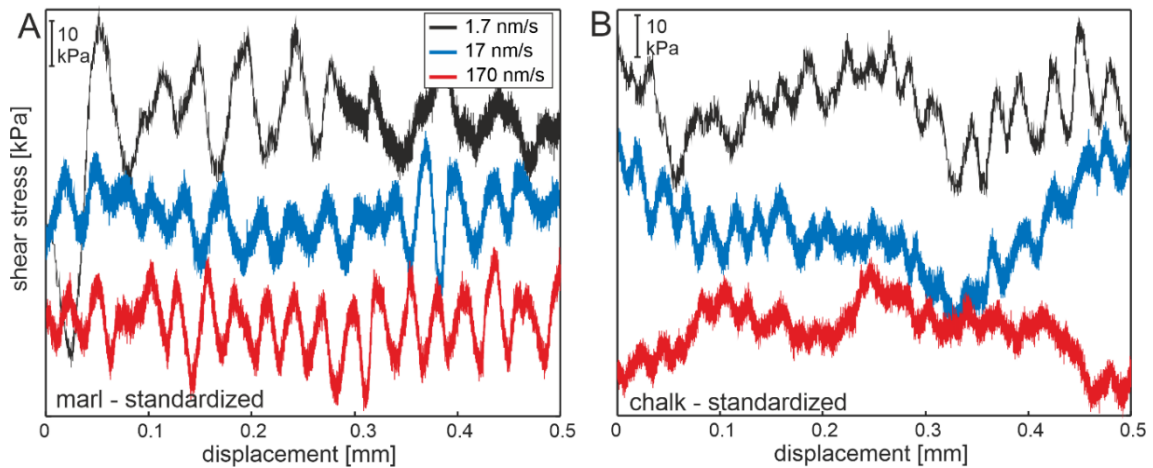


Figure 4.7: Shear stress with displacement for the two samples that show SSEs at 10 MPa normal stress at the last 0.5 mm before the next velocity step. A: Marl sample AE060 shows clear SSEs at all velocities. B: Chalk sample AE062 has small stress drops at the highest velocity, which are not clear SSEs.

as a SSE based on our definition. SSEs reappear during the second plate-rate sliding phase, where events are asymmetrical in loading/unloading phase (Fig. 4.8C). Compared to the SSEs during the first plate-rate sliding phase, the SSEs during the second plate-rate sliding phase (open symbols) have larger stress drops of 113 kPa (Fig. 4.8A), shorter durations of 40 minutes and higher slip velocities of 14.7 nm/s (Fig 4.8B). The SSEs during the first plate-rate step resemble the events observed in the intact sample at in-situ normal stress both in the symmetrical shape and in statistics (Fig. 4.6B+4.8), whereas the SSEs observed during the second plate-rate step are more comparable to those seen during the powdered experiment at in-situ normal stress (Fig 4.6C, Table 4.2).

The test with marl at standardized conditions shows SSEs at all driving velocities. With increasing driving velocity, the events decrease in terms of stress drop from 37 to 18 kPa (Fig. 4.8A), and maximum slip velocities are  $\sim 2$  times the driving velocity (Fig. 4.8B). Similar as in the standardized chalk experiment, the largest SSEs occur during the second plate-rate sliding step, where the events are asymmetrical (Fig. 4.8C) with higher stress drops of 312 kPa and maximum slip velocities over  $2 \mu\text{m/s}$  that are only resolved in two events were the sampling rate was significantly increased (table 4.2).

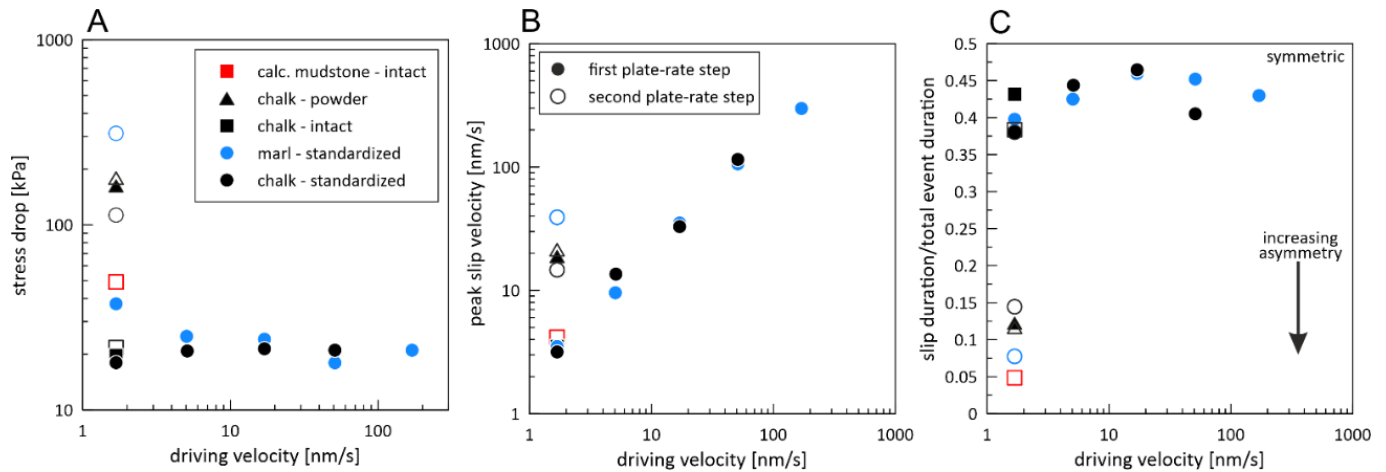


Figure 4.8: characteristics for the standardized experiments compared to other experiments that showed SSEs. A: Stress drop. B: maximum slip velocity normalized to driving velocity. Inset shows close-up of lower values. C: slip duration/total event duration is a measure how symmetric or sinusoidal events are, the not-sinusoidal events with low slip/total duration are the ones not following the same trends in A and B.

## 4.7 Discussion

### 4.7.1 Calcite content

The frictional behavior of the samples, is controlled mostly by lithology, not depth, where we observe samples with a higher calcite content have a higher friction coefficient and lower values for  $a-b$ . That the frictional strength of calcite-rich lithologies is higher than for example phyllosilicate rich samples, has been previously shown. Ruggieri et al. (2021) show the friction coefficient decreases from 0.65 to 0.37 for a sample composition changing from limestone to shale, at normal stress of 30-100 MPa. Verberne et al. (2015) show for samples with a calcite content of  $\sim 98\%$  at room temperature and 50 MPa normal stress, a steady-state friction coefficient at 1  $\mu\text{m/s}$  sliding velocity of 0.56 to 0.66. The friction coefficient we measure for the chalk, which consists of 99% calcite, has values ranging from 0.48-0.58 for 10  $\mu\text{m/s}$  and 1.7 nm/s at in-situ and 10 MPa effective normal stress. At room temperature, both Ruggieri et al. (2021) and Verberne et al. (2015) report velocity-strengthening behavior, although for the lower effective normal stress 30 MPa, there seems to be a transition to velocity-neutral behavior in the work of Verberne et al. (2015). Ruggieri et al. (2021) show for  $a-b$  decreases for velocities below 1  $\mu\text{m/s}$  for wet limestone. The other main component of our samples are phyllosilicates (Table 4.1), which are reported to be weaker than calcite. Three phyllosilicates common in subduction zones and in our samples, smectite, illite and montmorillonite have friction coefficients of about 0.3, 0.6 and 0.1 (Logan and Rauenzahn, 1987; Saffer and Marone, 2003). Velocity-dependent frictional behavior

is mostly velocity strengthening (montmorillonite, illite), but can be slightly velocity-weakening for smectite at low normal stress and sliding velocity (Saffer and Marone, 2003). All of this fits with the frictional strength and velocity dependent behavior we observe for the lithologies tested.

When focusing on the lithological control on which samples show spontaneous laboratory slow slip events, the occurrence of SSEs correlates with the calcite content of the samples. The chalk sample, which showed SSEs under all testing conditions, has a calcite content of 99% (Table 4.1). The marl, with the second-highest amount of calcite (76%), also showed SSEs at 10 MPa. The low in-situ normal stress of the marl (4.9 MPa) compared to the chalk (7.1 MPa) may be the reason why there were no SSEs at in-situ normal stress testing conditions, because the critical stiffness depends on effective normal stress. The intact calcareous mudstone sample that showed a single SSE contains an intermediate level of calcite of 38%, which also fits in this trend. This indicates that SSEs occur preferentially in the calcite-rich materials. To understand why calcite-rich lithologies are needed to initiate SSEs and to make predictions under what conditions they can initiate and propagate, we investigate the mechanisms that drive SSEs.

#### 4.7.1 SSE occurrence

As explained in the methods, the empirical rate- and state friction theory predicts periodic oscillations in friction, or laboratory SSEs, to occur when the faults critical stiffness  $k_c$  equals the machine stiffness  $k$ , or  $k/k_c \approx 1$ , with a transition to rapid stick-slip when  $k/k_c < 1$ . The experiments that showed SSEs, have  $k/k_c > 1$ , up to 21 for the intact chalk, only the chalk has  $k/k_c < 1$  for driving velocities  $> 51$  nm/s, although SSEs disappear at the highest driving velocity and occur when the material is velocity-strengthening and  $k/k_c$  is negative (Fig. 4.5). This simple criterion therefore seems insufficient to explain our results.

It has been suggested that SSEs are not full instabilities, but rather instances of accelerated slip that nucleate similar to ordinary earthquakes, but do not reach the critical size needed to develop into full dynamic instabilities and therefore these instabilities remain slow (Dieterich, 1992; Rubin, 2008; Ikari, 2019). The criterion that describes when this type of events may nucleate is:

$$k < k_b = \frac{b\sigma'_n}{D_c} + \frac{\dot{\tau}}{d} \quad (4.6)$$

Table 4.2 List of observed slow slip events statistics at plate-rate sliding \*) some sliding events, with data in brackets, were logged at higher sampling rate, revealing events are so fast that standard sampling rate underestimates peak velocity

Sample	Test type	$\sigma_0$ [MPa]	# of SSEs	Stress drop [kPa]	Duration [min]	Total slip [ $\mu\text{m}$ ]	Peak slip velocity		$k_{\text{trap}}$ [MPa/mm]
							[mm/s]	[cm/y]	
calc. mudstone	Intact	6.5	1	49.1	55	17.7	4.2	13.2	3.0
chalk	1 <sup>st</sup> step	7.1	3	19.7 $\pm$ 2.6	99.9 $\pm$ 13.1	13.3 $\pm$ 2.8	3.5 $\pm$ 0.5	11.1 $\pm$ 1.5	1.1 $\pm$ 0.2
	2 <sup>nd</sup> step	7.1	62	21.7 $\pm$ 5.7	82.9 $\pm$ 17.5	10.5 $\pm$ 2.9	3.3 $\pm$ 0.7	10.5 $\pm$ 2.1	2.1 $\pm$ 1.1
chalk	1 <sup>st</sup> step (*)	7.1	25 (1)	162.4 $\pm$ 15.8	41 $\pm$ 7	22.2 $\pm$ 2.8	18.8 $\pm$ 3.6 (63.5)	59.4 $\pm$ 11.5 (200.3)	8.1 $\pm$ 1.3
	2 <sup>nd</sup> step	7.1	31	179.1 $\pm$ 11.0	35 $\pm$ 4	22.9 $\pm$ 3.0	21.4 $\pm$ 3.1	67.6 $\pm$ 9.9	8.5 $\pm$ 1.2
Marl	1 <sup>st</sup> step	10	6	37.4 $\pm$ 6.4	184 $\pm$ 64	22.8 $\pm$ 4.9	3.5 $\pm$ 1.0	11.1 $\pm$ 3.1	1.6 $\pm$ 0.2
	2 <sup>nd</sup> step (*)	10	27 (2)	312 $\pm$ 19	40 $\pm$ 6	41.7 $\pm$ 4.1	39.2 $\pm$ 4.0 (2276)	123.5 $\pm$ 12.7 (7177)	7.8 $\pm$ 0.6
chalk	1 <sup>st</sup> step	10	8	18.0 $\pm$ 4.7	104 $\pm$ 19	12.4 $\pm$ 3.1	3.2 $\pm$ 0.6	10.0 $\pm$ 1.8	1.2 $\pm$ 0.3
	2 <sup>nd</sup> step	10	40	113 $\pm$ 10	39 $\pm$ 7	17.0 $\pm$ 2.5	14.7 $\pm$ 2.4	46.2 $\pm$ 7.5	7.6 $\pm$ 1.3

In which the second term may be neglected (Dieterich, 1992). This criterion is only valid for spring-slider systems that are far above steady state ( $V \gg D_c/\theta$ ), which can be achieved at high velocity or at low velocity when  $\theta$  is high. Since in this stiffness criterion parameter  $b$  appears instead of  $b-a$ , these slow instabilities are not limited to velocity-weakening faults (Dieterich, 1992). The SSEs we observe in the velocity-strengthening chalk at standardized conditions occur when  $k/k_b < 1$ , and therefore can be explained by this criterion. Also the SSEs in the standardized marl and chalk under in-situ conditions have  $k/k_b < 1$ , meaning we tend to observe laboratory SSEs when  $k_c < k < k_b$ , except for the single event in the intact marl which has  $k/k_b \gg 1$ . The intact calcareous mudstone however also satisfies this criterion, but did not show SSEs. Therefore, although this criterion does explain most of the occurrence of most SSEs, the usefulness to predict SSEs is limited, because single events may occur when the criteria are not met and sliding may be stable even when the criteria are met.

Another mechanism that has been used to explain the occurrence of slow slip events is that there is a specific cut-off velocity, because mixtures of common materials in subduction zones can be velocity-weakening at low sliding velocities and velocity-strengthening for increasing sliding velocity (Saffer and Wallace, 2015). Shibasaki et al. (2019) show the SSEs at the Hikurangi margin can be explained by this mechanism, using a cut-off velocity of  $\sim 1 \mu\text{m/s}$ , as found in experiments on a calcareous mudstone from the Hikurangi margin (Rabinowitz et al., 2018). Our data does not show a trend in  $a-b$  with velocity (Fig. 4.5A) and no transition from velocity-weakening to velocity-strengthening behavior, but the driving rates we use ( $< 170 \text{ nm/s}$ ) and at which we observe SSEs are also below the cut-off velocity found by Rabinowitz et al. (2018). That we observe SSEs only at plate-rate driving velocities for in-situ normal stress and the absence of SSEs at the highest driving velocity of  $170 \text{ nm/s}$  in the chalk, could be explained by a cut-off velocity. Without measurements of the frictional behavior at higher driving velocities that show a transition to velocity-strengthening behavior, our data does not indicate a cut-off velocity a present.

There are more mechanisms that have been proposed to explain SSEs, such as the mixing of velocity-weakening and velocity-strengthening materials (Skarbek et al., 2012), but we see SSEs can also occur in a chalk of 99% calcite. Also the interaction of multiple fault strands (Romanet et al., 2018) cannot explain our results as our set-up forces localization of the fault plane to a thin zone. We have no indications that external stress perturbations (Perfettini and Ampuero, 2008), high fluid pressures (Liu and Rice, 2007) or significant slip-weakening (Ikari et al., 2013), which have been used to explain the occurrence of slow slip events, occur

during our experiments. The only systematic correlation we see between the experiments that show SSEs, is the high calcite content.

#### 4.7.2 Earthquake relationships

When we compare all SSEs that occurred when the driving velocity was set to 1.7 nm/s, we observe that the lower the velocity during the inter-SSE period, the higher the maximum slip velocity during the SSE (Figure 4.9A), a trend previously observed by Ikari (2019), which is interpreted as that SSEs do not require full locking in between events, but stronger locking leads to larger events, which is also true for our data (Figure 4.9B). Stronger locking results in better healed fault surfaces, meaning the fault can support higher shear stresses before it slips, which causes larger stress drops (Figure 4.9C). This relationship we found is similar to trends observed by Johnson and Scholz (1976) and Okubo and Dieterich (1984), who both find a linear increase in stress drop with particle or average slip velocity.

In subduction zones, SSEs occur in the transition zones of partial locking, on the updip and downdip end of the locked, seismogenic zone (Obara and Kato, 2016), which has also been shown for the Hikurangi margin (Wallace and Beavan, 2010). The degree of locking is quantified by the coupling coefficient  $\phi$ , calculated from the short term local velocity, in our experiments  $V_{sample}$ , over the long term far-field velocity, or load-point velocity  $V_{lp}$  in the experiments, as  $\phi = 1 - (V_{sample}/V_{lp})$  (Wallace et al., 2009). At stable sliding  $V_{sample}$  and  $V_{lp}$  are equal and therefore the coupling coefficient is 0, whereas full locking or a sample velocity of zero gives a coupling coefficient of 1. Our results show that the slow slip events have non-zero inter-SSE sliding velocities and therefore do not become completely locked in between sliding events. As an example, the intact chalk sample (AE11) on average has inter-SSE sliding velocities  $\sim 0.6$  nm/s, which with a driving velocity of 1.7 nm/s would give a ‘coupling coefficient’ of  $\sim 0.64$ . When the inter-SSEs velocities decrease, the coupling coefficient increases and the events become faster and larger and start to approach ordinary earthquakes (Fig. 4.9A).

From natural earthquakes we know that seismic moment increases with recurrence interval when comparing faults of constant length (Kanamori and Allen, 1986) or for identical earthquakes (Vidale et al., 1994), which both studies say is most likely caused by an increase in stress drop. Our data confirms this, we see stress drop increases with increasing event duration (Fig. 4.9D), although there seems to be a difference between the relatively slow, sinusoidal events that commonly occur during the first velocity step (closed symbols in Figure 4.9) and the larger, faster events that generally occur during the second plate-rate velocity step (open symbols in Figure

4.9). Marone *et al.* (1995) show for two aftershocks sequences on a natural fault, the increase in stress drops with recurrence interval fits with laboratory measured healing rates for longer contact times.

That the SSEs we observe are linked to partial locking and inter-SSE healing explains why we observe the SSEs in the calcite-rich materials. Healing rates are material dependent and higher for calcite-rich material than for clay-rich materials under the conditions of our tests (Carpenter *et al.*, 2016; Ruggieri *et al.*, 2021). This does not mean SSEs in general are limited to calcite-rich material, the SSEs in the Cascadia subduction zone have for example been linked to silica content by Audet and Bürgmann (2014), who explain the occurrence of slip events by pore pressure buildups due to a healing-induced permeability reduction.

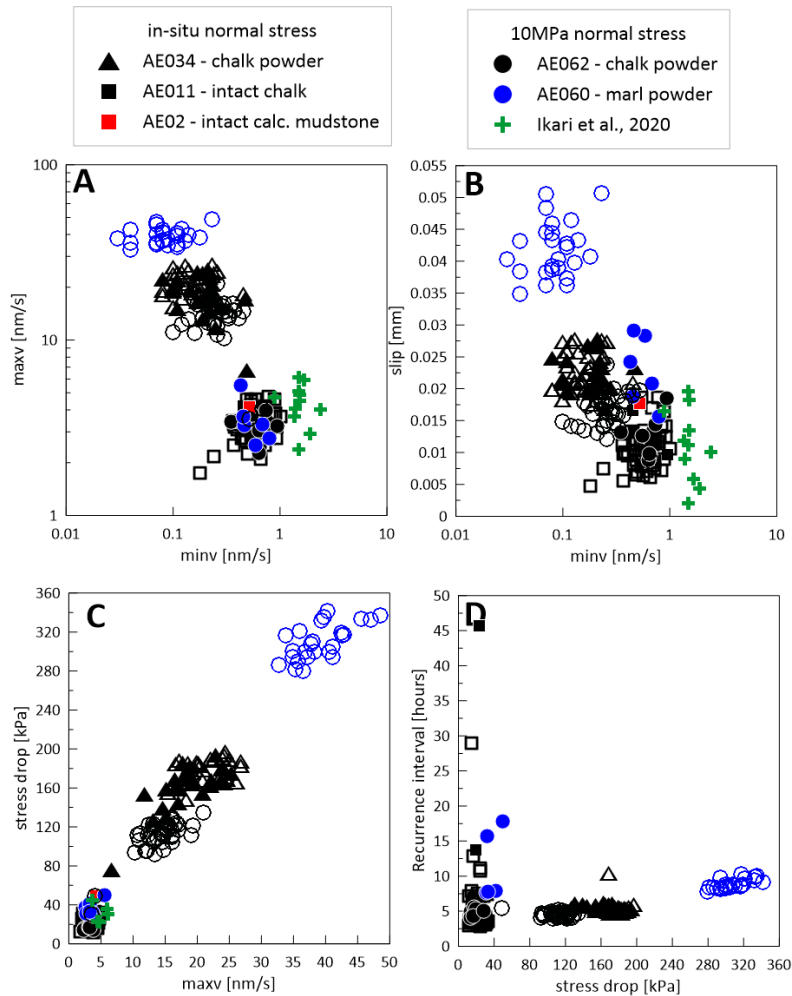


Figure 4.9 Characteristics of SSEs with maximum slip velocity. A: maximum slip velocity increases when interstitial velocities decrease. B: lower minimum slip velocities cause events with higher stress drops. C: stress drop increases with maximum slip velocity. D: Higher stress drops occur when recurrence interval increases. Included are all SSEs from different lithologies, but only at driving velocity of 1.7 nm/s, from (Ikari *et al.*, 2020) only experiments at 10 MPa normal stress are included. Open symbols are 2<sup>nd</sup> plate-rate step.

### 4.7.3 Hikurangi Margin

Our results clearly indicate the pelagic unit (510 – 848 mbsf), that consists of the marl, calcareous mudstone and chalk is the most likely origin of SSEs in the Hikurangi margin. This seems to be contradicted by the fact that these are among the strongest samples tested, whereas deformation typically localizes in the weakest layers. The two weakest samples we tested, a black mudstone and blue volcanoclastic conglomerate, are from the lowermost unit that consists of a mix of lithologies (Barnes et al., 2019) (Fig. 4.4), which suggests that the plate boundary fault or décollement should be most likely to form in this lowermost unit. This raises the problem that either the décollement does not form in the weakest layer, or the SSEs do not originate on the décollement.

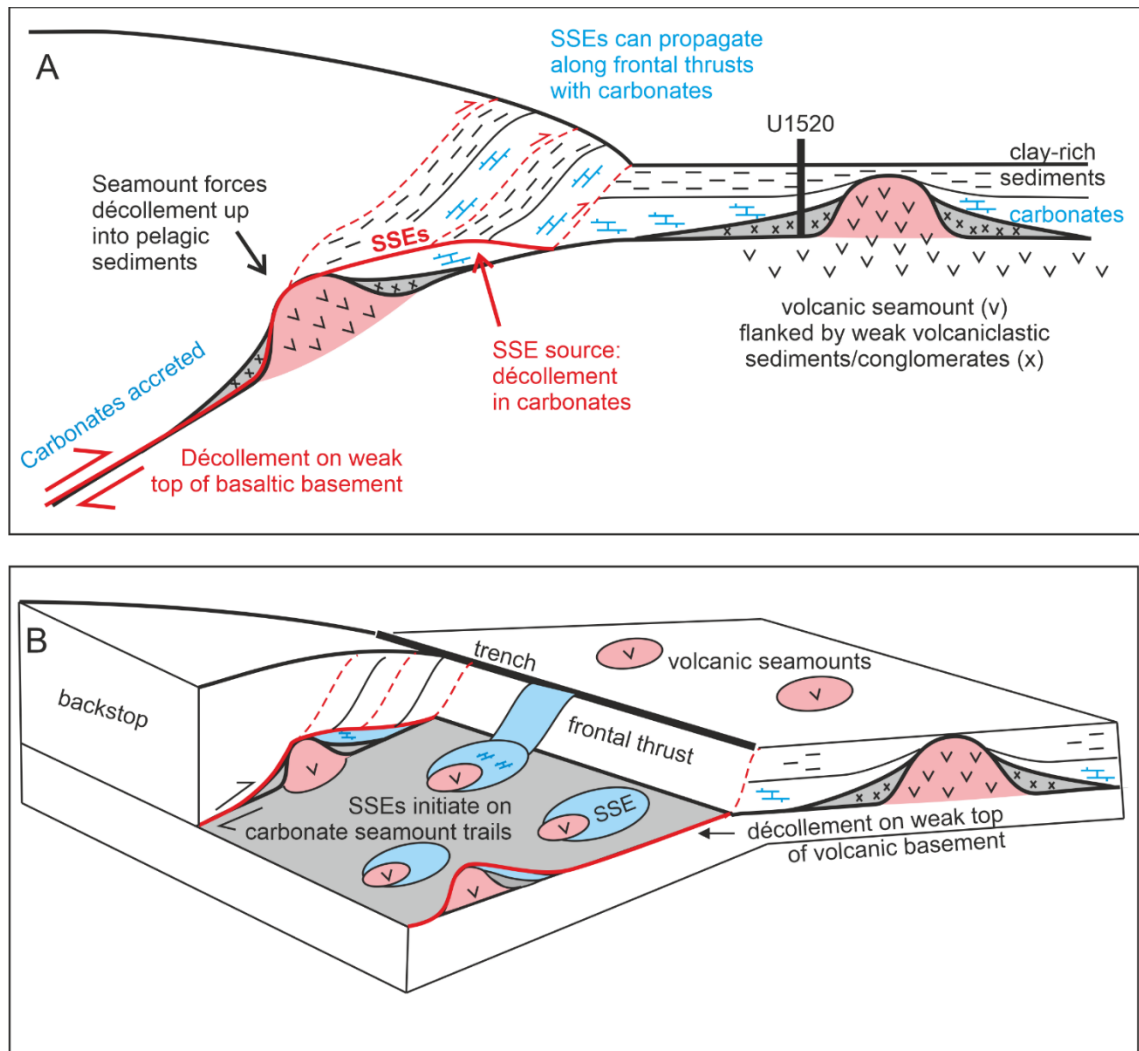


Figure 4.10 conceptual model of seamount subduction. A: 2D model based on the seismic profile 05CM-04 as interpreted by Barnes et al. (2020) (Fig. 1B), showing the main concept: the décollement will form in the weak thin layer of mixed lithologies directly overlying the basaltic basement, but the strong seamount forces the décollement up in the calcite-rich pelagic sediments. Calcite-rich layers are present along the frontal thrusts, where SSEs may

*propagate B: 3D model showing the patchy distribution of carbonate sediments trails behind subducted seamounts on the megathrust fault, that otherwise follows the weak top of the volcanic basement.*

Our data shows that the initiation of SSEs requires the calcite-rich unit to be present in the plate-boundary fault zone. We propose this is caused by numerous seamounts that are present on the incoming and at depth in the Hikurangi subduction zone (Lewis et al., 1998; Bell et al., 2010; Barnes et al., 2020). The dense, intact volcanic rock of the incoming seamount is difficult to break and therefore forces the surrounding sedimentary rocks to break. The seamounts penetrate the pelagic layer entirely or partially and are surrounded by the pelagic sediments, which means the volcanic rocks are in direct contact with the pelagic sediments (Barnes et al., 2020). Interpretation of seismic profiles by Bell *et al.* (2010) suggest that a trail of sediments up to 2-4 km thick may follow a subducted seamount and since the seamounts are surrounded by the pelagic sediments, it is likely that this trail of sediments include carbonates. The seamount forcing the décollement up into the pelagic sediments, illustrated in Figure 4.10 would explain various of the observations. It explains how the pelagic sediments can be present at the plate boundary fault, which is required for the initiation of SSEs, while at the same time a large part of the pelagic unit is accreted into the accretionary wedge, which is visible from the seismic sections, but also a requirement for the SSEs to propagate to shallow depths, as observed. It also explains why the shallow SSEs at the Hikurangi margin occur at locations where numerous seamounts are subducted, whereas south of Cape Turnagain where there are less seamounts only one small SSE has been observed since 2009 (Wallace, 2020), even though we show the frictional behavior of the volcanic lithologies indicates they are not likely to host unstable events and slow slip is limited directly on top of subducted seamounts (Barker et al., 2018).

This mechanism builds on the mechanism to explain the SSEs at the Hikurangi margin by Barnes *et al.* (2020), who suggested the geometrical complexity of subduction seamounts leads to a wide deformation zone in which various lithologies are entrained, with a heterogeneous distribution that explains the patchy nature of slow earthquakes. Our results indicate it is specifically the calcite-rich lithologies that have to be present in the deformation zone. Seamounts have also been proposed to act as asperities that cause normal stress heterogeneities to explain earthquake or slow slip occurrence (Lay et al., 1982; Wang and Bilek, 2014). Also high fluid pressures, possibly caused by subducting seamounts (Sun et al., 2020) have been proposed to drive SSEs by causing very low effective normal stresses (Saffer and Wallace, 2015). These physical mechanisms may coexist with what we propose, but SSEs will only occur in lithologies that are potentially unstable. When focusing on the lithological controls on the Hikurangi shallow SSEs, the spontaneous laboratory SSEs we observe in the carbonate-rich layers show that

introduction of the pelagic sediments into the plate-boundary fault zone suffices to explain the occurrence of these SSEs.

## 4.8 Conclusion

Using laboratory experiments, we describe the frictional behavior at plate-rate sliding velocities of the sedimentary sequence going into the Hikurangi subduction zone, from IODP site U1520. The calcite-rich pelagic unit (510 – 848 mbsf), consisting of chalk, marl and calcareous mudstone showed stress drop events that are the laboratory equivalent of SSEs at either all (chalk) or some (marl and calcareous mudstone) of the tested conditions. This unit is therefore the most likely candidate to host the shallow slow slip events observed at the Hikurangi margin. The calcite-rich lithologies show partial locking in between slip events, where with lower inter-SSE sliding velocities the events become faster and stress drops increase so that the events start to approach ordinary earthquakes. The generation of slow slip events at the Hikurangi subduction margin requires the calcite-rich pelagic unit to be present in the deformation zone, although these lithologies are frictionally strong and therefore unlikely to form the décollement. We propose the introduction of these sediments to the plate-boundary deformation zone can occur due to the presence of numerous seamounts that cause heterogeneity of the subduction interface.

## 5 Synopsis

### 5.1 Introduction

In this thesis, I have explored the effects three variables have on the frictional behavior and stability of faults, in an overall effort to explain why some natural faults host destructive ordinary earthquakes, whereas others may be more prone to slow slip events or stable sliding. Specifically, I describe frictional behavior by (1) the friction coefficient  $\mu$ , which represents the shear strength of a surface, normalized by the normal stress and is important because faults normally develop in the weakest layer, where  $\mu$  is the lowest. And (2) frictional stability parameter  $a-b$ , which is a measure for the velocity-dependence of friction. Normally velocity-weakening behavior, or a negative  $a-b$ , is one of the requirements for unstable slip whereas velocity-strengthening behavior or positive  $a-b$  will lead to stably sliding faults. Additionally, we consider the occurrence of slip instabilities, independent of whether this is predicted by the frictional behavior.

Here, I summarize the main findings and answer the research questions, starting with how fault surface roughness and fault-normal stiffness influence the sliding behavior in the laboratory and how laboratory experiments show in which lithology the SSEs in the Hikurangi subduction margin occur. I then proceed to expand the results of the laboratory experiments to natural faults, after which I briefly explore how the variables may interact.

### 5.2 How does the surface morphology of a fault influence the frictional stability?

Using laboratory experiments on Rochester Shale and pure quartz powders, I show in Chapter 0 that the development of anisotropy in the surface roughness of a fault is directly linked to the frictional stability of a fault. The fault surfaces that develop in quartz are rough, compared to the shale, and do not become smoother with displacement. The fault surfaces that develop in the shale are smoother, and become preferentially smoother parallel to the sliding direction with increasing slip, which leads to an anisotropic roughness or a striated fault surface. The development of a striated fault surface coincides with a drop in friction coefficient  $\mu$  and an increase in frictional stability parameter  $a-b$ . No spontaneous slip instabilities occur during this study.

By comparing the experimental data to previous work, I show the relationship between roughness anisotropy and  $a-b$  is valid for a range of geological materials and therefore likely

widely applicable. The low friction coefficient of the shale, which is the result of a low interparticle friction, might aid in the rearrangement of grains and therefore in the striation formation. However, comparison to other materials shows that striations form when the frictional behavior is velocity-strengthening independent of the friction coefficient. Therefore, there is no direct relationship between friction coefficient and fault surface roughness.

That no spontaneous slip events occur in the quartz, despite the velocity-weakening behavior is because a negative  $a-b$  is only one prerequisite for unstable slip, but also the critical stiffness criterion  $k < k_c$  must be satisfied (section 1.2.4, equation 1.10). A quick calculation using average values of  $a-b$  of -0.004 and  $D_c$  is 20  $\mu\text{m}$  (section 2.4&2.5.3) at the applied effective normal stress of 10 MPa shows  $k_c$  is on the order of 2 MPa/mm. The machine stiffness  $k$  as we show in chapter 4 is  $\sim 9$  MPa/mm at 10 MPa normal stress. Therefore,  $k < k_c$  is not satisfied and the stable sliding I observe in the quartz despite the velocity-weakening behavior is expected.

The main conclusion from chapter 2 and the answer to this research question is that anisotropic fault surface morphology coincides with velocity-strengthening behavior and that isotropic fault surfaces show velocity-weakening behavior. An important note to this finding is that the causal relationship implied by the question, is not shown. At this point, it is not possible to conclude whether the surface morphology dictates frictional behavior, that the surface anisotropy is a result of the frictional behavior, or that both are the result of a different process, such as grain rearrangement.

### 5.3 How does the stiffness normal to the fault zone influence the occurrence and nature of slip instabilities?

To answer this research question, I use laboratory experiments on pure quartz powder, presented in chapter 3. I varied the machine stiffness in the fault-normal and shear-parallel direction separately, by using springs in both the direction normal to the fault surface and parallel to the shear stress. The main findings are twofold: decreasing the fault-normal stiffness causes the friction coefficient  $\mu$  and  $a-b$  to increase and decreasing the fault-normal stiffness leads to spontaneous slip instabilities. These two findings seem difficult to relate at first, as the less negative  $a-b$  at low fault-normal stiffness would lead to lower values of  $k_c$ , thereby bringing the fault further away from satisfying the critical stiffness criterion  $k < k_c$  when unstable slip would be expected. The two findings are explained separately, where the frictional behavior is a direct result

of the lower fault-normal stiffness, whereas the slip events that occur, occur by a different mechanism that is not described by the critical stiffness criterion.

The changes in frictional behavior, higher  $\mu$  and higher  $a-b$  with decreasing fault-normal stiffness, I explain by more volumetric deformation occurring when fault-normal stiffness is low. Volumetric strain involves work against the normal stress, which adds to the observed shear stress and therefore results in a higher friction coefficient. The higher  $a-b$  can also be explained by more volumetric deformation at low fault-normal stiffness resulting in higher  $a$ .

I explain the occurrence of the observed instabilities by a different mechanism, the wrinkle-like slip pulse. This type of slip pulse occurs when the elastic properties on both sides of the fault are different. The fault then does not occur in a homogeneous material, but is better described by sliding on a bimaterial interface. Reducing the fault-normal stiffness on one side of the fault induces such a stiffness asymmetry. The most distinctive properties of a wrinkle-like slip pulse, uni-directional rupture propagation and a low propagation velocity, are not measurable in our set-up. The increased ground motion or fault-normal movement inferred for wrinkle-like slip pulses, can be measured only indirectly, and is higher for the wrinkle-like slip pulses. I also show that the peak slip velocity and event slip increase with stiffness contrast, as expected for wrinkle-like slip pulses.

Reducing the shear-parallel stiffness results in a transition from stable sliding through slow slip events to rapid earthquake slip, as has been previously shown. At the low shear-parallel stiffness where these expected slip events occur, additionally reducing the fault-normal stiffness results in less regular events with on average smaller stress drops and lower peak slip velocities. Also this is the result of a component of wrinkle-like slip pulses that interact with the crack-like slip pulses expected by the critical stiffness criterion.

Like my findings, the answer to this research question is twofold. Reducing the fault-normal stiffness increases the faults frictional strength and makes the fault less velocity-weakening, which should stabilize slip. However, reducing the fault-normal stiffness on one side of the fault induces an asymmetry in stiffness, which when large enough, results in the occurrence of wrinkle-like slip events.

#### 5.4 At the Hikurangi subduction zone margin, how does lithology control the occurrence of the observed shallow slow slip events

This research question sprouts from the known effects lithology has on frictional behavior and the research opportunities that the well-documented and very shallow SSEs that occur in the Hikurangi margin provide. To answer this research question, I made use of samples drilled during IODP Expedition 375 at site U1520, which is on an undisturbed part of the incoming plate. This enables me to do experiments on sediments that are an accurate representation of the lithologies present in the subduction zone. To have an as accurate as possible representation of the conditions at which the SSEs occur, I test the frictional behavior of those sediment at driving velocities close to the in-situ plate convergence rate and driving velocities that occur during the SSEs, the results of which are presented in chapter 4.

Under different testing conditions for intact and powdered samples, at in-situ and 10 MPa effective normal stress, spontaneous SSEs only occur in calcite-rich samples. There is no trend in friction parameters with depth, but the calcite-rich lithologies are relatively strong and show mostly velocity-weakening behavior. However, I show spontaneous slip instabilities can also occur during velocity-strengthening conditions. The frictionally weak lithologies on the other hand show velocity-strengthening behavior. If deformation would localize in the weakest layer, the occurrence of slow slip events is unlikely.

Pinpointing the mechanisms that causes the observed spontaneous laboratory SSEs has proven difficult. The critical stiffness criterion is not satisfied for various samples that do show slow slip events. An addition to the critical stiffness theory introducing a second stiffness criterion  $k < k_b$  that predicts a value when slow instabilities may start, but which will only become dynamic instabilities when also  $k < k_c$  is satisfied, can predict the occurrence of SSEs slightly better, but also not for all experiments. The existence of a cut-off velocity can explain SSEs, requires a transitions from velocity-weakening at low velocity to velocity-strengthening behavior above the cut-off velocity. However, I do not observe a dependency of  $a-b$  on driving velocity.

The direct answer to this research question is therefore simple, the calcite-content of the lithology controls whether or not slow slip events occur. Without a satisfactory mechanism that explains why specifically the calcite-rich lithologies host the SSEs, it is however difficult to expand this finding to different conditions or to subduction zones where different lithologies are present. It also poses the problem why the frictionally strong calcite-rich sediments are in the deformation zone instead of deformation being localized in the frictionally weak sediments. My

explanation for this last point is the introduction of the calcite-rich lithologies into a heterogeneous deformation zone due to subduction of seamounts.

## 5.5 How can our findings be applied to natural faults?

As mentioned in the introduction, laboratory experiments have the advantage that it is possible to separate out variables and to single out the influence of one variable at a time. However, to apply laboratory findings to natural faults, scale differences need to be considered, especially regarding the differences in time and sample size. The laboratory samples used in the studies presented here are several cm across, whereas natural faults can be several kilometers in size. The driving velocities used during most experiments are significantly higher than the actual deformation rates on faults, therefore the asperities will be in contact for shorter times than when the driving velocity would be a realistic value representative for the fault zone. The smaller sample size also limits the amount of slip that occurs during a single event, which can be meters for natural earthquakes, but is generally limited to tens of  $\mu\text{m}$ 's on our samples.

I show fault surface roughness can be used to overcome the length scaling problem, as it is scalable over many orders of magnitude wavelengths. Friction parameters  $a$  and  $b$  can be related to the roughness of the fault surface and the relationship between frictional behavior and fault surface anisotropy should therefore be applicable to larger scale faults. Since I show differences in intrinsic frictional properties, the time-dependence or sliding velocity dependence does not play a major role here. The relationship I present would predict seismogenic faults are rough and isotropic, which contradicts observations from natural faults, which are commonly striated. Possible explanations for this discrepancy might be that natural fault surfaces are often defined as fault surface when they display striations or anisotropic roughness, whereas isotropic fault surfaces might not be recognized as a fault surface, so a sampling bias. Another explanation I propose is a late phase of velocity-strengthening sliding or possibly afterslip. Either the exposed fault was seismogenic at depth, but becomes velocity-strengthening at very shallow depths, or the striations do not form during the earthquake itself, but during the last moments of sliding where the fault is slowing down and is velocity-strengthening, or afterslip occurs after the seismic event that causes the striations. The relationship I propose between velocity-dependent frictional behavior and fault surface anisotropy is consistent with the interpretation of an active megathrust in Costa Rica. There, large parts of the fault are corrugated and anisotropic, but rough patches form due to interaction of the megathrust with normal faults. These rough patches are interpreted as potential earthquake sources.

An unresolved question here is the scaling of the critical slip distance  $D_c$  from laboratory samples to natural faults. Two possible scaling relationships have been suggested, either  $D_c$  is a minimum size of asperities below which asperities deform plastically, rather than brittle. This minimum size of fault surface anisotropy is scale-independent, therefore  $D_c$  would not have to be scaled from the laboratory to natural faults. A common physical interpretation of  $D_c$  is however that it represents the average size of asperities or the slip distance needed to completely renew the asperity population on a fault. On a self-affine fault surface, contact asperities depend on the fault length considered, for example a cm-scale laboratory sample could have asperities on the  $\mu\text{m}$  size, whereas a natural fault of several kilometers length could have asperities of several meters. If  $D_c$  represents average asperity size, it should therefore be scaled from the laboratory to natural faults, depending on the fault roughness and size of the slipping fault. The results I present in this thesis are however not conclusive and cannot distinguish if  $D_c$  is related to asperity size or the minimum anisotropy value.

Relating the results of varying normal stiffness to natural faults is challenging, since fault-normal stiffness is not commonly measured. The main new finding here is the wrinkle-like slip pulses that occur when a stiffness contrast is present. To be able to relate my findings regarding wrinkle-like slip pulses from the laboratory to natural faults, I would need to determine the stiffness contrast in the laboratory and pinpoint more accurately at which value of stiffness contrast these events occur. The stiffness contrast can be measured on natural faults, so when I determine how the stiffness contrast controls these events, the results can be applied to natural faults. How important these pulses are on natural faults is still debated. One important argument here seems that using realistic rupture models, a slip pulse driven by a stress drop due to friction decreasing from a higher static to a lower dynamic friction coefficient is more efficient than the wrinkle-like slip pulse. One issue regarding the scale difference between laboratory samples and natural faults is that slip pulses do not have to propagate over large distances on a small laboratory sample. Characteristics such as self-sharpening of the pulse or divergence of the pulse would therefore be difficult to observe on a small sample even with the right sensors installed. Without being able to determine with more certainty if the slip events I observe are indeed wrinkle-like slip pulses, and with the current debate if wrinkle-like slip pulses occur in nature, relating my findings to natural faults remains speculative.

The finding most easily related to natural faults are the results from the Hikurangi margin. Here, I use natural samples and realistic deformation rates, so that time scaling is not an issue. I also show that slip event characteristics such as the increase of stress drop with increasing peak slip velocity are scalable according to scaling laws known from natural earthquakes. The problem

with applying the results found in this study is that without pinpointing the mechanism causing the SSEs, it is difficult to upscale the results, or to apply the results to other subduction zones. My results clearly show that the calcite-rich lithologies host the slow slip events, but this might not be true for other subduction zones. There must be a physical property of the calcite that causes the slow slip events, which can also occur in other minerals in subduction zones where the SSEs are not bound to calcite-rich lithologies. One requirement for faults to show repetitive slip events is that they regain strength during the inter-seismic period. I therefore propose the explanation why the SSEs occur in the calcite-rich layers may have to do with the comparably high healing rate of calcite compared to other lithologies, but healing experiments would be required to prove this.

Explaining how the calcite-rich lithologies can host the SSEs in the Hikurangi margin is also challenging. The calcite-rich lithologies are relatively strong, whereas the weakest layers, in which deformation would most likely localize, are velocity-strengthening and therefore not capable of hosting slip events. In between these two lithologies is also another layer of volcanoclastic conglomerates that have an intermediate strength and mostly velocity-neutral behavior. For SSEs to occur, the calcite rich lithologies must however be incorporated in the deformation zone. I propose this occur by stepping up of the décollement when strong seamounts subduct. A trail of sediments may follow the subducted seamount, in which the calcite-rich lithologies are present.

## 5.6 How are fault zone roughness, fault normal stiffness and lithology related, and how do they influence each other?

To give a well-funded answer to how the three different effects influence one another, specific testing would be needed to test exactly that. My findings, in combination with theoretical considerations however already give some clues about how they are related. Figure 5.1 summarizes these relationships, of which some are known from theory or related to findings in this thesis and some are more speculative.

The most direct influence is that of lithology on stiffness. The lithology specific shear and bulk moduli control the stiffness of the host rock in the shear and fault-normal direction. A stiffness contrast across the fault, when caused by juxtaposition of different lithologies is directly controlled by the ratio of the bulk moduli of the two materials. More complex is the interplay between lithology, damage and stiffness or stiffness contrasts. I show, that the stiffness and

especially the normal stiffness contrast controls the mode of fault sliding. Stable sliding is less likely to cause a large damage zone than slip instabilities. Loss of cohesion due to off-fault damage influences the physical properties and therefore the lithology. A fractured rock may also have more fluid circulation, thereby changing the composition of the host rock. However, as the role of wrinkle-like slip pulses on natural faults is not entirely clear yet, it is difficult to say how wrinkle-like versus crack-like slip influence the structural integrity of a rock.

The interplay of fault roughness and stiffness or stiffness contrast seems multiple, although most of these are speculative. Rougher faults are for example likely to have larger damage zones, because a larger volume of rock participates in the deformation. Larger damage zones lead to a reduction in host rock stiffness and if damage occurs preferentially on one side of the fault, also to a stiffness asymmetry across the fault. Another point to consider regarding roughness is that when faults smoothen with slip, as I show occurs for the shale samples presented in chapter 2, if the influence of normal stiffness on frictional parameters decreases. I explain the effects a reduction in fault-normal stiffness has on friction coefficient  $\mu$  and parameter  $a-b$  by more volumetric deformation occurring at low fault-normal stiffness. For smooth faults, where there is negligible volumetric deformation, it might therefore be expected that a reduction in stiffness has little to no effect. However, if a reduction in fault-normal stiffness leads to more volumetric deformation this may lead to a thicker deformation zone, which may in turn increase the fault surface roughness.

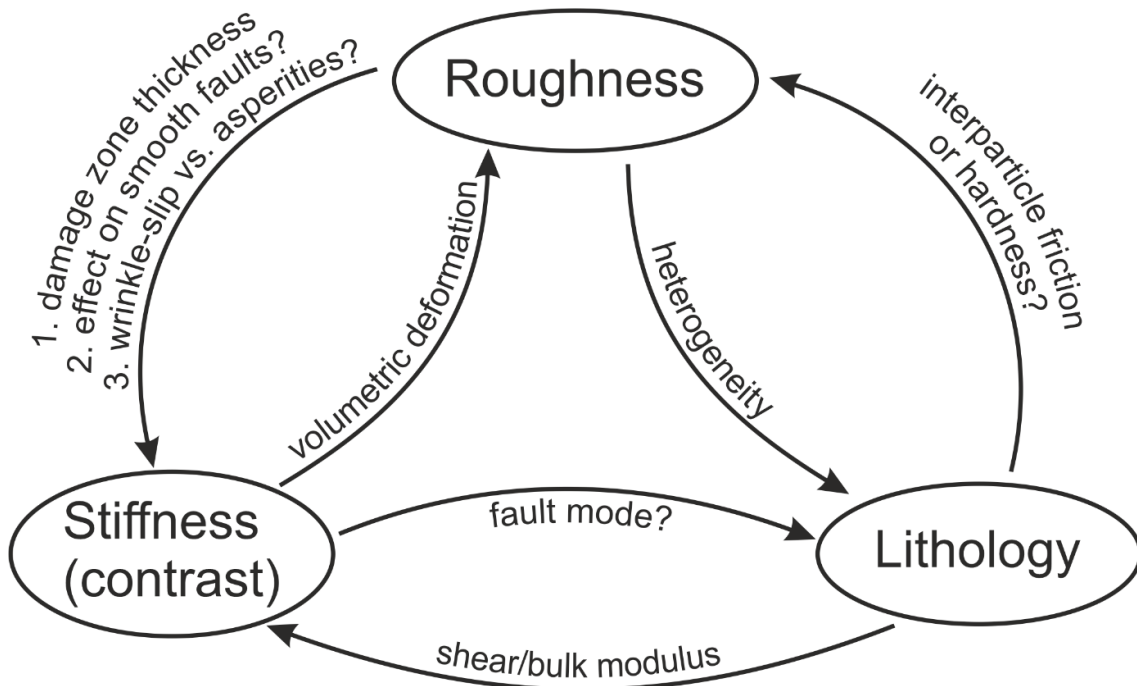


Figure 5.1: Schematic overview of how the three different variables studied in this thesis may interact

More speculative is the effect roughness has on wrinkle-like slip pulses. As wrinkle-like slip pulses depend on a reduction of shear traction on the surface by fault-normal movement on the fault, it would be expected that on rougher faults, more normal movement is needed and therefore a larger stiffness contrast might be needed before wrinkle-like slip pulses occur. Should this effect occur, then wrinkle-slip pulses would occur preferentially on smooth surfaces, whereas we show that smoother faults are prone to stable sliding behavior based on the finding that they are velocity-strengthening. Under certain circumstances, wrinkle-like slip pulses may however also occur on velocity-strengthening faults. This poses the question which of the effects will be more important on a smooth, striated fault with a stiffness contrast, the velocity-strengthening friction due to anisotropic fault morphology, or wrinkle-like slip pulses that occur due to a low fault roughness.

Considering the interactions between lithology and roughness, I can use the observations from two different studies. That lithology has an effect on roughness is clear from my surface anisotropy study (chapter 2). The two different lithologies I test develop fault surfaces with different roughness characteristics. I report on previous work that has shown that under the right conditions, quartz can develop striated surfaces and therefore show the same surface roughness anisotropy as I observe during this study. Under the same conditions, lithology however has a clear effect. For the two materials tested, I explain the difference may lie in the lower interparticle friction of the shale grains, compared to the quartz, which may facilitate grain rearrangement into the smooth striated surfaces. Since the development of striated surface is not limited to materials with a low interparticle friction, other rock properties must be able to control surface roughness as well. One possible property is mineral hardness; low hardness would lead to a large contact area that may cause smoothening of the fault with displacement.

That fault roughness may in turn influence the lithology of the fault zone, is described in the Hikurangi study (chapter 4). In this specific case the roughness is caused by incoming seamounts, which causes a geometrically complex deformation zone, in which a mix of lithologies is present. Exactly how large this effect is, is difficult to say without knowing the degree of lithological mixing in the deformation zone. In the extreme case, this may even lead to stiffness differences that cause a component of wrinkle-pulse slip on the plate-boundary fault. This would however lead to irregular fast events (chapter 3), whereas at the Hikurangi margin mostly regular slow slip events are observed, although ordinary earthquakes do occur. Therefore, it seems in the Hikurangi margin the roughness does lead to heterogeneous lithologies in the deformation zone, but not to an extent large enough to cause stiffness contrasts large enough to host wrinkle-like slip pulses.

## 5.7 Conclusions

From the surface roughness anisotropy study present in chapter 2, I conclude that unstable sliding occurs on anisotropic, rough fault patches, whereas stable sliding occurs on smoother, striated faults. I show the frictional parameters  $a$  and  $b$  are related to the scalable self-affine fault surface roughness, which implies the findings can be directly applied to natural faults. I present a conceptual fault model where various processes may affect fault roughness, which leads to rough fault patches where unstable sliding may occur. The stiffness study presented in chapter 3 shows that a low shear stiffness results in a transition from stable sliding to slow and ordinary earthquakes. A reduction in fault-normal stiffness makes the fault stronger and less velocity-weakening, whereas a stiffness contrast across the fault may lead to wrinkle-like slip pulses. I describe various processes that can influence the stiffness, the most important of which are lithology and off-fault damage. Chapter 4 shows that at the Hikurangi margin, SSEs occur specifically in the calcite-rich lithologies. However, fault roughness in the form of incoming seamounts is needed to get deformation in the lithologies with unstable frictional behavior. In the above section, I discuss how all of these different factors can be related and how they may interact.

The most widely accepted view when earthquakes occur, which I present in the introduction (chapter 1), is that a transition occurs from stable sliding, through slow slip events to ordinary earthquakes when the critical stiffness  $k_c$  is lower, equal or higher than the host rock stiffness. First, I show that striated faults display velocity-strengthening behavior, which means the critical stiffness  $k_c$  is negative, so that sliding will always be stable. For the rough and isotropic quartz surfaces, I show that as long as there is no fault stiffness contrast across the fault, this expected transition in slip instabilities occurs with decreasing host rock stiffness parallel to the shear stress. When there is a stiffness contrast, a different type of slip instabilities occur, wrinkle-like slip pulses, that are not described by the critical stiffness criterion. When the critical stiffness criterion is satisfied and there is a stiffness contrast, both mechanisms interact.

From these observations, I can conclude that seismogenic behavior is expected on rough, isotropic fault surfaces when the critical stiffness criterion is satisfied or when there is a stiffness contrast across the fault. Although the laboratory results indicate that this relationship is scale-independent, striated seismogenic faults have been observed in nature (chapter 2). Also our results presented in chapter 4, shows that the slow slip events that occur at the Hikurangi margin are not explained by this criterion. At the same time, I show the occurrence of these slow slip events is related to the presence of seamounts, which produces a rough fault. The relationship between fault roughness and slip instabilities is therefore robust.

## 5.8 Open questions and future research

In this thesis, I show some basic controls roughness and fault-zone stiffness have on a faults slip behavior. Some open questions are what controls the surface roughness and the formation of fault surface anisotropy. Future research may also focus on how fault surface roughness evolves during the transition from velocity-strengthening to velocity-weakening. This transition is not captured in detail in this work. Additional questions related to the surface roughness may focus on how it changes with sliding velocity, normal stress and temperature. Especially interesting would be how fault roughness evolves during the earthquake cycle from slow speeds to seismogenic speeds, and during the phase where the fault slows down again. The focus should be on explaining observations from natural faults, the common occurrence of striated fault surfaces, including on seismogenic faults, and striated pseudotachylytes suggests that earthquakes may occur on anisotropic fault surfaces, despite our findings.

Future research to elucidate the occurrence of wrinkle-like slip pulses in the laboratory is also of interest. Whereas extensive numerical modelling studies exist to predict under what circumstances these pulses may exist, laboratory examples are limited. It would however help if these studies would make use of sensors that can measure the rupture propagation speed and direction, as this is the main characteristic that distinguishes wrinkle-like slip pulses, as well as better vertical motion sensors or fluid pressure sensors to measure volumetric deformation. Specifically, quantification of the stiffness contrast needed for these type of events to occur would be interesting, because that is a property that can also be measured for natural faults.

In general, bimaterial interfaces have received relatively little attention so far, whereas it is clear that across large faults, the material on both sides of the fault is rarely perfectly similar. This would be of specific interest in subduction zones, which host the largest earthquakes worldwide and the plate-boundary fault is likely to separate various lithologies. The interplay with the other variables studied here would be interesting, if a fault separates a velocity-weakening from a velocity-strengthening material, which lithology controls the fault surface roughness and does the fault surface show striations?



## 6 References

- Abe, Y., and Kato, N., 2013, Complex Earthquake Cycle Simulations Using a Two-Degree-of-Freedom Spring-Block Model with a Rate- and State-Friction Law: *Pure and Applied Geophysics*, v. 170, p. 745–765, doi:10.1007/s00024-011-0450-8.
- Adams, G.G., 1995, Self-excited oscillations of two elastic half-spaces sliding with a constant coefficient of friction: *Journal of Applied Mechanics, Transactions ASME*, v. 62, p. 867–872, doi:10.1115/1.2896013.
- Ampuero, J.P., and Rubin, A.M., 2008, Earthquake nucleation on rate and state faults - Aging and slip laws: *Journal of Geophysical Research: Solid Earth*, v. 113, p. 1–21, doi:10.1029/2007JB005082.
- Andrews, D.J., 1976, Rupture Propagation With Finite Stress in Antiplane Strain.: *Journal of Geophysical Research*, v. 81, p. 3575–3582, doi:10.1029/JB081i020p03575.
- Andrews, D.J., and Ben-Zion, Y., 1997, Wrinkle-like slip pulse on a fault between different materials: *Journal of Geophysical Research B: Solid Earth*, v. 102, p. 553–571, doi:10.1029/96jb02856.
- Andrews, D.J., and Harris, R.A., 2005, The wrinkle-like slip pulse is not important in earthquake dynamics: *Geophysical Research Letters*, v. 32, p. 1–4, doi:10.1029/2005GL023996.
- Audet, P., and Bürgmann, R., 2014, Possible control of subduction zone slow-earthquake periodicity by silica enrichment: *Nature*, v. 510, doi:10.1038/nature13391.
- Badt, N., Hatzor, Y.H., Toussaint, R., and Sagy, A., 2016, Geometrical evolution of interlocked rough slip surfaces: The role of normal stress: *Earth and Planetary Science Letters*, v. 443, p. 153–161, doi:10.1016/j.epsl.2016.03.026.
- Barker, D.H.N., Henrys, S., Caratori Tontini, F., Barnes, P.M., Bassett, D., Todd, E., and Wallace, L., 2018, Geophysical Constraints on the Relationship Between Seamount Subduction, Slow Slip, and Tremor at the North Hikurangi Subduction Zone, New Zealand: *Geophysical Research Letters*, v. 45, p. 12,804–12,813, doi:10.1029/2018GL080259.
- Barnes, P.M. et al., 2019, Site U1520: Wallace, L.M., Saffer, D.M., Barnes, P.M., Pecher, I.A., Petronotis, K.E., LeVay, L.J., and the Expedition 372/375 Scientists, Hikurangi Subduction Margin Coring, Logging, and Observatories. *Proceedings of the International Ocean Discovery Program, 372B/3*, doi:10.14379/iodp.proc.374.107.2019.
- Barnes, P.M. et al., 2020, Slow slip source characterized by lithological and geometric heterogeneity: *Science Advances*, v. 6, p. 1–11, doi:10.1126/sciadv.aay3314.
- Baumberger, T., Berthoud, P., and Caroli, C., 1999, Physical analysis of the state- and rate-dependent friction law. II. Dynamic friction: *Physical Review B - Condensed Matter and Materials Physics*, v. 60, p. 3928–3939, doi:10.1103/PhysRevB.60.3928.
- Baumberger, T., Heslot, F., and Perrin, B., 1994, Crossover from creep to inertial motion in friction dynamics: *Nature*, v. 367, p. 544–546.
- Beeler, N.M., 2007, Laboratory-Observed Faulting in Intrinsically and Apparently Weak Materials: Strength, Seismic Coupling, Dilatancy, and Pore-Fluid Pressure: *The Seismogenic Zone of Subduction Thrust Faults*, p. 370–449, doi:10.7312/dixo13866-013.
- Bell, R., Sutherland, R., Barker, D.H.N., Henrys, S., Bannister, S., Wallace, L., and Beavan, J., 2010, Seismic reflection character of the Hikurangi subduction interface, New Zealand, in the region of repeated Gisborne slow slip events: *Geophysical Journal International*, v. 180, p. 34–48, doi:10.1111/j.1365-246X.2009.04401.x.
- Ben-Zion, Y., 2001, Dynamic ruptures in recent models of earthquake faults: v. 49, 2209–2244 p., doi:10.1016/S0022-5096(01)00036-9.
- Ben-Zion, Y., and Huang, Y., 2002, Dynamic rupture on an interface between a compliant fault zone layer and a stiffer surrounding solid: *Journal of Geophysical Research*, v. 107, doi:10.1029/2001jb000254.

- Ben-Zion, Y., and Shi, Z., 2005, Dynamic rupture on a material interface with spontaneous generation of plastic strain in the bulk: *Earth and Planetary Science Letters*, v. 236, p. 486–496, doi:10.1016/j.epsl.2005.03.025.
- Beroza, G.C., and Ide, S., 2011, Slow earthquakes and nonvolcanic tremor: *Annual Review of Earth and Planetary Sciences*, v. 39, p. 271–296, doi:10.1146/annurev-earth-040809-152531.
- Bhattacharya, P., Rubin, A.M., Bayart, E., Savage, H.M., and Marone, C., 2015, Critical evaluation of state evolution laws in rate and state friction: Fitting large velocity steps in simulated fault gouge with time-, slip-, and stress-dependent constitutive laws: *Journal of Geophysical Research: Solid Earth*, v. 120, p. 6365–6385, doi:10.1002/2015JB012437.
- Biegel, R.L., Wang, W., Scholz, C.H., Boitnott, G.N., and Yoshioka, N., 1992, Micromechanics of rock friction: 1. Effects of surface roughness on initial friction and slip hardening in Westerly granite: *Journal of Geophysical Research*, v. 97, p. 8951–8964, doi:10.1029/92JB00042.
- Bilham, R., Suszek, N., and Pinkney, S., 2004, California creepmeters: *Seismological Research Letters*, v. 75, p. 481–492, doi:10.1785/gssrl.75.4.481.
- Bistacchi, A., Ashley Griffith, W., Smith, S.A.F., di Toro, G., Jones, R., and Nielsen, S., 2011, Fault Roughness at Seismogenic Depths from LIDAR and Photogrammetric Analysis: *Pure and Applied Geophysics*, v. 168, p. 2345–2363, doi:10.1007/s00024-011-0301-7.
- Brietzke, G.B., Cochard, A., and Igel, H., 2009, Importance of bimaterial interfaces for earthquake dynamics and strong ground motion: *Geophysical Journal International*, v. 178, p. 921–938, doi:10.1111/j.1365-246X.2009.04209.x.
- Brodsky, E.E., Gilchrist, J.J., Sagy, A., and Colletini, C., 2011, Faults smooth gradually as a function of slip: *Earth and Planetary Science Letters*, v. 302, p. 185–193, doi:10.1016/j.epsl.2010.12.010.
- Brodsky, E.E., McLaskey, G.C., and Ke, C., 2020, Groove Generation and Coalescence on a Large-Scale Laboratory Fault: *AGU Advances*, v. 1, doi:10.1029/2020av000184.
- Brodsky, E.E., and Mori, J., 2007, Creep events slip less than ordinary earthquakes: *Geophysical Research Letters*, v. 34, p. 1–5, doi:10.1029/2007GL030917.
- Brown, S.R., and Scholz, C.H., 1985, Broad bandwidth study of the topography of natural rock surfaces.: *Journal of Geophysical Research*, v. 90, doi:10.1029/jb090ib14p12575.
- Bürgmann, R., 2018, The geophysics, geology and mechanics of slow fault slip: *Earth and Planetary Science Letters*, v. 495, p. 112–134, doi:10.1016/j.epsl.2018.04.062.
- Candela, T., and Brodsky, E.E., 2016, The minimum scale of grooving on faults: *Geology*, v. 44, p. 603–606, doi:10.1130/G37934.1.
- Candela, T., Renard, F., Bouchon, M., Brouste, A., Marsan, D., Schmittbuhl, J., and Voisin, C., 2009, Characterization of fault roughness at various scales: Implications of three-dimensional high resolution topography measurements: *Pure and Applied Geophysics*, v. 166, p. 1817–1851, doi:10.1007/s00024-009-0521-2.
- Candela, T., Renard, F., Klinger, Y., Mair, K., Schmittbuhl, J., and Brodsky, E.E., 2012, Roughness of fault surfaces over nine decades of length scales: *Journal of Geophysical Research: Solid Earth*, v. 117, p. 1–30, doi:10.1029/2011JB009041.
- Carpenter, B.M., Ikari, M.J., and Marone, C., 2016, Laboratory observations of time-dependent frictional strengthening and stress relaxation in natural and synthetic fault gouges: *Journal of Geophysical Research: Solid Earth*, v. 121, p. 1183–1201, doi:10.1002/2015JB012136.
- Chen, X., Madden, A.S., Bickmore, B.R., and Reches, Z., 2013, Dynamic weakening by nanoscale smoothing during high-velocity fault slip: *Geology*, v. 41, p. 739–742, doi:10.1130/G34169.1.
- Chen, J., and Niemeijer, A.R., 2017, Seismogenic Potential of a Gouge-filled Fault and the Criterion for Its Slip Stability: Constraints From a Microphysical Model: *Journal of Geophysical Research: Solid Earth*

- Earth, v. 122, p. 9658–9688, doi:10.1002/2017JB014228.
- Collot, J.Y., Lewis, K., Lamarche, G., and Lallemand, S., 2001, The giant Ruatoria debris avalanche on the northern Hikurangi margin, New Zealand: Result of oblique seamount subduction: *Journal of Geophysical Research: Solid Earth*, v. 106, p. 19271–19297, doi:10.1029/2001jb900004.
- Cook, N.G.W., 1981, Stiff Testing Machines, Stick Slip Sliding, and the Stability of Rock Deformation: *Geophysical Monograph Series*, v. 24, p. 93–102, doi:10.1029/gm024p0093.
- Cowie, P.A., and Scholz, C.H., 1992, Growth of faults by accumulation of seismic slip: *Journal of Geophysical Research*, v. 97, p. 85–95, doi:10.1029/92jb00586.
- Dascher-Cousineau, K., Kirkpatrick, J.D., and Cooke, M.L., 2018, Smoothing of Fault Slip Surfaces by Scale-Invariant Wear: *Journal of Geophysical Research: Solid Earth*, p. 7913–7930, doi:10.1029/2018JB015638.
- Davidesko, G., Sagy, A., and Hatzor, Y.H., 2014, Evolution of slip surface roughness through shear: *Geophysical Research Letters*, v. 41, p. 1492–1498, doi:10.1002/2013GL058913.
- Deirich, A., Ortega, J.A., Ulm, F.J., and Abousleiman, Y., 2012, Nanochemomechanical assessment of shale: A coupled WDS-indentation analysis: *Acta Geotechnica*, v. 7, p. 271–295, doi:10.1007/s11440-012-0185-4.
- DeMets, C., Gordon, R.G., Argus, D.F., and Stein, S.C.N., 1994, Effect of Recent Revisions to the Geomagnetic Reversal Time-Scale on Estimates of Current Plate Motions: *Geophysical Research Letters*, v. 21, p. 2191–2194.
- Dieterich, J.H., 1981, Constitutive properties of faults with simulated gouge, *in* *Mechanical Behavior of Crustal Rocks*, p. 103–120.
- Dieterich, J.H., 1992, Earthquake nucleation on faults with rate-and state-dependent strength: *Tectonophysics*, v. 211, p. 115–134, doi:10.1016/0040-1951(92)90055-B.
- Dieterich, J.H., 1979, Modeling of rock friction 1. Experimental results and constitutive equations: *Journal of Geophysical Research: Solid Earth*, v. 84, p. 2161–2168, doi:10.1029/JB084iB05p02161.
- Dieterich, J.H., 1978, Time-Dependent Friction and the Mechanics of Stick-Slip: *Rock friction and earthquake prediction*, v. 116, p. 790–806.
- Dieterich, J.H., 1972, Time-dependent friction in rocks: *Journal of Geophysical Research*, v. 77, p. 3690–3697, doi:10.1029/jb077i020p03690.
- Dieterich, J.H., and Kilgore, B.D., 1994, Direct Observation of Frictional Contacts: New Insights for State-dependent Properties: *Pure and Applied Geophysics PAGEOPH*, v. 143, p. 283–302.
- Dieterich, J.H., and Kilgore, B.D., 1996, Imaging surface contacts: power law contact distributions and contact stresses in quartz, calcite, glass and acrylic plastic: *Tectonophysics*, v. 256, p. 219–239, doi:10.1016/0040-1951(95)00165-4.
- Dmitrieva, K., Hotovec-Ellis, A.J., Prejean, S., and Dunham, E.M., 2013, Frictional-faulting model for harmonic tremor before Redoubt Volcano eruptions: *Nature Geoscience*, v. 6, p. 652–656, doi:10.1038/ngeo1879.
- Doblas, M., 1998, Slickenside kinematic indicators: *Tectonophysics*, v. 295, p. 187–197, doi:10.1016/S0040-1951(98)00120-6.
- Dor, O., Rockwell, T.K., and Ben-Zion, Y., 2006, Geological observations of damage asymmetry in the structure of the San Jacinto, San Andreas and Punchbowl faults in Southern California: A possible indicator for preferred rupture propagation direction: *Pure and Applied Geophysics*, v. 163, p. 301–349, doi:10.1007/s00024-005-0023-9.
- Dragert, H., Wang, K., and James, T.S., 2001, A silent slip event on the deeper Cascadia subduction interface: *Science*, v. 292, p. 1525–1528.

- Dunham, E.M., and Rice, J.R., 2008, Earthquake slip between dissimilar poroelastic materials: *Journal of Geophysical Research: Solid Earth*, v. 113, p. 1–20, doi:10.1029/2007JB005405.
- Edmond, J.M., and Paterson, M.S., 1972, Volume changes during the deformation of rocks at high pressures: *International Journal of Rock Mechanics and Mining Sciences*, v. 9, p. 161–182.
- Ellsworth, W.L., and Beroza, G.C., 1995, Seismic evidence for an earthquake nucleation phase: *Science*, v. 268, p. 851–855, doi:10.1126/science.268.5212.851.
- Engelder, J.T., and Scholz, C.H., 1976, The role of asperity indentation and ploughing in rock friction—II: *International Journal of Rock Mechanics and Mining Sciences & Geomechanics Abstracts*, v. 13, p. 155–163, doi:10.1016/0148-9062(76)90820-2.
- Fagereng, Å., and Ellis, S., 2009, On factors controlling the depth of interseismic coupling on the Hikurangi subduction interface, New Zealand: *Earth and Planetary Science Letters*, v. 278, p. 120–130, doi:10.1016/j.epsl.2008.11.033.
- Fagereng, Å., and Ikari, M.J., 2020a, Low-Temperature Frictional Characteristics of Chlorite-Epidote-Amphibole Assemblages: Implications for Strength and Seismic Style of Retrograde Fault Zones: *Journal of Geophysical Research: Solid Earth*, v. 125, p. 1–16, doi:10.1029/2020jb019487.
- Fagereng, Å., and Ikari, M.J., 2020b, Low - Temperature Frictional Characteristics of Chlorite - Epidote - Amphibole Assemblages : Implications for Strength and Seismic Style of Retrograde Fault Zones: *Journal of Geophysical Research: Solid Earth*, v. 125, p. 1–16, doi:10.1029/2020JB019487.
- Faulkner, D.R., Mitchell, T.M., Healy, D., and Heap, M.J., 2006, Slip on “weak” faults by the rotation of regional stress in the fracture damage zone: *Nature*, v. 444, p. 922–925, doi:10.1038/nature05353.
- Fondriest, M., Smith, S.A.F., Candela, T., Nielsen, S.B., Mair, K., and Toro, G. Di, 2013, Mirror-like faults and power dissipation during earthquakes: *Geology*, v. 41, p. 1175–1178, doi:10.1130/G34641.1.
- Freund, L.B., 1979, The mechanics of dynamic shear crack propagation: *Journal of Geophysical Research: Solid Earth*, v. 84, p. 2199–2209, doi:10.1029/JB084iB05p02199.
- Gee, M.J.R., Gawthorpe, R.L., and Friedmann, J.S., 2005, Giant striations at the base of a submarine landslide: *Marine Geology*, v. 214, p. 287–294, doi:10.1016/j.margeo.2004.09.003.
- Ghisetti, F.C., Barnes, P.M., Ellis, S., Plaza-Faverola, A.A., and Barker, D.H.N., 2016, The last 2 Myr of accretionary wedge construction in the central Hikurangi margin (North Island, New Zealand): Insights from structural modeling: *Geochemistry, Geophysics, Geosystems*, v. 17, p. 2661–2686, doi:10.1002/2016GC006341.Received.
- Griffith, W.A., Sanz, P.F., and Pollard, D.D., 2009, Influence of Outcrop Scale Fractures on the Effective Stiffness of Fault Damage Zone Rocks: *Pure and Applied Geophysics*, v. 166, p. 1595–1627, doi:10.1007/s00024-009-0519-9.
- Gu, J.C., Rice, J.L., Ruina, A.L., and Tse, S.T., 1984, Slip Motion and Stability of a Single Degree of Freedom Elastic System With Rate and State Dependent: *J. Me&. Phys. Solids*, v. 32, p. 167–196.
- Gu, Y., and Wong, T.-F., 1991, Effects of loading velocity, stiffness, and inertia on the dynamics of a single degree of freedom spring-slider system: *Journal of Geophysical Research*, v. 96, doi:10.1029/91jb02271.
- Handwerger, A.L., Rempel, A.W., Skarbek, R.M., Roering, J.J., and Hilley, G.E., 2016, Rate-weakening friction characterizes both slow sliding and catastrophic failure of landslides: *Proceedings of the National Academy of Sciences of the United States of America*, v. 113, p. 10281–10286, doi:10.1073/pnas.1607009113.
- Harbord, C.W.A., Nielsen, S.B., De Paola, N., and Holdsworth, R.E., 2017, Earthquake nucleation on rough faults: *Geology*, v. 45, p. 931–934, doi:10.1130/G39181.1.
- Harris, R.A., 2017, Large earthquakes and creeping faults: *Reviews of Geophysics*, v. 55, p. 169–198, doi:10.1002/2016RG000539.

- Heaton, T.H., 1990, Evidence for and implications of self-healing pulses of slip in earthquake rupture: *Physics of the Earth and Planetary Interiors*, v. 64, p. 1–20, doi:10.1016/0031-9201(90)90002-F.
- Hughes, A., Kendrick, J.E., Salas, G., Wallace, P.A., Legros, F., Di Toro, G., and Lavallée, Y., 2020, Shear localisation, strain partitioning and frictional melting in a debris avalanche generated by volcanic flank collapse: *Journal of Structural Geology*, v. 140, doi:10.1016/j.jsg.2020.104132.
- Hyun, S., Pei, L., Molinari, J.F., and Robbins, M.O., 2004, Finite-element analysis of contact between elastic self-affine surfaces: *Physical Review E - Statistical Physics, Plasmas, Fluids, and Related Interdisciplinary Topics*, v. 70, p. 12, doi:10.1103/PhysRevE.70.026117.
- Ida, Y., 1972, Cohesive force across the tip of a longitudinal-shear crack and Griffith's specific surface energy: *Journal of Geophysical Research*, v. 77, p. 3796–3805, doi:10.1029/jb077i020p03796.
- Ide, S., Beroza, G.C., Shelly, D.R., and Uchide, T., 2007, A scaling law for slow earthquakes: *Nature*, v. 447, p. 76–79, doi:10.1038/nature05780.
- Ikari, M.J., 2019, Laboratory slow slip events in natural geological materials: *Geophysical Journal International*, v. 218, p. 354–387, doi:10.1093/gji/ggz143.
- Ikari, M.J., Carpenter, B.M., and Marone, C., 2016, A microphysical interpretation of rate- and state-dependent friction for fault gouge: *Geochemistry, Geophysics, Geosystems*, v. 17, p. 1660–1677, doi:10.1002/2016GC006286.
- Ikari, M.J., and Hüpers, A., 2021, Velocity-weakening friction induced by laboratory-controlled lithification: *Earth and Planetary Science Letters*, v. 554, p. 116682, doi:10.1016/j.epsl.2020.116682.
- Ikari, M.J., and Kopf, A.J., 2017, Seismic potential of weak, near-surface faults revealed at plate tectonic slip rates: *Science Advances*, v. 3, p. 1–7, doi:10.1126/sciadv.1701269.
- Ikari, M.J., Marone, C., and Saffer, D.M., 2011, On the relation between fault strength and frictional stability: *Geology*, v. 39, p. 83–86, doi:10.1130/G31416.1.
- Ikari, M.J., Marone, C., Saffer, D.M., and Kopf, A.J., 2013, Slip weakening as a mechanism for slow earthquakes: *Nature Geoscience*, v. 6, p. 468–472, doi:10.1038/ngeo1818.
- Ikari, M.J., Saffer, D.M., and Marone, C., 2009, Frictional and hydrologic properties of clay-rich fault gouge: *Journal of Geophysical Research: Solid Earth*, v. 114, p. 1–18, doi:10.1029/2008JB006089.
- Ikari, M.J., Wallace, L.M., and Rabinowitz, H.S., 2020, Observations of Laboratory and Natural Slow Slip Events: Hikurangi Subduction Zone, New Zealand *Geochemistry, Geophysics, Geosystems*: *Geochemistry, Geophysics, Geosystems*, v. 21, p. 1–19, doi:10.1029/2019GC008717.
- Ito, Y. et al., 2013, Episodic slow slip events in the Japan subduction zone before the 2011 Tohoku-Oki earthquake: *Tectonophysics*, v. 600, p. 14–26, doi:10.1016/j.tecto.2012.08.022.
- Jeppson, T.N., and Tobin, H.J., 2015, San Andreas fault zone velocity structure at SAFOD at core, log, and seismic scales: *Journal of Geophysical Research: Solid Earth*, v. 120, p. 4983–4997, doi:10.1002/2015JB012608.Received.
- Johnson, T.L., and Scholz, C.H., 1976, Dynamic properties of stick-slip friction of rock: *Journal of Geophysical Research*, v. 81, p. 881–888, doi:10.1029/jb081i005p00881.
- Kamb, B., 1970, Sliding motion of glaciers: Theory and observation: *Reviews of Geophysics*, v. 8, p. 673–728, doi:10.1029/RG008i004p00673.
- Kanamori, H., and Allen, C.R., 1986, Earthquake repeat time and average stress drop, *in* *Earthquake source mechanics*, p. 227–235, doi:10.1029/GM037p0227.
- Kanamori, H., and Anderson, D.L., 1975, Theoretical basis of some empirical relations in seismology: *Bulletin of the seismological society of America*, v. 65, p. 1073–1095.
- Kanamori, H., and Brodsky, E.E., 2004, The physics of earthquakes: *Reports on Progress in Physics*, v. 67, p. 1429–1496, doi:10.1088/0034-4885/67/8/R03.

- Kim, Y., Peacock, D.C.P., and Sanderson, D.J., 2004, Fault damage zones: *Journal of Structural Geology*, v. 26, p. 503–517, doi:10.1016/j.jsg.2003.08.002.
- Kirkpatrick, J.D., Edwards, J.H., Verdecchia, A., Kluesner, J.W., Harrington, R.M., and Silver, E.A., 2020, Subduction megathrust heterogeneity characterized from 3D seismic data: *Nature Geoscience*, doi:10.1038/s41561-020-0562-9.
- Lacroix, P., Handwerker, A.L., and Bièvre, G., 2020, Life and death of slow-moving landslides: *Nature Reviews Earth & Environment*, v. 1, p. 404–419, doi:10.1038/s43017-020-0072-8.
- Lay, T., Kanamori, H., and Ruff, L., 1982, The asperity model and the nature of large subduction zone earthquakes.: *Earthquake Prediction Research*, v. 1, p. 3–71.
- Lee, J.J., and Bruhn, R.L., 1996, Structural anisotropy of normal fault surfaces: *Journal of Structural Geology*, v. 18, p. 1043–1058, doi:10.1016/0191-8141(96)00022-3.
- Leeman, J.R., Marone, C., and Saffer, D.M., 2018, Frictional Mechanics of Slow Earthquakes: *Journal of Geophysical Research: Solid Earth*, p. 1–19, doi:10.1029/2018JB015768.
- Leeman, J.R., Saffer, D.M., Scuderi, M.M., and Marone, C., 2016, Laboratory observations of slow earthquakes and the spectrum of tectonic fault slip modes: *Nature Communications*, v. 7, p. 1–6, doi:10.1038/ncomms11104.
- Legros, F., Cantagrel, J.M., and Devouard, B., 2000, Pseudotachylite (frictionite) at the base of the Arequipa volcanic landslide deposit (Peru): Implications for emplacement mechanisms: *Journal of Geology*, v. 108, p. 601–611, doi:10.1086/314421.
- Lewis, K.B., Collot, J.-Y., and Lallemand, S.E., 1998, The dammed Hikurangi Trough: A channel-fed trench blocked by subducting seamounts and their wake avalanches (New Zealand-France GeodyNZ Project): *Basin Research*, v. 10, p. 441, doi:10.1046/j.1365-2117.1998.00080.x.
- Linde, A.T., and Sacks, I.S., 2002, Slow earthquakes and great earthquakes along the Nankai trough: *Earth and Planetary Science Letters*, v. 203, p. 265–275, doi:10.1016/S0012-821X(02)00849-X.
- Lipovsky, B.P., and Dunham, E.M., 2017, Slow-slip events on the Whillans Ice Plain, Antarctica, described using rate-and-state friction as an ice stream sliding law: *Journal of Geophysical Research: Earth Surface*, v. 122, p. 973–1003, doi:10.1002/2016JF004183.
- Liu, Y., and Rice, J.R., 2007, Spontaneous and triggered aseismic deformation transients in a subduction fault model: v. 112, p. 1–23, doi:10.1029/2007JB004930.
- Logan, J.M., and Rauenzahn, K.A., 1987, Frictional dependence of gouge mixtures of quartz and montmorillonite on velocity, composition and fabric: *Tectonophysics*, v. 144, p. 87–108, doi:10.1016/0040-1951(87)90010-2.
- Marone, C., 1998, Laboratory-Derived Friction Laws and Their Application To Seismic Faulting: *Annual Review of Earth and Planetary Sciences*, v. 26, p. 643–696, doi:10.1146/annurev.earth.26.1.643.
- Marone, C., Raleigh, C.B., and Scholz, C.H., 1990, Frictional behavior and constitutive modeling of simulated fault gouge: *Journal of Geophysical Research*, v. 95, p. 7007–7025, doi:10.1029/JB095iB05p07007.
- Marone, C., and Saffer, D.M., 2015, The Mechanics of Frictional Healing and Slip Instability During the Seismic Cycle: *Elsevier B.V.*, v. 4, 111–138 p., doi:10.1016/B978-0-444-53802-4.00092-0.
- Marone, C., and Scholz, C.H., 1988, The depth of seismic faulting and the upper transition from stable to unstable slip regimes: *Geophysical Research Letters*, v. 15, p. 621–624.
- Marone, C., Vidale, J.E., and Ellsworth, W.L., 1995, Fault healing inferred from time dependent variations in source properties of repeating earthquakes: *Geophysical Research Letters*, v. 22, p. 3095–3098.
- McBeck, J., Mair, K., and Renard, F., 2021, Decrypting healed fault zones: How gouge production reduces the influence of fault roughness: *Geophysical Journal International*, doi:10.1201/9781315366784.

- Mitchell, T.M., Ben-Zion, Y., and Shimamoto, T., 2011, Pulverized fault rocks and damage asymmetry along the Arima-Takatsuki Tectonic Line, Japan: *Earth and Planetary Science Letters*, v. 308, p. 284–297, doi:10.1016/j.epsl.2011.04.023.
- Morrow, C.A., Moore, D.E., and Lockner, D.A., 2000, The effect of mineral bond strength and adsorbed water on fault gouge frictional strength: *Geophysical Research Letters*, v. 27, p. 815–818.
- Nagata, K., Nakatani, M., and Yoshida, S., 2012, A revised rate- and state-dependent friction law obtained by constraining constitutive and evolution laws separately with laboratory data: *Journal of Geophysical Research: Solid Earth*, v. 117, p. 1–17, doi:10.1029/2011JB008818.
- Nicol, A., and Beavan, J., 2003, Shortening of an overriding plate and its implications for slip on a subduction thrust, central Hikurangi Margin, New Zealand: *Tectonics*, v. 22, p. n/a-n/a, doi:10.1029/2003tc001521.
- Nicol, A., and Wallace, L.M., 2007, Temporal stability of deformation rates : Comparison of geological and geodetic observations , Hikurangi subduction margin , New Zealand: *Earth and Planetary Science Letters*, v. 258, p. 397–413, doi:10.1016/j.epsl.2007.03.039.
- Niemeijer, A.R., and Spiers, C.J., 2005, Influence of phyllosilicates on fault strength in the brittle-ductile transition: insights from rock analogue experiments: *Geological Society, London, Special Publications*, v. 245, p. 303–327, doi:10.1144/GSL.SP.2005.245.01.15.
- Obara, K., Hirose, H., Yamamizu, F., and Kasahara, K., 2004, Episodic slow slip events accompanied by non-volcanic tremors in southwest Japan subduction zone: *Geophysical Research Letters*, v. 31, p. 1–4, doi:10.1029/2004GL020848.
- Obara, K., and Kato, A., 2016, Connecting slow earthquakes to huge earthquakes: *Science*, v. 353, p. 253–258.
- Ohnaka, M., Kuwahara, Y., Yamamoto, K., and Hirasawa, T., 1986, Dynamic breakdown processes and the generating mechanism for high-frequency elastic radiation during stick-slip instabilities, *in* *Earthquake source mechanics*, v. 37, p. 13–24.
- Okamoto, K.K., Brodsky, E.E., Thom, C.A., Smeraglia, L., and Billi, A., 2019, The Minimum Scale of Grooving on a Recently Ruptured Limestone Fault: *Geophysical Research Letters*, v. 46, p. 11878–11885, doi:10.1029/2019GL084889.
- Okubo, P.G., and Dieterich, J.H., 1984, Effects of Physical Fault Properties on Frictional Instabilities Produced on Simulated Faults: *Journal of Geophysical Research*, v. 89, p. 5817–5827.
- Palmer, A.C., and Rice, J.R., 1973, The growth of slip surfaces in the progressive failure of over-consolidated clay: *Proceedings of the Royal Society of London. A. Mathematical and Physical Sciences*, v. 332, p. 527–548, doi:10.1098/rspa.1973.0040.
- Pei, L., Hyun, S., Molinari, J.F., and Robbins, M.O., 2005, Finite element modeling of elasto-plastic contact between rough surfaces: *Journal of the Mechanics and Physics of Solids*, v. 53, p. 2385–2409, doi:10.1016/j.jmps.2005.06.008.
- Perfettini, H., and Ampuero, J.P., 2008, Dynamics of a velocity strengthening fault region: Implications for slow earthquakes and postseismic slip: *Journal of Geophysical Research: Solid Earth*, v. 113, p. 1–22, doi:10.1029/2007JB005398.
- Perrin, G., Rice, J.R., and Zheng, G., 1995, Self-healing slip pulse on a frictional surface: *Journal of the Mechanics and Physics of Solids*, v. 43, p. 1461–1495, doi:10.1016/0022-5096(95)00036-I.
- Le Pichon, X., Kreemer, C., and Chamot-Rooke, N., 2005, Asymmetry in elastic properties and the evolution of large continental strike-slip faults: *Journal of Geophysical Research: Solid Earth*, v. 110, p. 1–11, doi:10.1029/2004JB003343.
- Plaza-Faverola, A., Klaeschen, D., Barnes, P., Pecher, I., Henrys, S., and Mountjoy, J., 2012, Evolution of fluid expulsion and concentrated hydrate zones across the southern Hikurangi subduction margin, New Zealand: An analysis from depth migrated seismic data: *Geochemistry, Geophysics*,

- Geosystems, v. 13, p. n/a-n/a, doi:10.1029/2012gc004228.
- Posamentier, H.W., and Kolla, V., 2003, Seismic geomorphology and stratigraphy of depositional elements in deep-water settings: *Journal of Sedimentary Research*, v. 73, p. 367–388, doi:10.1306/111302730367.
- Power, W.L., and Tullis, T.E., 1991, Euclidean and fractal models for the description of rock surface roughness: *Journal of Geophysical Research*, v. 96, p. 415–424, doi:10.1029/90JB02107.
- Power, W.L., Tullis, T.E., Brown, S.R., Boitnott, G.N., and Scholz, C.H., 1987, Roughness of natural fault surfaces: *Geophysical Research Letters*, v. 14, p. 29–32.
- Rabinowitz, H.S., Savage, H.M., Skarbek, R.M., Ikari, M.J., Carpenter, B.M., and Collettini, C., 2018, Frictional Behavior of Input Sediments to the Hikurangi Trench, New Zealand: *Geochemistry, Geophysics, Geosystems*, p. 2973–2990, doi:10.1029/2018GC007633.
- Renard, F., Candela, T., and Bouchaud, E., 2013, Constant dimensionality of fault roughness from the scale of micro-fractures to the scale of continents: *Geophysical Research Letters*, v. 40, p. 83–87, doi:10.1029/2012GL054143.
- Renard, F., Voisin, C., Marsan, D., and Schmittbuhl, J., 2006, High resolution 3D laser scanner measurements of a strike-slip fault quantify its morphological anisotropy at all scales: *Geophysical Research Letters*, v. 33, p. 33–36, doi:10.1029/2005GL025038.
- Reyners, M., 1998, Plate coupling and the hazard of large subduction thrust earthquakes at the Hikurangi subduction zone, New Zealand: *New Zealand Journal of Geology and Geophysics*, v. 41, p. 343–354, doi:10.1080/00288306.1998.9514815.
- Rice, J.R., Lapusta, N., and Ranjith, K., 2001, Rate and state dependent friction and the stability of sliding between elastically deformable solids: *Journal of the Mechanics and Physics of Solids*, v. 49, p. 1865–1898, doi:10.1016/S0022-5096(01)00042-4.
- Rice, J.R., and Ruina, A.L., 1983, Stability of steady frictional slipping.: v. 5.
- Romanet, P., Bhat, H.S., Jolivet, R., and Madariaga, R., 2018, Fast and Slow Slip Events Emerge Due to Fault Geometrical Complexity: *Geophysical Research Letters*, p. 4809–4819, doi:10.1029/2018GL077579.
- Rowe, C.D., and Griffith, W.A., 2015, Do faults preserve a record of seismic slip: A second opinion: *Journal of Structural Geology*, v. 78, p. 1–26, doi:10.1016/j.jsg.2015.06.006.
- Roy, M., and Marone, C., 1996, Earthquake nucleation on model faults with rate- and state-dependent friction: Effects of inertia: *Journal of Geophysical Research*, v. 101, p. 919–932.
- Rubin, A.M., 2008, Episodic slow slip events and rate-and-state friction: *Journal of Geophysical Research: Solid Earth*, v. 113, p. 1–18, doi:10.1029/2008JB005642.
- Rubin, A.M., and Ampuero, J.P., 2005, Earthquake nucleation on (aging) rate and state faults: *Journal of Geophysical Research: Solid Earth*, v. 110, p. 1–24, doi:10.1029/2005JB003686.
- Ruggieri, R., Scuderi, M.M., Trippetta, F., Tinti, E., Brignoli, M., Mantica, S., Petroselli, S., Osculati, L., Volontè, G., and Collettini, C., 2021, The role of shale content and pore-water saturation on frictional properties of simulated carbonate faults: *Tectonophysics*, v. 807, p. 1–12, doi:10.1016/j.tecto.2021.228811.
- Ruina, A., 1983, Slip Instability and State Variable Laws: *Journal of geophysical research*, v. 88, p. 359–370.
- Saffer, D.M., and Marone, C., 2003, Comparison of smectite- and illite-rich gouge frictional properties: Application to the updip limit of the seismogenic zone along subduction megathrusts: *Earth and Planetary Science Letters*, v. 215, p. 219–235, doi:10.1016/S0012-821X(03)00424-2.
- Saffer, D.M., and Wallace, L.M., 2015, The frictional, hydrologic, metamorphic and thermal habitat of

- shallow slow earthquakes: *Nature Geoscience*, v. 8, p. 594–600, doi:10.1038/ngeo2490.
- Sagy, A., Brodsky, E.E., and Axen, G.J., 2007, Evolution of fault-surface roughness with slip: *Geology*, v. 35, p. 283–286, doi:10.1130/G23235A.1.
- Sagy, A., Tesei, T., and Collettini, C., 2017, Fault-surface geometry controlled by faulting mechanisms: Experimental observations in limestone faults: *Geology*, v. 45, p. 851–854, doi:10.1130/G39076.1.
- Samuelson, J., Elsworth, D., and Marone, C., 2009, Shear-induced dilatancy of fluid-saturated faults: Experiment and theory: *Journal of Geophysical Research: Solid Earth*, v. 114, p. 1–15, doi:10.1029/2008JB006273.
- Schmittbuhl, J., Gentier, S., and Roux, S., 1993, Field measurements of the roughness of fault surfaces: *Geophysical Research Letters*, v. 20, p. 639–641, doi:10.1029/93GL00170.
- Schmittbuhl, J., Schmitt, F., and Scholz, C., 1995, Scaling invariance of crack surfaces: *Journal of Geophysical Research*, v. 100, p. 5953–5973, doi:10.1029/94JB02885.
- Scholz, C.H., 1998, Earthquakes and friction laws: *Nature*, v. 391, p. 37–42, doi:10.1038/34097.
- Scholz, C.H., 2019, *The Mechanics of Earthquakes and Faulting*: Cambridge University Press, 493 p.
- Schwartz, S.Y., and Rokosky, J.M., 2007, Slow slip events and seismic tremor at circum-pacific subduction zones: reviews of geophysics, v. 45, doi:10.1029/2006RG000208.1.
- Scuderi, M.M., Carpenter, B.M., Johnson, P.A., and Marone, C., 2016a, Poromechanics of stick-slip frictional sliding and strength recovery on tectonic faults: *Journal of Geophysical Research: Solid Earth*, p. 3782–3803, doi:10.1002/2015JB012608.Received.
- Scuderi, M.M., Collettini, C., Viti, C., Tinti, E., and Marone, C., 2017, Evolution of shear fabric in granular fault gouge from stable sliding to stick slip and implications for fault slip mode: *Geology*, v. 45, p. 731–734, doi:10.1130/G39033.1.
- Scuderi, M.M., Marone, C., Tinti, E., Di Stefano, G., and Collettini, C., 2016b, Precursory changes in seismic velocity for the spectrum of earthquake failure modes: *Nature Geoscience*, v. 9, p. 695–700, doi:10.1038/ngeo2775.
- Share, P., and Ben-zion, Y., 2016, Bimaterial interfaces in the south San Andreas Fault with opposite velocity contrasts NW and SE from San Gorgonio Pass: , p. 680–687, doi:10.1002/2016GL070774.Received.
- Shervais, K.A.H., and Kirkpatrick, J.D., 2016, Smoothing and re-roughening processes: The geometric evolution of a single fault zone: *Journal of Structural Geology*, v. 91, p. 130–143, doi:10.1016/j.jsg.2016.09.004.
- Shi, Z., and Ben-Zion, Y., 2006, Dynamic rupture on a bimaterial interface governed by slip-weakening friction: *Geophysical Journal International*, v. 165, p. 469–484, doi:10.1111/j.1365-246X.2006.02853.x.
- Shibazaki, B., Wallace, L.M., Kaneko, Y., Hamling, I., Ito, Y., and Matsuzawa, T., 2019, Three-Dimensional Modeling of Spontaneous and Triggered Slow-Slip Events at the Hikurangi Subduction Zone, New Zealand: *Journal of Geophysical Research: Solid Earth*, v. 124, p. 13250–13268, doi:10.1029/2019JB018190.
- Shlomai, H., and Fineberg, J., 2016, The structure of slip-pulses and supershear ruptures driving slip in bimaterial friction: *Nature Communications*, v. 7, p. 1–7, doi:10.1038/ncomms11787.
- Shuzui, H., 2001, Process of slip-surface development and formation of slip-surface clay in landslides in Tertiary volcanic rocks, Japan: *Engineering Geology*, v. 61, p. 199–220, doi:10.1016/S0013-7952(01)00025-4.
- Singh, R., and Pathak, S., 2013, In-Situ Normal Stiffness of Rock Mass: *INDOROCK 2013: Fourth Indian Rock Conference*,.

- Skarbek, R.M., Rempel, A.W., and Schmidt, D.A., 2012, Geologic heterogeneity can produce aseismic slip transients: *Geophysical Research Letters*, v. 39, p. 1–5, doi:10.1029/2012GL053762.
- Skarbek, R.M., and Savage, H.M., 2019, RSFit3000: A MATLAB GUI-based program for determining rate and state frictional parameters from experimental data: *Geosphere*, v. 15, p. 1665–1676, doi:10.1130/GES02122.1.
- Sun, T., Saffer, D., and Ellis, S., 2020, Mechanical and hydrological effects of seamount subduction on megathrust stress and slip: *Nature Geoscience*, v. 13, p. 249–255, doi:10.1038/s41561-020-0542-0.
- Tesei, T., Carpenter, B.M., Giorgetti, C., Scuderi, M.M., Sagy, A., Scarlato, P., and Collettini, C., 2017, Friction and scale-dependent deformation processes of large experimental carbonate faults: *Journal of Structural Geology*, v. 100, p. 12–23, doi:10.1016/j.jsg.2017.05.008.
- Toy, V.G., Niemeijer, A.R., Renard, F., Morales, L., and Wirth, R., 2017, Striation and slickenline development on quartz fault surfaces at crustal conditions: origin and effect on friction: *Journal of Geophysical Research : Solid Earth*, v. 122, p. 3497–3512, doi:10.1002/2016JB013498.
- Verberne, B.A., Niemeijer, A.R., De Bresser, J.H.P., and Spiers, C.J., 2015, Mechanical behavior and microstructure of simulated calcite fault gouge sheared at 20–600°C: Implications for natural faults in limestone: *Journal of Geophysical Research : Solid Earth*, v. 120, p. 8169–8196, doi:10.1002/2015JB012352.Received.
- Vidale, J.E., Ellsworth, W.L., Cole, A., and Marone, C., 1994, Variations in rupture process with recurrence interval in a repeated small earthquake: *Nature*, v. 368, p. 624–626.
- Vincent-Dospital, T., Steyer, A., Renard, F., and Toussaint, R., 2021, Frictional anisotropy of 3D-printed fault surfaces: *Frontiers in Earth Science*, p. 1–10.
- Voisin, C., Renard, F., and Grasso, J.R., 2007, Long term friction: From stick-slip to stable sliding: *Geophysical Research Letters*, v. 34, p. 0–4, doi:10.1029/2007GL029715.
- Wallace, L.M. et al., 2009, Characterizing the seismogenic zone of a major plate boundary subduction thrust: Hikurangi Margin, New Zealand: *Geochemistry, Geophysics, Geosystems*, v. 10, doi:10.1029/2009GC002610.
- Wallace, L.M., 2020, Slow Slip Events in New Zealand: *Annual Review of Earth and Planetary Sciences*, v. 48, p. 175–203, doi:10.1146/annurev-earth-071719-055104.
- Wallace, Barnes, P., Beavan, J., Van Dissen, R., Litchfield, N., Mountjoy, J., Langridge, R., Lamarche, G., and Pondard, N., 2012a, The kinematics of a transition from subduction to strike-slip: An example from the central New Zealand plate boundary: *Journal of Geophysical Research*, v. 117, doi:10.1029/2011JB008640.
- Wallace, L.M., and Beavan, J., 2010, Diverse slow slip behavior at the Hikurangi subduction margin, New Zealand: *Journal of Geophysical Research*, v. 115, p. 1–20, doi:10.1029/2010JB007717.
- Wallace, L.M., Beavan, J., Bannister, S., and Williams, C., 2012b, Simultaneous long-term and short-term slow slip events at the Hikurangi subduction margin, New Zealand: Implications for processes that control slow slip event occurrence, duration, and migration: *Journal of Geophysical Research*, v. 117, p. 1–18, doi:10.1029/2012JB009489.
- Wallace, L.M., Beavan, J., McCaffrey, R., and Darby, D., 2004, Subduction zone coupling and tectonic block rotations in the North Island, New Zealand: *Journal of Geophysical Research: Solid Earth*, v. 109, p. 1–21, doi:10.1029/2004JB003241.
- Wallace, L.M., and Eberhart-Phillips, D., 2013, Newly observed, deep slow slip events at the central Hikurangi margin, New Zealand: Implications for downdip variability of slow slip and tremor, and relationship to seismic structure: *Geophysical Research Letters*, v. 40, p. 5393–5398, doi:10.1002/2013GL057682.
- Wallace, L.M., Saffer, D.M., Barnes, P.M., Pecher, I.A., Petronotis, K.E., LeVay, L.J., and Scientists, E. 372/375, 2019, Hikurangi Subduction Margin Coring, Logging and Observatories: *Proceedings of*

- the International Ocean Discovery Program, v. 372B/375, doi:<https://doi.org/10.14379/iodp.proc.372B375.2019>.
- Wallace, L.M., Webb, S.C., Ito, Y., Mochizuki, K., Hino, R., Henrys, S., Schwartz, S.Y., and Sheehan, A.F., 2016, Slow slip near the trench at the Hikurangi subduction zone, New Zealand: *Science*, v. 352, p. 701–704, doi:10.1126/science.aaf2349.
- Wang, K., and Bilek, S.L., 2014, Invited review paper: Fault creep caused by subduction of rough seafloor relief: *Tectonophysics*, v. 610, p. 1–24, doi:10.1016/j.tecto.2013.11.024.
- Wang, W., and Scholz, C.H., 1994, Micromechanics of the velocity and normal stress dependence of rock friction: *Pure and Applied Geophysics PAGEOPH*, v. 143, p. 303–315, doi:10.1007/BF00874333.
- Weertman, J., 1980, Unstable slippage across a fault that separates elastic media of different elastic constants: *Journal of Geophysical Research*, v. 85, p. 1455–1461, <http://dx.doi.org/10.1029/JB085iB03p01455>; doi:10.1029/JB085iB03p01455.
- Wood, R., and Davy, B., 1994, The Hikurangi Plateau: *Marine Geology*, v. 118, p. 153–173, doi:10.1016/0025-3227(94)90118-X.
- Zhao, P., Peng, Z., Shi, Z., Lewis, M.A., and Ben-zion, Y., 2010, Variations of the velocity contrast and rupture properties of M6 earthquakes along the Parkfield section of the San Andreas fault: *Geophysical Journal International*, v. 180, p. 765–780, doi:10.1111/j.1365-246X.2009.04436.x.
- Zielke, O., Galis, M., and Mai, P.M., 2017, Fault roughness and strength heterogeneity control earthquake size and stress drop: *Geophysical Research Letters*, v. 44, p. 777–783, doi:10.1002/2016GL071700.
- Zoet, L.K., Carpenter, B., Scuderi, M., Alley, R.B., Anandakrishnan, S., Marone, C., and Jackson, M., 2013, The effects of entrained debris on the basal sliding stability of a glacier: *Journal of Geophysical Research: Earth Surface*, v. 118, p. 656–666, doi:10.1002/jgrf.20052.
- Zoet, L.K., Ikari, M.J., Alley, R.B., Marone, C., Anandakrishnan, S., Carpenter, B.M., and Scuderi, M.M., 2020, Application of Constitutive Friction Laws to Glacier Seismicity: *Geophysical Research Letters*, v. 47, p. 1–9, doi:10.1029/2020GL088964.
- Zoet, L.K., and Iverson, N.R., 2020, A slip law for glaciers on deformable beds: *Science*, v. 368, p. 76–78, doi:10.1126/science.aaz1183.

## 7 Acknowledgements

I owe a big thanks to my supervisor Matt Ikari. Thank you for your support and never-ending criticism, for always providing almost-instantaneous feedback on my work and for asking me (often annoying) questions to nudge my thinking into the right direction. Looking back, I really appreciate how you challenged me and tried to make me a better all-round scientist.

I would like to thank Alex Rösner and especially Katja Stanislowski for being on this PhD journey with me, for the many discussions we had, and for helping each other out in the laboratory. I also have to thank Katja for helping me find the German way of life and for the fun times and (virtual) coffee breaks. I would also like to thank Philipp Haberkorn, both for being my office mate since the start and for your work as our lab technician, some of your improvements on the Giesa devices made our lives a lot easier. I am especially grateful for your work in designing and constructing the CLSM sample holder and the stiffness extensions needed for the stiffness study. Without those, a lot of the work presented here would not have existed. I would also like to thank Professor Achim Kopf and the other members of the AG Kopf and AG Mörz. A big thanks goes out to Nele and Ricarda who supported me and kept me motivated and sane during the challenging last phases of my PhD.

I have to thank the graduate school GLOMAR for the many interesting courses organized, for providing funding to travel to various conferences and for funding that enabled my research stay in Oslo. Also the funding for Plan M – mentoring in Science provided by GLOMAR was greatly appreciated. I have to mention how much I enjoyed the Writing Space organized by GLOMAR, without which a lot of the thesis writing would have been more problematic.

## 8 Versicherung an Eides Statt / Affirmation in lieu of an oath

### **Versicherung an Eides Statt / Affirmation in lieu of an oath**

**gem. § 5 Abs. 5 der Promotionsordnung vom 18.06.2018 /**

**according to § 5 (5) of the Doctoral Degree Rules and Regulations of 18 June, 2018**

Ich / I, Agathe Eijsink, Bremen

(Vorname / First Name, Name / Name, Anschrift / Address, ggf. Matr.-Nr. / student ID no., if applicable)

versichere an Eides Statt durch meine Unterschrift, dass ich die vorliegende Dissertation selbständig und ohne fremde Hilfe angefertigt und alle Stellen, die ich wörtlich dem Sinne nach aus Veröffentlichungen entnommen habe, als solche kenntlich gemacht habe, mich auch keiner anderen als der angegebenen Literatur oder sonstiger Hilfsmittel bedient habe und die zu Prüfungszwecken beigelegte elektronische Version (PDF) der Dissertation mit der abgegebenen gedruckten Version identisch ist. / *With my signature I affirm in lieu of an oath that I prepared the submitted dissertation independently and without illicit assistance from third parties, that I appropriately referenced any text or content from other sources, that I used only literature and resources listed in the dissertation, and that the electronic (PDF) and printed versions of the dissertation are identical.*

Ich versichere an Eides Statt, dass ich die vorgenannten Angaben nach bestem Wissen und Gewissen gemacht habe und dass die Angaben der Wahrheit entsprechen und ich nichts verschwiegen habe. / *I affirm in lieu of an oath that the information provided herein to the best of my knowledge is true and complete.*

Die Strafbarkeit einer falschen eidesstattlichen Versicherung ist mir bekannt, namentlich die Strafandrohung gemäß § 156 StGB bis zu drei Jahren Freiheitsstrafe oder Geldstrafe bei vorsätzlicher Begehung der Tat bzw. gemäß § 161 Abs. 1 StGB bis zu einem Jahr Freiheitsstrafe oder Geldstrafe bei fahrlässiger Begehung. / *I am aware that a false affidavit is a criminal offence which is punishable by law in accordance with § 156 of the German Criminal Code (StGB) with up to three years imprisonment or a fine in case of intention, or in accordance with § 161 (1) of the German Criminal Code with up to one year imprisonment or a fine in case of negligence.*

---

Ort / Place, Datum / Date

---

Unterschrift / Signature